

# Design and development of MEMs rotary fans

Keramati, Hamed

2010

Keramati, H. (2010). Design and development of MEMs rotary fans. Master's thesis,  
Nanyang Technological University, Singapore.

<https://hdl.handle.net/10356/41856>

<https://doi.org/10.32657/10356/41856>

# **DESIGN AND DEVELOPMENT OF MEMS ROTARY FANS**

**HAMED KERAMATI**

School of Mechanical and Aerospace Engineering

A thesis submitted to the Nanyang Technological University  
in fulfillment of the requirement for the degree of  
Master of Engineering

**2010**

## **Acknowledgment**

I would like to express my appreciation to my supervisor Prof. Chan Weng Kong and my co-supervisor Prof. Miao Jianmin for their supports, encouragements, and helping me throughout my research project. I am also grateful to Nanyang Technological University for the use of facilities and A-Star for financial support. Furthermore, I would like to thank my dear parents and brothers for their constant support and their incredible patience during my study. I thank Nay Lin, Tan Chee Wee, Lim Wei Meng and Mr. Pek, Mr. Ho for helping me through the fabrication process. I would also like to appreciate Mr. Eric's efforts for conducting the experiments. And finally, I would like to thank my dear friends for their supports and helps.

## Table of Contents

Abstract .....	4
1 Introduction.....	6
2 Literature review .....	9
2.1 Introduction .....	9
2.2 Air cooling technologies .....	11
2.2.1 Geometric Scaling of Fans.....	14
2.3 Aerodynamics.....	18
2.3.1 Introduction.....	18
2.3.2 Airfoil.....	19
2.3.3 Conventional fan design .....	22
2.3.4 Drag Force .....	28
2.3.5 Cordier diagram .....	29
2.3.6 Physical Properties at Micro-Scale .....	31
2.4 Fan Testing.....	31
2.5 Fabrication.....	33
2.5.1 3-D Micro-fabrication .....	34
2.5.2 Other fabrication methods.....	37
2.5.3 SU-8.....	38
2.5.4 UV Lithography on SU-8.....	42
3 Design and Fabrication .....	46

3.1	Introduction .....	46
3.2	Design Procedure .....	47
3.3	Fabrication.....	55
3.3.1	Introduction.....	56
3.3.2	Fabrication Procedure .....	58
3.3.3	Masks .....	66
3.3.4	Results and Discussion .....	68
3.3.5	Discussion .....	72
4	Numerical Modelling .....	76
4.1	Introduction .....	76
4.2	Fan Geometry .....	77
4.2.1	Boundary conditions .....	78
4.2.2	Mesh Generation .....	79
4.2.3	Numerical Simulation .....	82
5	Design Modification .....	84
5.1	Results for Angle of attack= $15^{\circ}$ .....	84
5.2	Aerodynamic Coefficients.....	89
5.3	Discussions.....	94
5.4	Modification of the Geometry .....	95
5.4.1	Results for Angle of attack= $15^{\circ}$ .....	96
5.5	Flat-Plate Cross-Section.....	100

5.5.1	Geometry.....	100
5.5.2	Numerical Simulation .....	101
5.6	Discussions.....	103
6	Fan Testing and Experiment .....	106
6.1	Introduction .....	106
6.2	Calibration.....	107
6.3	Test Rig .....	109
6.4	Torque Calculation .....	110
6.5	Results and Discussion.....	111
7	Conclusions and Recommendations .....	115
7.1	Conclusions .....	115
7.2	Recommendations .....	118
8	References.....	121
	Appendix A.....	127
	Appendix B .....	128
	Preliminary Design .....	129
	Modified Geometry.....	147
	Flat Plate .....	155

## Abstract

As miniaturization technologies improve, electronic devices are becoming smaller and, hence, smaller devices are needed for heat removal. Micro fans are very crucial in compact cooling technologies. Among them, axial fans have unique properties that make them very useful in different applications. Previous studies concentrate mainly on centrifugal micro turbomachines because micro fabrication limitations do not allow making efficient 3-D axial fans. In the present project, a mini-axial fan was designed and fabricated. A conventional fan design method was adopted to obtain the preliminary design. 2-D numerical modelling was carried out to modify the design. During the design procedure, fabrication limitations were considered. Hence, the modelled geometries were influenced by UV photolithography which is selected as the fabrication method in this project. Being a planar technique, only layer-by-layer 3-D devices can be produced using UV lithography. SU-8, because of its special properties, was selected as the photoresist. A comparison was made between modified and non-modified geometries. It was concluded that the obtained results did not violate the assumptions made. Nonetheless, some modifications are necessary to improve the fan efficiency. Some prototypes were fabricated and we succeeded in fabricating some fans with oblique walls using UV lithography. The relationship between the product quality and some of the parameters were determined. The fabricated fans were tested. The pressure generated by the fans was measured. The results show that the 2-D numerical analysis can predict the best angle of attack approximately according to lift/drag ratio criteria. The fabricated fans were tested and the results were compared to 2-D numerical analyses at the same angle of

attack. It is concluded that the 2-D simulations and the lift/drag ratio criteria can give us an acceptable estimation of the best angle of attack. In general, the best angle of attack based on static pressure generation is  $20^\circ$ . The flow rates generated by the fans with the angle of attacks of  $15^\circ$  and  $20^\circ$  are almost the same.



# 1 Introduction

Fans have a large number of applications such as cooling, ventilation and air moving applications. They are the most important fields that fans are applicable in.

As miniaturization advances rapidly, small fans are needed in many different industries. Air flow controlling devices in micro scale experimental set-ups is a field that small fans are essential. In electronic devices, one of the limitations that slow down possible developments in the production of smaller electronic devices is the problem caused by the rate of heat removal. Small fans could solve some of such problems and reduce the effect of limitations related to heat dissipation.

In this project, the objective is to design, analyze, simulate and fabricate a very small axial fan that can be used in the above-mentioned applications. However, the main aim is using it in cooling technology.

At the beginning of the project, a thorough literature review was conducted. In spite of its importance, limitations in fabrication processes in the mini and micro scale have impeded the progress in this area. Fortunately, in recent years, fabrication technologies are getting more developed and advanced as miniaturization is needed in numerous industries such as

electronic and computer devices, medical devices and experimental set-ups for micro fluidic researches.

Axial fans have some special advantages that make them necessary to be used in many applications. Conventional axial fans are used in many applications that centrifugal and diaphragm fans cannot be used. Some examples are open- and closed-circuits wind tunnels, condensers and ventilation. These applications not only can be used in micro scale, but also seems to be necessary for evaluating the calculation and numerical predictions in empirical investigations.

This project contains three key elements: design, simulation and fabrication.

In the design stage, a conventional method was used to determine the preliminary design. Although the method is used for conventional axial fans, it can serve as a guideline to size the preliminary geometry. The air flow rate and pressure drop are input required to determine the fan specifications. The preliminary fan geometry is determined using the Cordier diagram.

Generally, because of practical considerations, designers do not have many choices for their designs at micro-scale. In other words, micro-fabrication methods impose many limitations which result in few designs for any device. This is especially true for 3-Dimensional shapes which are difficult to fabricate. Hence, the designs developed would have to be modified for ease of fabrication. A geometrically-simple layer-by-layer blade was designed and it was very different from those that are used conventionally.

Subsequently, a numerical modelling of the blade was conducted to study the effect caused by the deviation from the preliminary design because of fabrication constraints.

Fluid flow in complex geometry can be solved numerically. CFD (Computational Fluid Dynamics) simulations help us to understand the flow better. For this reason, simulations

were carried out to determine the best angle of attack in the layer-by-layer blades. The FLUENT software was used as a solver and the GAMBIT as the geometry and mesh generator. Based on these results, the blade profile is modified so that the optimal characteristics can be obtained.

The fabrication process is the last stage of this project. SU-8 lithography was chosen as the fabrication method as it is relatively cheap. With SU-8, it is possible to achieve very high aspect ratio in comparison with other micro-fabrication methods. In addition, relatively high thicknesses can also be achieved. Different samples were fabricated. The fabrication parameters were changed to obtain higher quality. SEM images are taken to compare the quality of the different samples. Success in making oblique part of the fan blade was the most important part of the fabrication stage. Fabrication of multi-layer SU-8 products having oblique parts using UV lithography is a new achievement.

The fans were tested in a designed test rig. The pressure generated and flow rate were then measured. The results are presented and discussed in the chapter 6.

## 2 Literature review

### 2.1 Introduction

Micro fans are useful for many applications where producing and controlling gas flow at the micro-scale is needed. The interest of miniaturized turbo machines is fuelled by both technology push and user pull. The technology push is the capability of fabricating very small structures and the availability of high manufacturing speed. The user pull is the need of compact energy supplier and, consequently, compact heat removers in small, portable electronics and computers, GPS receivers, cell phones, etc. Moreover, as research continues in the field of micro-fluidics, the need for such devices will become more important.

Small fans, either micro-scale or mini-scale, can be used in many fields. In general, their applications can be considered in aerosol collections in micro channels, micro air vehicles (MAV) and chip-scale cooling systems for electronic devices. Additionally, they can also be used in micro combustion motors as a necessary part of chemical mixing systems at micro-scale to solve the problems of mixing in low Reynolds number regimes. Some applications are illustrated in Figure 2-1.

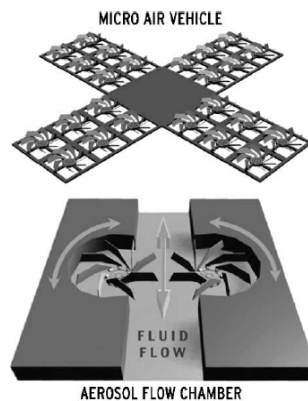


Figure 2-1 Depiction of micro fan application concepts [1]

Due to this increasing need for small fans, design and development of micro-fans are becoming critical. In addition, more economic fabrication, testing and mass-production techniques are also needed.

For different applications, micro fans have different characteristics. However, being compact and light are two key characteristics for all cases. Moreover, as an air mover, the ability of generating enough pressure and flow rate is a critical factor.

In spite of the great variety of fans, rotary fans have some unique characteristics (e.g. produce constant flows). This can be an important advantage as compared to diaphragm pumping system which produces peristaltic flows.

Numerous projects and researches have been carried out in the field of small turbomachines. Almost all the researches in this area are focused on centrifugal turbomachines because it is very difficult to make axial 3-D structures using micro fabrication techniques like planar lithography [2]. Many approaches have been tested and analyzed. Scaled down version of conventional types, which are fabricated using conventional method like CNC machining are tested [3, 4]. As an alternative for conventional fabrication methods, in some other

researches, micro fabrication methods were used to manufacture mini- and micro-scale turbomachine [5].

Micro fabrication methods have some limitations including fabrication time, shape of products, etc. Despite these limitations, Micro-Electrical-Mechanical-Systems (MEMS) fabrication methods have many advantages in contrast to conventional fabrication methods, e.g. better accuracy at the micro-scale.

Some micro turbomachines are also designed to operate efficiently at low Reynolds numbers [2, 5]. The design methods are different when the size changes from macro to mini or micro. These differences are due to the differences in operating conditions and different physical properties, e.g. difference in material properties which is one of the critical parameters in the design [2].

This chapter consists three main sections. In the first section, an introduction to air cooling technologies is presented. The second section presents the aerodynamics of fans and conventional fan design technique which will be used in this project. A literature review on micro manufacturing will be presented in the last section.

## **2.2 Air cooling technologies**

Cooling elements is one of the essential parts of electronic devices. If advanced cooling technologies were not developed, it would not be possible to have advanced, portable and small electronic devices. Using rotary fans is the easiest way to produce forced flow to cool these devices. However, other than using fans, there are other technologies that can be used to remove heat.

Piezoelectricity is one of the technologies used to accelerate air. Piezoelectricity is the ability of generation of electricity by mechanical strain and vice versa in special crystals. Yoo et. al [6] worked on simple-designed piezoelectric cooling fans and developed correlations between the tip displacement and the wind velocity under operating conditions. This type of fans has the advantage of the elimination of unwanted electromagnetic noises produced by rotary type fans [6]. The wind velocity produced using this technique is, in general, adequate for small fans. However, the displacements and dimensions of the oscillating plates are relatively large to be used in very small devices such as mobile phones and GPS facilities.

Another technology for mobile electronic devices cooling is using phase-change materials (PCM). As its name implies, this technology utilized the latent heat for cooling. The use of PCM in chips inside a personal digital assistant and the orientation of the heat storage unit are experimentally investigated [7]. Since the phase change occurs at uniform temperature, the temperature of the electronic device can be maintained. Heat could be dissipated to the surroundings from the PCM. Therefore, to obtain more effective devices, forced convection heat transfer is needed which can be produced by a fan.

Electrostatic propulsion can also be a useful technology to accelerate air [8, 9]. This technology is based on the corona discharge as the driving mechanism for a high air velocity. The principle of this technique is illustrated in Figure 2-2 [9].

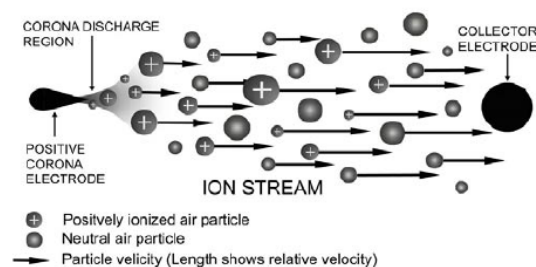


Figure 2-2 Ion stream of a DC electrostatic air pump where the corona and collector electrodes are powered by a high voltage DC source[9].

The main advantages of this technology over conventional fans are the elimination of moving parts, low noise, dynamic airflow profiles, versatile shapes and sizes, and compatibility with chip and chip-level structures.

However, this technology is not mature and extensive studies are still being conducted. Modifying and optimizing electrostatic air pumps for use at the micro-scale is another scope for researchers working in this field [9]. Several attempts were conducted to improve this technique: miniaturizing electrostatic air accelerator [10], numerical simulation of the electrical field [11], coupled-physics modelling [8] and heat transfer enhancement [12].

As each technology has its own benefits and disadvantages, the most efficient cooling system will most likely be a combination of a number of current technologies. Axial fans can be used as a complementary part in the above-mentioned technologies as they have the potential to remove heat from critical components and exhaust it to the ambient in a relatively simple and effective way.

Scaling is a common approach for developing small fans [3]. However, the problem of dynamic similarity arises; the reduction of fan dimensions to the micro-scale causes increased performance loss. Hence, geometric scaling of macro-scale designs is not sufficient to produce efficient micro-scale cooling fans [3]. Some modifications, according to the changes in flow physics, must be made. The following section will be devoted to the geometric scaling of fans as it is the key to the performance prediction of micro-scale fans.



### 2.2.1 Geometric Scaling of Fans

The performance of all geometrically similar conventional fans, which are operating at the same specific speed, is the same. However, as the Reynolds number is reduced and the boundary layers become laminar, the efficiency of the fan becomes particularly sensitive to the Reynolds number [3]. The non-dimensional fan performance is illustrated in Figure 2-3.

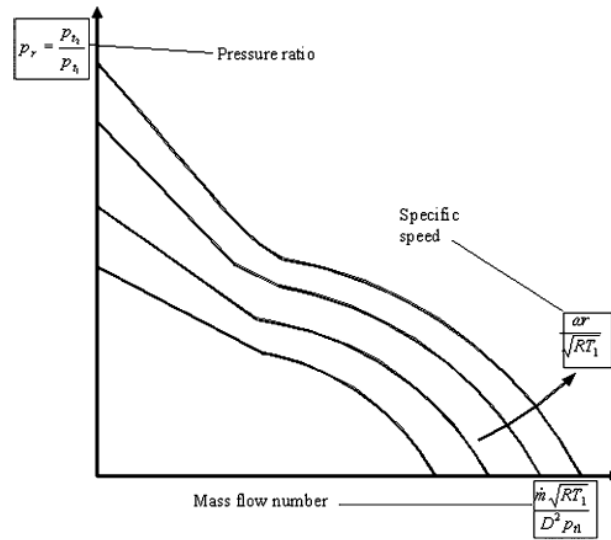


Figure 2-3 Non-dimensional fan performance[3]

According to some analytical investigations, a reduction in efficiency and a drop in performance as the fan size reduces is reported [3]. To relate the size to the efficiency, the entropy generation rate can be used, to predict the efficiency. Equation (2.1) relates the non-dimensional entropy generation rate and the Reynolds number in laminar boundary layer [13].

$$\frac{TS''}{\rho U_e^3} = 0.17 \text{Re}_\theta^{-1} \quad (2.1)$$

where,  $T$  is the temperature,  $S''$  is the entropy generation rate per unit area,  $U_e$  is velocity at the boundary-layer edge,  $\rho$  is the density and  $Re_\theta$  is the Reynolds number with respect to the momentum thickness  $\theta$ . The left-hand-side of equation (2.1) is named the dissipation coefficient  $C_d$ .

The dissipation coefficient for turbulent boundary layer is different and is shown in equation (2.2)

$$C_d = 0.0056 Re_\theta^{-1/6} \quad (2.2)$$

where  $10^3 < Re_\theta < 10^5$  [14].

The most striking feature is that for laminar boundary layers the dissipation coefficient is dependent on the state of boundary layer, i.e., on the shape factor[14]. As size reduces, laminar flow will dominate. This causes a large increase in the local entropy generation rate in the boundary layer, which, obviously, affects the efficiency in a negative manner.

The dissipation coefficient for laminar flow can be written as

$$C_d = 0.17 Re_\theta^{-1} \quad (2.3)$$

This coefficient for laminar flow is larger than the corresponding coefficient for turbulent flow. If the scale is reduced excessively, then the entropy produced exceeds the pressure rise generated and the work done by the fan becomes zero [3]. Figure 2-4 shows the normalized total pressure loss versus logarithm of the Reynolds number. Although these results are for centrifugal turbine and compressors, it is expected to have a similar behavior in axial machines.

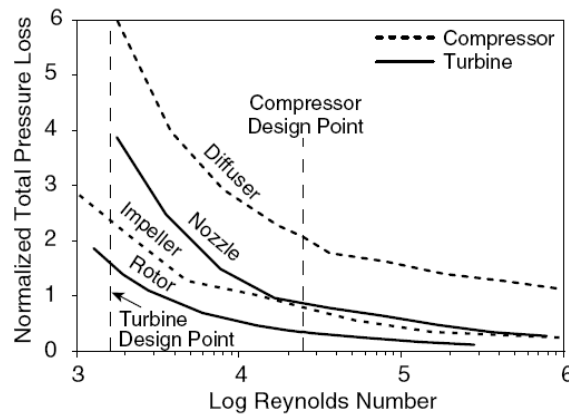


Figure 2-4 Calculated sensibility of 2-D airfoil loss with Reynolds number [15]

However, there are also some phenomena that do not depend on the size of the machine. Separation and the effects of centrifugal forces are such phenomena [3]. Scaling down results in a lower Reynolds number which implies that it is difficult to diffuse the flow without separation [2].

One approach to delay the separation caused by low Reynolds number flow is to control the diffusion in the blade and vane passages airfoil by increasing the thickness [16, 17]. Figure 2-5 shows the turbine designed using this technique. The design trade-off is between thick trailing edges (which add loss to the rotor) or high rotor exit angles (which result in reduced work at constant wheel speed, increased diffuser loss, and reduced operating range). However, this technique is only applicable for centrifugal machines.



**Figure 2-5** A 500 m/s tip speed, 8 mm diameter centrifugal engine compressor- An unusual thick airfoil is visible [17].

Another practical method is to use corona discharge which can be utilized to control boundary layer separation [18]. The principle of using corona discharge is illustrated in Figure 2-6.

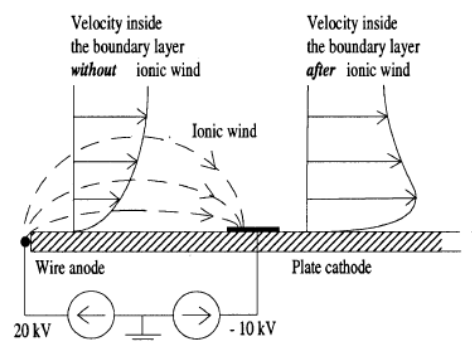


**Figure 2-6** Schematic side view of the wanted influence of an ionic wind on the air flow velocity inside a 2D laminar boundary layer[18]

Figure 2-7 shows the visualized flow and the effect of corona discharge on boundary layer thickness.

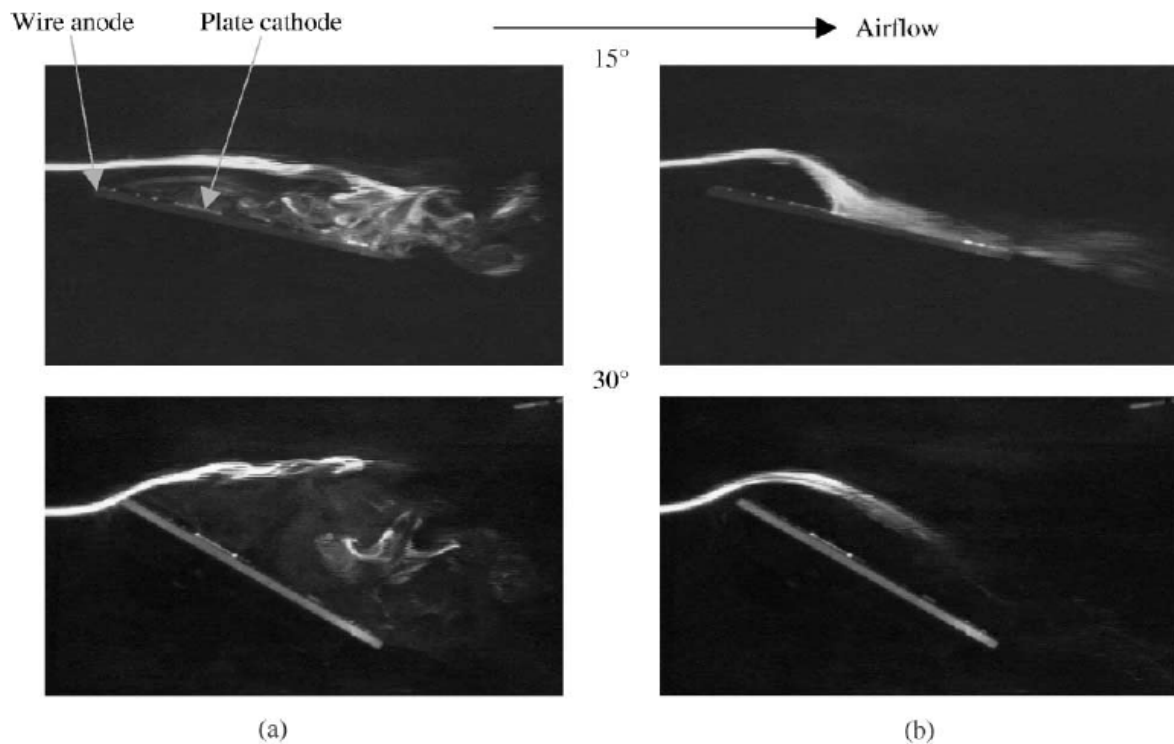


Figure 2-7 (a) Visualization of air flow at 0.35 m/s ( $Re = 3750$ ) around a flat plate for two angles of attack (15° and 30°) without corona discharge; (b) same experiments with corona discharge [18].

## 2.3 Aerodynamics

### 2.3.1 Introduction

An efficient fan should transfer most of its energy effectively to the fluid particles through the rotor blades. Hence, interaction between the blades and air is of critical importance. This interaction depends on the shape of the blade (airfoil), relative velocity magnitude and direction.

Working at the macro- or micro-scale is also a critical factor that should be considered. There is no difference in thermodynamic consideration between micro- and macro-systems. But the physics and mechanics, which influence the shapes of components, change at micro-scale. Therefore, the optimal design is different for macro- and micro-scale turbomachines [2].

Viscous forces are highly dependent on the scale of the machine. The viscous drag is relatively large in microsystems due to the small length scale [15]. Other than the increase of viscous forces and higher surface area-to-volume ratio at the micro-scale, manufacturing constraints at the micro-scale should be taken into account; current micro fabrication technology is limited mainly to two-dimensional, planar geometries. Hence, some laws are not applicable when turbomachines and engines are scaled down geometrically. For example, the cube-square law: where the airflow and thus the power decreases with the intake area (the square of the linear size) while the weight decreases with the volume of the engine (the cube of the linear size) dictates that the power-to-weight ratio increases linearly as the engine size is reduced. As the specific power is very small for the micro-scale devices, the actual scaling is not correct [19].

In addition, in conventional machines where the physical dimensions are bigger than one micron, the flow can be assumed to be continuum flow [2]. Conventional design procedures are valid for continuum flows and may not be applicable for the design of small fans. Hence, modifications may be necessary.

In this section, a brief introduction to airfoils is presented and a conventional fan design procedure is briefly described.

### **2.3.2 Airfoil**

When fluid particles flow pass a solid body, the resulting pressure distribution gives rise to lift and drag forces. The drag force is parallel to the free stream air flow and the lift force is perpendicular to the free stream direction. A two-dimensional lifting surface with a lift to profile drag ratio of 10 or more can be considered as an airfoil [20].

Geometrical properties of airfoils, including chord line, camber line and angle of attack, have critical effects on the lift and drag forces. The chord line is defined as the distance between the leading and trailing edges. The angle of attack is the angle between the relative air velocity and the chord line. The camber line is a line that divides the airfoil profile into two parts and is drawn midway between the upper and lower surfaces. For flat plate airfoils, the camber line and chord line coincide with each other. These properties are illustrated in Figure 2-8.

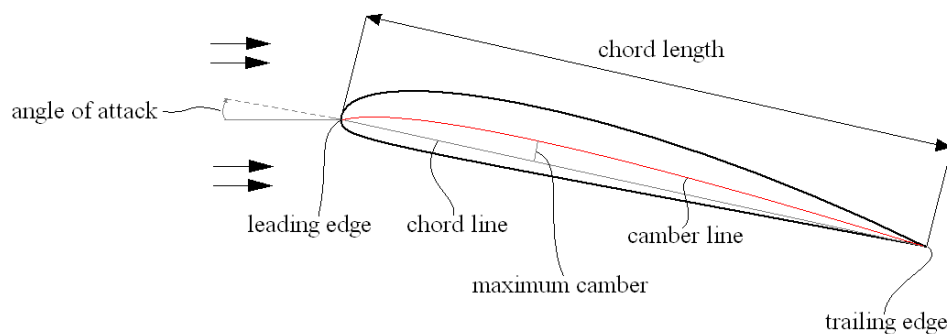


Figure 2-8 airfoil and its properties

When the camber line is straight, the airfoil is symmetrical but such airfoils are rarely encountered in fan design as rotors [20].

Many attempts have been made in airfoil designing and shape optimization including using numerical computational codes [21-23]. There are many different kinds of airfoils and each family is developed for a specific purpose. Most of them are designed for the aircraft industry where manufacturing expediency is the key factor in determining the selected airfoil.

### 2.3.2.1 Lift and Drag Forces

As mentioned previously, the lift and drag forces are two perpendicular components of force exerted by the fluid on the airfoil and are parallel and perpendicular to the relative velocity vector respectively. The lift force is a function of the angle of attack. This relationship is determined empirically and Figure 2-9 shows the lift coefficient for different angles of attack for cambered plate airfoils.

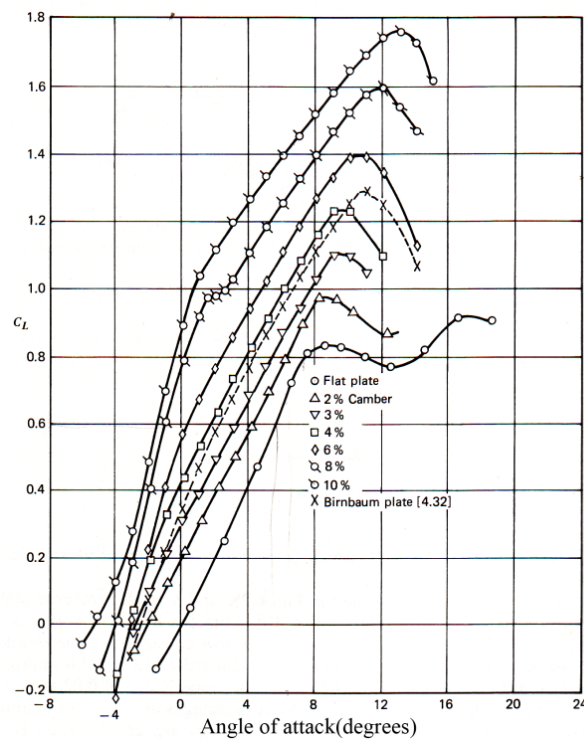


Figure 2-9 Cambered plate lift data,  $Re= 3 \times 10^5$  [20]

The lift coefficient,  $C_L$ , drops drastically when stall occurs. Stall is the result of flow separation at the upper surface of the airfoil for high angles of attack.

The factors that affect the maximum lift and the drag forces are maximum thickness of chord ratio, the chordwise position of maximum thickness and the leading edge radius. However, the general lift properties are determined by the camber line.



The lift force,  $L$ , can be normalized as the lift coefficient which is defined in equation(2.4).

$$C_L = \frac{L}{\frac{1}{2} \rho U^2 A} \quad (2.4)$$

where,  $\rho$  is the free stream density,  $U$  is the free stream velocity and  $A$  is a reference area.

For 2-D airfoil this area is defined in equation (2.5), where the depth is assumed to be unity.

$$A = 1 \times c \quad (2.5)$$

and,  $c$  is the chord length of the airfoil.

The drag force is also an important factor in airfoil design. In a similar way to the lift coefficient, the drag coefficient can be defined by equation (2.6) as:

$$C_D = \frac{D}{\frac{1}{2} \rho U^2 A} \quad (2.6)$$

where,  $D$  is total drag force and  $A$  is calculated using equation (2.5).

In 2-D airfoil analysis, the total drag is the profile drag. In 3-D model another component of the total drag force, called the secondary drag will have to be considered. It is a result of vortices formed at the tip of airfoils with finite span [20]. Profile and secondary drags will be explained in section 2.3.4.

### 2.3.3 Conventional fan design

A schematic fan is shown in Figure 2-10.

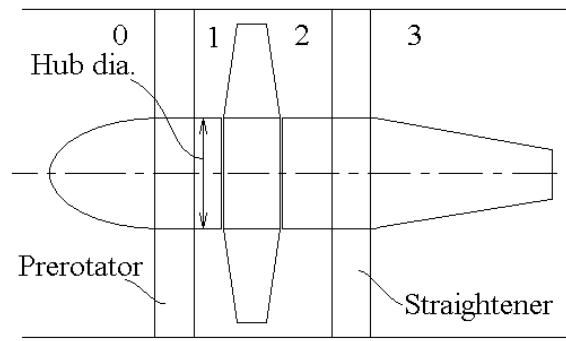


Figure 2-10 Schematic general blading case

From Figure 2-10, the Bernoulli relationships at the four stations (0, 1, 2 and 3) are

$$H_0 = P_0 + \frac{1}{2} \rho V_a^2 \quad (2.7)$$

$$H_1 = P_1 + \frac{1}{2} \rho V_a^2 + \frac{1}{2} \rho V_{\theta_p}^2 \quad (2.8)$$

$$H_2 = P_2 + \frac{1}{2} \rho V_a^2 + \frac{1}{2} \rho V_{\theta_s}^2 \quad (2.9)$$

$$H_3 = P_3 + \frac{1}{2} \rho V_a^2 \quad (2.10)$$

where  $H$ ,  $P$ ,  $V_a$ , and  $V_{\theta}$  are the total pressure, static pressure, axial velocity component, and swirl velocity component, respectively. The assumption is that there is constant total pressure at each cross-sectional plane. The total pressure difference is

$$H_3 - H_0 = \Delta H_{th} - \Delta h_R - \Delta h_P - \Delta h_s \quad (2.11)$$

where  $\Delta H_{th}$  is the theoretical mean total pressure rise. The other terms correspond to losses in the rotor, prerotor blades and straighteners, respectively. Prerotators and straighteners are elements found in bigger-size fans that are used to improve flow quality.

After normalizing the equation with  $\frac{1}{2}\rho\bar{V}_a^2$  equation (2.12) is obtained:

$$\frac{H_3 - H_0}{\frac{1}{2}\rho\bar{V}_a^2} = K_{th} - k_R - k_P - k_S \quad (2.12)$$

where  $\bar{V}_a$  is the axial mean velocity and  $k = \Delta h / (\frac{1}{2}\rho\bar{V}_a^2)$ .

After some substitutions and using the definition as below,

$$\varepsilon = \frac{V_\theta}{V_a} \quad (2.13)$$

We have,

$$P_2 - P_1 = \Delta P = \frac{1}{2}\rho\bar{V}_a^2 (K_{th} - k_R + \varepsilon_p^2 - \varepsilon_s^2) \quad (2.14)$$

Subscripts  $p$  and  $s$  refers to upstream and downstream of the rotator respectively.

The work output done by the rotor in the elementary annulus is

$$W_o = (H_2 - H_1).(2\pi r)V_a dr \quad (2.15)$$

The work input in the same annulus is

$$W_i = \Omega dT \quad (2.16)$$

where  $\Omega$  is rotational speed (radians per second) and  $dT$  is elemental torque. Using the expression for the rate of change of angular momentum, we have

$$dT = \rho V_a (2\pi r dr) (V_{\theta_s} + V_{\theta_p}) \quad (2.17)$$

After substitution and simplification we have

$$\Delta H_{th} = \rho \Omega r (V_{\theta_s} + V_{\theta_p}) \quad (2.18)$$

This quantity can be expressed non-dimensionally as:

$$K_{th} = \frac{2}{\lambda} (\varepsilon_s + \varepsilon_p) \quad (2.19)$$

where  $\lambda$  is defined as

$$\lambda = \frac{\bar{V}_a}{\Omega r} \quad (2.20)$$

Thus,

$$K_{th} = \frac{\Delta H_{th}}{\frac{1}{2} \rho \bar{V}_a^2} \quad (2.21)$$

The tangential velocity component ( $V_t$ ) of the air relative to the blade is given by

$$V_t = \Omega r - \frac{1}{2} (V_{\theta_s} - V_{\theta_p}) \quad (2.22)$$

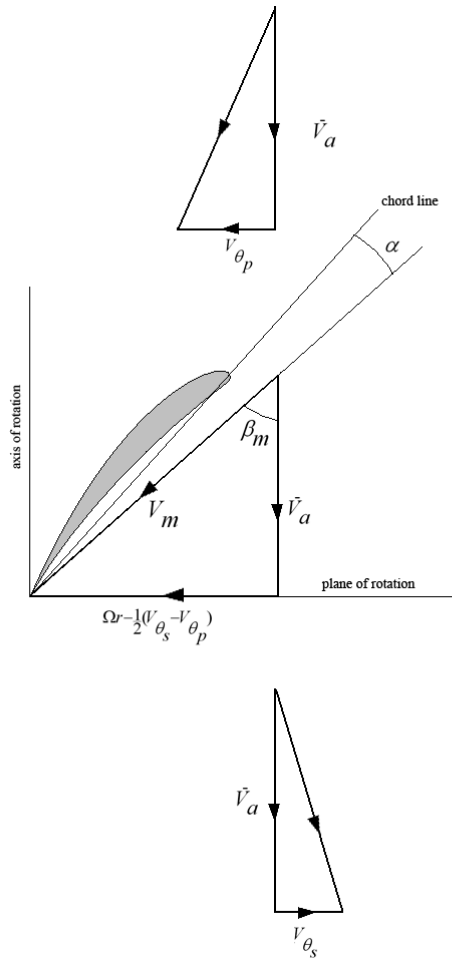


**Figure 2-11 Relative velocity vectors and the airfoil**

As shown in Figure 2-11, the angle between the resultant velocity and the plane of rotation is

$$\tan \beta_m = \frac{\Omega r - \frac{1}{2}(V_{\theta_s} - V_{\theta_p})}{\bar{V}_a} \quad (2.23)$$

or

$$\tan \beta_m = \frac{1 - \frac{1}{2}(\varepsilon_s - \varepsilon_p)}{\lambda} \quad (2.24)$$

The relation between  $\beta_1$ ,  $\beta_2$  and  $\beta_m$  is,

$$\tan \beta_m = \frac{1}{2} (\tan \beta_1 + \tan \beta_2) \quad (2.25)$$

As shown in Figure 2-11,  $\beta_m$  is the angle that the vector mean of  $V_1$  and  $V_2$ , namely  $V_m$ , makes with  $\bar{V}_a$ .

After calculating  $\beta_m$ , the blade angle can be determined using equation (2.26)

$$\xi = \beta_m - \alpha \quad (2.26)$$

where  $\alpha$  is angle of attack of the airfoil (blade cross section). These angles are shown in Figure 2-12.

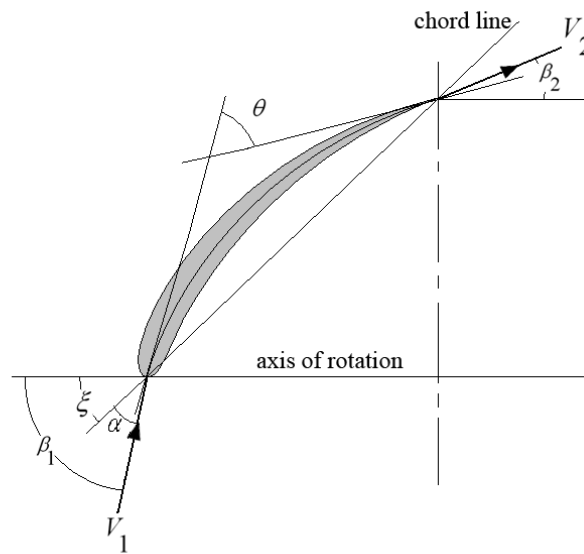


Figure 2-12 Geometric details of airfoil

By using the momentum equation, the drag coefficient can be determined as:

$$C_D = \frac{2}{\sigma} k_R \cos^3 \beta_m \quad (2.27)$$

In the same way,  $C_L$ , after some simplification, is,

$$C_L = \frac{2}{\sigma}(\varepsilon_R + \varepsilon_P) \cos \beta_m \quad (2.28)$$

To satisfy the condition for free vortex flow, it is usual to make one of  $\varepsilon$ 's equal to zero.

The lift coefficient,  $C_L$ , is usually an empirical quantity. Therefore, after calculating  $C_L\sigma$  from equation (2.28), the solidity,  $\sigma$ , can be obtained. The chord length, for different  $r$ , is obtained from equation (2.29)

$$c = \frac{2\pi\sigma r}{n} \quad (2.29)$$

where  $n$  is the number of blades.

### 2.3.4 Drag Force

Drag forces are generated by several mechanisms. Drag forces are usually undesirable not only in fan blades but also in every structure having fluid-structure interactions, as they decrease the efficiency of the flow processes. Decreasing the drag forces is one of the objectives that designers try to achieve in order to have an efficient product.

Because of the sizes considered in this project and the unusual shape of blade cross-section, it is important to decrease drag forces. A brief description of different drag forces are presented below.

#### 2.3.4.1 Profile Drag

As implied by its name, the source of this drag is the airfoil profile. This drag arises from skin friction and pressure forces. The difference in pressure between the upstream and downstream of the airfoil affects this drag. Skin friction is the effect of friction on the surface of the airfoil. The sources of skin friction and pressure drags are the tangential and normal

stresses, respectively. There are some variables that influence this force, including profile shape, surface roughness, blade solidity, Reynolds number and air turbulence [20].

When boundary layer separation takes place, the static pressure on the rear of the airfoil is sharply reduced. This phenomenon is the main cause of stall. The surface roughness is another factor which affects the profile drag. In general, the drag increases as the surface roughness increases.

Tests on a flat plate over the range of Reynolds number  $1.5 \times 10^5$  to  $4.0 \times 10^5$ , show no significant change in the drag force [24]. Hence for most practical purposes, the drag coefficient will not be subjected to variation with the Reynolds number [20].

#### **2.3.4.2 Secondary Drag**

There are other mechanisms that create drag force for finite span airfoil. The main phenomenon that causes secondary drag is the tip vortex. This vortex propagates downstream and is eventually dissipated as heat [20]. Vortices are also shed from the trailing edge along the entire span. There are other losses in ducted fans which are categorized as secondary drag. Some relations are available to approximate secondary drag coefficient that are derived by different researchers [20]. Secondary drag losses are generally associated with three-dimensional effects of the blade.

#### **2.3.5 Cordier diagram**

The Cordier diagram is used to determine the air flow,  $Q$ , and the pressure generated,  $\Delta P$  for turbomachines. The Cordier diagram [25, 26] is an empirical diagram which relates the specific speed,  $n_s$  and the specific diameter  $d_s$  for efficient turbomachines.



It was found that turbomachines, with high efficiencies tend to cluster along the Cordier line.

The Cordier diagram is shown in Figure 2-13 [26].

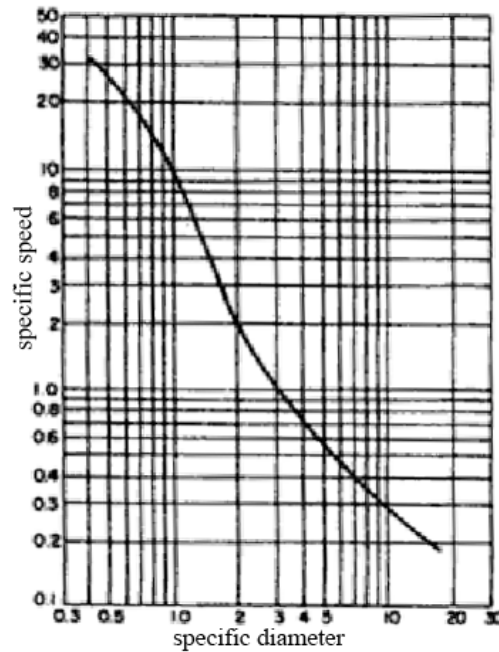


Figure 2-13 Cordier diagram

Using dimensional analysis for turbomachines handling incompressible fluid, it can be shown that the specific speed depends only on the specific diameter. The Cordier line serves a good guide for designer to select efficient geometrical parameters for their designs.

The specific speed,  $n_s$ , is defined as equation (2.30).

$$n_s = \frac{\omega \sqrt{Q}}{(gH)^{\frac{3}{4}}} \quad (2.30)$$

where  $\omega$  is rotational velocity,  $Q$  is the fluid flow rate,  $H$  is the head produced and  $g$  is the gravity acceleration.

The specific diameter,  $d_s$ , is defined as equation (2.31).

$$d_s = \frac{D(gH)^{\frac{1}{4}}}{\sqrt{Q}} \quad (2.31)$$

where  $D$  is the outer diameter.

Using the Cordier diagram is a reliable way to have an efficient design. As a qualitative guide, this diagram can also aid the designer to determine the type of turbomachine needed for a given specification.

### 2.3.6 Physical Properties at Micro-Scale

Some physical properties related to micro machines are sensitive to the size and have different values at micro- and macro-scale. As the size decreases, elastic, plastic and heat condition behaviours do not change, while fracture strength, creep, and oxidation rates can change [2]. Different physical properties at micro-scale cause a different criterion for material selection. Moreover, the electrical and mechanical properties of the materials used in MEMS technology, generally, change during the fabrication process. In addition to the change of some physical properties, micro fabrication constraints also affect the material selection criterion. However, it is important to note that in some micro machines where the size is relatively big, continuum mechanics can still be applied.

## 2.4 Fan Testing

Generally, pressure generated for different flow rates are measured for fan testing. For in-line fans, the fan total pressure should be measured (FTP)[20]. The diagram of the fan total pressure, which is the summation of fan static pressure (FSP) and fan velocity pressure (FVP), drawn against flow rate is representative of fan characteristics.

The appropriate test data presentation for geometrically similar fans is presented in Figure 2-14. From these simple relationships, the desired performance curves can be constructed for any combination of fan size, speed and air density. However, strict non-dimensional similarity in construction is essential. For example, the shape of blades, blade clearance and surface roughness should be non-dimensionally similar. However, the diagram is for commercially sized fans where the Reynolds number is higher than 100,000.

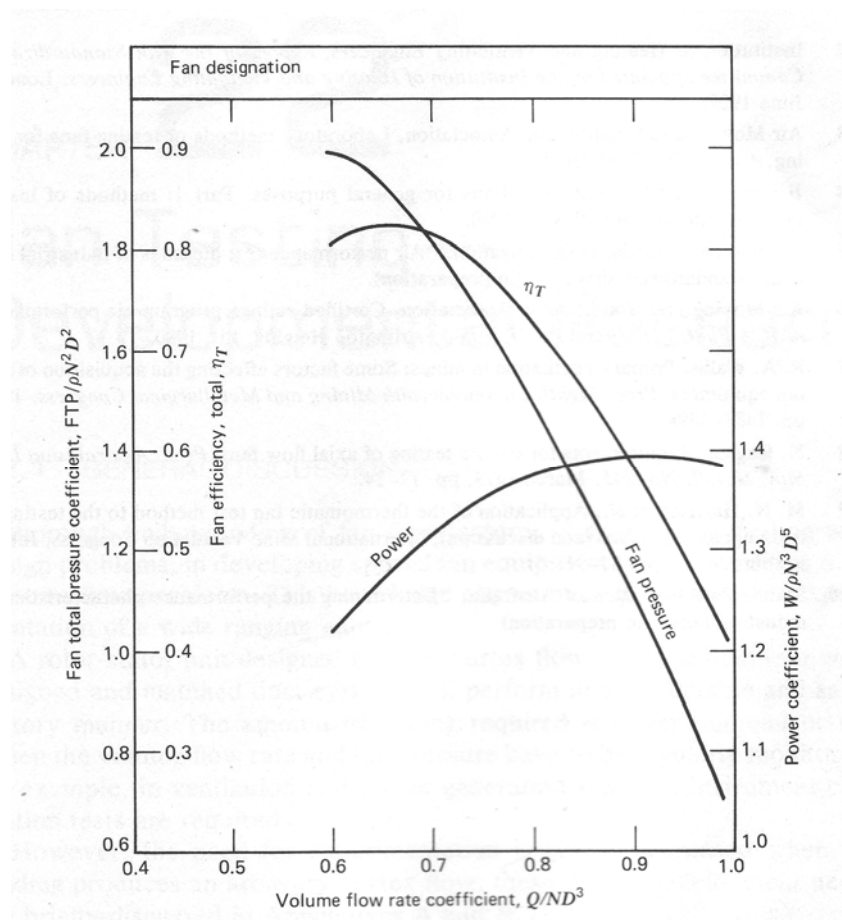


Figure 2-14 A non-dimensional presentation of test data[20]

As the Reynolds number decreases and the boundary layers become laminar, the efficiency of the fan becomes sensitive to Reynolds number [3]. Hence, the non-dimensional presentation of the fan performance (Figures 2-3 and 2-14) may not be useful.

## 2.5 Fabrication

Fabrication process is one of the major factors that affect the design. Micro-fabrication techniques are chosen to fabricate the designed fan. The fabrication limitations, e.g. inability of fabrication of smooth channels and turnings using micro-fabrication techniques, cause a big effect on turbomachine performance. A 5% decrease in compressor efficiency and 15% in mass flow is reported for a 2 mm diameter inlet when the smooth turning is changed to a right-angle one by 3-D CFD simulation [17]. Designing, based on micro-fabrication limitations, enables us to miniaturize the product without changing the design techniques; the only thing that should be improved for a smaller product is the fabrication techniques.

There are many fabrication technologies and each of them has its own limitations. In order to have an efficient product, these limitations should be considered. In addition, the costs availability of the facilities should also be considered in the selection for appropriate fabrication method. UV (Ultra Violet) lithography was selected in this project because it is not costly and, moreover, desired products can be fabricated with acceptable accuracy using this method. SU-8 (the photoresist in this project) has many advantages, e.g. being suitable for layer-by-layer structures.

In this section, a literature review on micro-fabrication technologies for 3-D products, the polymer SU-8 and previous attempts and projects on micro-fabrication is presented.

### 2.5.1 3-D Micro-fabrication

The abilities and accuracy of micro-fabrication technology are increasing rapidly. Micromachining enables the fabrication of complex small parts with submicron precision. Using photolithography-defined method results in high fabrication speed and many parts can be fabricated simultaneously.

However, photolithography can basically produce 2-D micro parts and layer-by-layer fabrication should be exploited to fabricate 3-D structures using photolithography.

Several 3-D micro fabrication techniques have been developed such as IH Process (Integrated Harden Polymer Stereo lithography) [27], advanced microstereo lithography named as Super IH process [28, 29], a combinational method using microstereo lithography and UV lithography[30, 31], using Microloading Effect for Micromachining 3-D Structures of Nearly All Shape (MEMSNAS) [32], moving mask LIGA (an abbreviation for German words: Lithographie, Galvanoformung, Abformung) process [33], inclined UV lithography [34], inclined/rotated UV lithography [35], Two-Photon lithography [36-38], Proton Beam Writing (PBW) system [39] and Electron Beam lithography [40].

In the lithography fabrication methods, the first step consists of coating the wafer with a light-sensitive material called photoresist. Photoresist is a polymer with its properties changing when it is exposed to UV light or X-rays. The exposure area is defined according to the selected process. This exposure in proper pattern can be made using a mask or by direct optical or e-beam writing. After solidification of the photoresist, the required parts, which is highly dependent on the fabrication process, will remain and the other parts will be removed. Two types of photoresists are used in photolithography techniques: negative and positive. For the negative photoresists, the solubility of the exposed area decreases and for the positive photoresists, the solubility of this area increases.

IH process is a layer-by-layer method, which uses UV to solidify the polymer similar to conventional stereo lithography at the macro scale [27, 28]. In this method, UV light is focused on the surface of the polymer and the 3-D structure is fabricated layer by layer.

Super IH process is an advanced IH process. In this method the polymer solidifies at a pinpoint position (into the liquid polymer) that UV light is focused. Although super IH process does not use layer-by-layer process [28], the final fabricated product is similar to layer-by-layer made products. The main advantage of super IH process is that fabricating a support for the product is not necessary.

The principle of the combinational method using microstereo lithography and UV lithography is layer-by-layer polymerization of a liquid resin [31]. SU-8, a negative photoresist is used in this method. Using SU-8 in this technique results in unique characteristics like smooth and vertical walls. This process can also be used as a post-processing step on planar structure with no need to micro assembly manipulation [31]. Through this method, a product having more than 1000 layer can be fabricated [30].

Microloading Effect for Micromachining 3-D Structures of Nearly All Shape (MEMSNAS) is a hole-area modulation method where microloading effect of reactive ion etching (RIE) is used in order to obtain multiple levels of heights in an array of microholes of different diameters [32]. This method uses the microloading effect. By using a mask with different openings, different depth can be obtained because the etching rate on larger holes is faster. Therefore, 3-D shapes can be fabricated. After removing the mask, the surface will be etched **again** and the produced surface will be smoother.  $SF_6$  is used as etchant [32]. The mask in this method has uniform hole-distribution but the sizes of the holes are different. A model is derived to calculate the size and distribution of the openings in order to make the mask.

However, this model can be considered as a first order model only and a more accurate model is needed. The most important limitation is that this method is not suitable to fabricate very small products, i.e. smaller than  $50\ \mu\text{m}$  [32]. Other limitations are that high slope walls and high aspect ratios cannot be made by MEMSNAS.

Moving mask deep X-ray lithography (M<sup>2</sup>DXL) is proposed to produce more flexible and precise controllability for cross-sectional micro structures [33]. In this method, both mask movement and X-ray exposure energy are controlled. An “inverse approach” is also proposed, using the Fourier transform technique, to achieve optimum mask movement which avoids try-and-error approach in the mask design. Although this technique overcomes many problems, it is not possible to make any arbitrary 3-D micro-structures.

The inclined UV lithography is another technique for 3-D fabrication. It was firstly reported using thick positive photoresist [34].

As another method for 3-D micro-fabricating, the inclined/rotated UV lithography [35] can be used. This method is suitable to make oblique structures. As the name implies, this method uses inclined UV lithography and by rotating the substrate to make some special geometries such as inclined cylinder. SU-8 is used as the photoresist. Oblique cylinder, embedded channels, bridges, V-grooves and truncated cones are made by this method [35].

Two-Photon lithography [36-38] is also a method that can be used to fabricate 3-D complicated and oblique walls. A limitation is low throughput due to the sequential nature of the laser scanning process [36].

The Proton Beam Writing (PBW) system uses existing scanning system with external beam positioning and fast beam switching system [39]. The negative photoresist SU-8 was used because of its suitable mechanical properties and proper sensitivity for charged particles with

energies of few MeV and steep contrast curve (the ratio of cross linked material to density of deposited energy for proton beam irradiation). Although the fabricated structures can be categorised as 3-D, they do not have any deviation from normal vector of the substrate plane. This limitation causes this method not to be suitable for fan blade fabrication.

The electron beam lithography uses different doses of electron beam to solidify SU-8 in different depth to fabricate 3-D sub-micro-structures [40]. By utilising this method, self-supporting structures can be fabricated. After some modifications, the light intensity can be controlled spatially and greyscale electron beam lithography [41] is developed. However, in this method, a sensitive control of exposure and accurate condition controlling are required, which cause this method to be costly.

### 2.5.2 Other fabrication methods

Other than the methods described in the proceeding section, some other fabrication methods and technologies, which may not be categorized as 3-D fabrication methods, can be exploited to produce a 3-D product. Flip-chip [42] and solder self-assembly [43, 44] technologies are two methods that can be utilized to make some 3-D structures. In addition, surface micromachining and rotary scratch drive actuator (SDA) motors are also used in fabrication of micro-axial fans [1, 45].

Two different types of fans were developed by Linderman et al. [1]. These two fans are illustrated in Figure 2-15. In the fabrication of one of them flip-chip technology was exploited and for the other one, predetermined blade angles were adjusted by solder self-assembly technology. In both approaches, the substrates can be further reduced in size, and consequently in weight, by bulk etching, leaving only a thin structural layer to support the motor and fan blade arrays [1]. As an advantage, for using solder assembly, the specific blade angle can be achieved by controlling the condition and using different forms of locks [43].



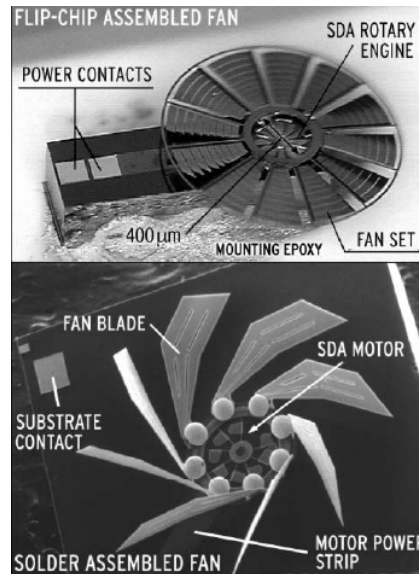


Figure 2-15 Flip-chip (top) and solder assembly (bottom) micro-fans[1]

### 2.5.3 SU-8

SU-8 is a negative, epoxy-type, near-UV photoresist with very high epoxy functionality which was developed by IBM [46]. This material is used either as the main structure material or as a mould for electroplating [46, 47] in fabrication of micro-structures and MEMS devices. Flexibility in processing and not being very expensive, are major factors that cause this polymeric material to be chosen as a useful material for several applications related to micro fabrications. This polymer was also used for fabrication of biologically inspired artificial compound eyes [48].

SU-8 has the capability of being used to fabricate structures of high aspect ratios and high thicknesses. Having high aspect ratio and ultra thick resists are very important, especially in electronic sensors and actuators, fluid channels and micro robots [49]. There are two methods employed to fabricate high-aspect-ratio parts using SU-8. The first one is LIGA process that uses deep X-ray lithography [33, 50-52] and the second one is UV lithography [53-58].

However, because of the absorption of UV light by the resist and the optical refraction occurred in that medium, the highest achievable aspect ratio by UV lithography is about 25:1 (height:width). Since X-ray can penetrate deeply into most materials, 100:1 structures are obtained using deep X-ray lithography [51]. Moreover, as another advantage of SU-8, high aspect ratio holes and trenches can also be obtained [56]. In recent years, ultra-high aspect ratios (191:1) and very thick micro structures have been fabricated using UV-lithography [59]. Fabrication of a six-layer micro structure with the overall thickness of up to 500 microns, using the method of UV lithography on SU-8 2100 and 2010 is presented in the research conducted by Mata et al. [60]. The layers do not have the same thicknesses and some layers are only 10 microns thick.

UV lithography has shown great potential for industrial applications. In spite of more accurate and smoother products using X-ray LIGA, the cost considerations are the main disadvantage for X-ray LIGA compared with the UV lithography fabrication. The UV lithography needs only standard lithography equipments instead expensive synchrotron X-ray source in LIGA.

In some cases, multiple photolithographic steps of exposure and development are performed to develop complex and multi-layer SU-8 features [61, 62]. As mentioned before, SU-8 is used for many different fabrication technologies. Although initially developed for UV photolithography, SU-8 has been successfully extended as a resist for X-ray, e-beam and two-photon lithography [37, 53].

#### ***2.5.3.1 SU-8 characterization***

For a successful fabrication process, one needs to know the accurate values of physical properties of SU-8. Many investigations have been carried out to determine these values. Basically, the concentration of the solvent affects the properties, e.g. the range of achievable

thicknesses. Friction coefficient and modulus of elasticity are obtained in the reported research by Lorenz et al. [56]. A comprehensive characterization of mechanical and thermal properties, such as bi-axial modulus of elasticity and coefficient of thermal expansion, is carried out in [58]. The optical properties of photoresists like refractive index of SU-8, which has a critical importance in the lithography accuracy, is characterized by Sum et al. [63]. The UV transmission for layers with different thicknesses (varying from 5 to 375  $\mu\text{m}$ ) have been measured and the coefficient of absorption for  $\lambda = 365 \text{ nm}$  is calculated [31]. Recently, the bond strength between SU-8 and gold is investigated by pull test experiment in different conditions [64].

#### ***2.5.3.2 SU-8 applications in micro-channels***

SU-8 is widely used to fabricate devices related to micro-fluidics. In these cases, SU-8 polymer epoxy photoresist is the main structural material. Being cheap and simple, SU-8 is numerously used in micro-channel fabrication. This polymer is very useful in embedded micro-channel fabrication, e.g. a 3-D interconnected micro channel with high aspect ratio and smooth wall [65]. To produce a multi-layer embedded micro channel employing dosage-controlled UV exposure, the bottom surface of each layer is coated by an anti-reflection material to prevent the solidification of SU-8 in undesired areas caused by reflected UV light [66].

#### ***2.5.3.3 SU-8 and high-thickness layers***

In the fabrication of micro-structures with thickness up to 1mm, some errors occur at the side wall profiles of micro-structures because of UV diffraction error in liquid photoresist. This error results in T-shaped walls. One way to avoid this problem is to minimize the effect of air gap between the photomask and photoresist by using glycerol as an index match to eliminate the UV light diffraction as illustrated in Figure 2-16 [49]. This method minimizes the

diffraction error which is a result of the Fresnel diffracting. Despite its simplicity, this method is very useful and the wall pattern with error decreased from 45% to almost zero percent [49].

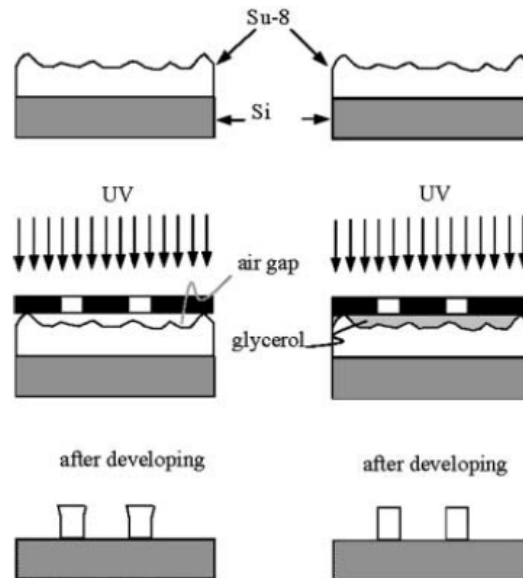


**Figure 2-16** Fabrication comparison of standard SU-8 process (left), and glycerol filled process (right) [49]

In UV lithography, other index matching liquids, such as Cargille, are also used for ultra-high aspect ratio structure fabrication [59]. Cargille index matching liquid is slightly better than the effect of glycerine, because of having a better matched refractive index with SU-8.

Another way of reducing the defects caused by UV diffraction is placing a soft cushion under the substrate [67]. By applying an additional force onto the backside of the wafer contact is improved. This method is illustrated in Figure 2-17.

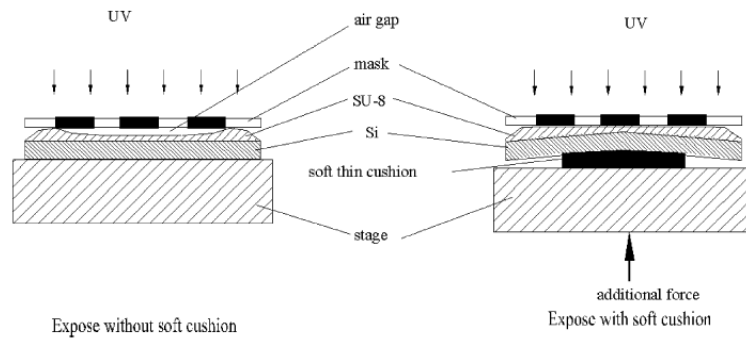


Figure 2-17 Effect of the soft cushion during exposure [67]

#### 2.5.4 UV Lithography on SU-8

The steps involved in the photolithographic process are, basically, wafer cleaning, photoresist application, soft baking, mask alignment, exposure, development, and hard-baking. A flow-chart in the Figure 2-18 shows these steps in more details.

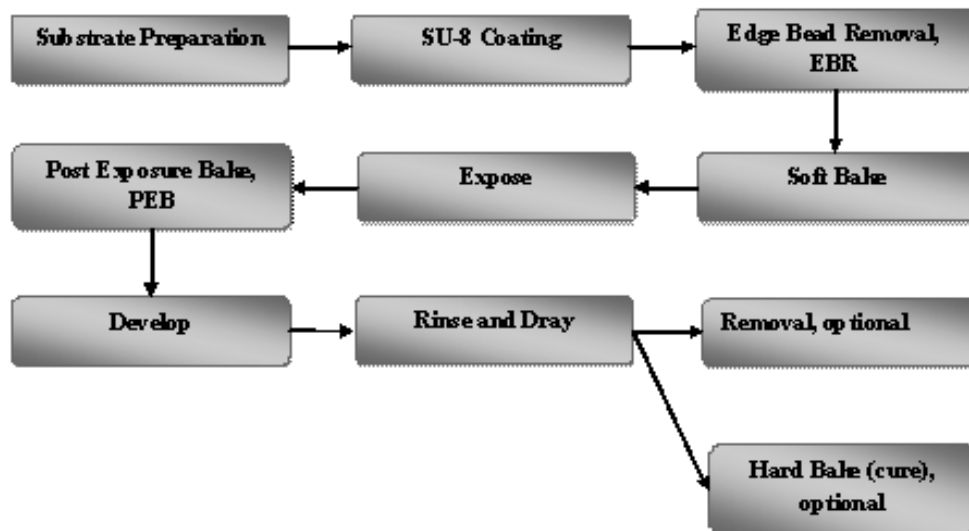


Figure 2-18 The procedure of UV lithography

These steps will be explained in more details according to the chemical standards provided by the manufacturer (MicroChem Corp.).

#### 2.5.4.1 Substrate Preparation

To obtain maximum process reliability, substrates should be clean and dry prior to applying SU-8 2000 resist.

#### 2.5.4.2 Coat

1ml of resist (SU-8 2000) for each inch (25mm) of substrate diameter should be dispensed on the wafer. Then, the wafer will be rotated to reach a specific rotational speed with a given acceleration. After some time as specified in the standards, the wafer will be rotated at a higher speed. The latter is to obtain a uniform thickness coat.

SU-8 2000 is available in twelve standards. The required information for coating is available in the corresponding catalogue. Figure 2-19 shows spin speed versus thickness for some standards of Su-8 2000 which are suitable for this project.

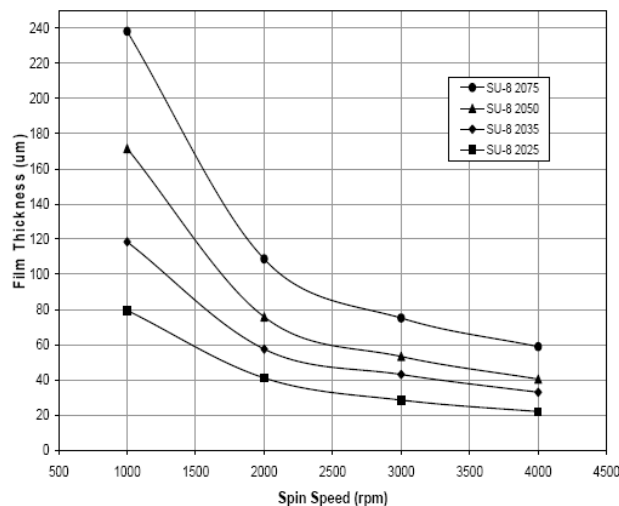


Figure 2-19 spin speed against film thickness for different SU-8 resists

As one can see in Figure 2-19, different types of SU-8 2000 is characterized using a number added to 2000, e.g. 75 or 50. This number roughly shows the order of thickness that can be achieved.

#### ***2.5.4.3 Edge Bead Removal (EBR)***

During the spin coat process step, a build-up of photoresist may occur on the edge of the substrate. In order to minimize contamination of the hotplate, this thick bead should be removed. By removing any edge bead, the photomask can be placed into close contact with the wafer, resulting in improved resolution and aspect ratio.

#### ***2.5.4.4 Soft Bake***

After the coating, the resist should be heated according to manufacturer's catalogue. A level hotplate with good thermal control and uniformity is required for use during the Soft Bake step of the process.

#### ***2.5.4.5 Exposure***

The photoresist should be exposed by UV for a specific time. The time of the exposure depends on several factors, such as the material of the substrate, the thickness of the layer, the type of the photoresist, and the position of the layer, i.e. the exposure time for the layers at the top, in multi-layer structures, is less than the exposure time of the first layer (at the bottom) [60].

#### ***2.5.4.6 Alignment***

Alignment is critical for multi-layer structures. Some specific patterns are printed on the mask for this purpose. These alignment marks enable us to align the position and the angle of the mask and the wafer.

#### *2.5.4.7 Post Exposure Bake (PEB)*

For some photoresists, including SU-8, a post exposure heating is required. The polymerization of the SU-8 will be completed during the post exposure heating.

#### *2.5.4.8 Development*

The redundant parts should be removed from the product. Developers are used to solve the unexposed parts of SU-8. In multi-layer structures, a single development can be done after the exposure is done for all layers [60, 68-70]. Besides reduction in processing time, simultaneous development causes and increase in coating uniformity compared to a process that coats over the topography of previous patterned layers [60].

High-aspect-ratio micro structures often require optimization of development time and agitation, while low-aspect-ratio features have less sensitivity to development parameters [71]. However, vigorous agitation of the SU-8 Developer may be destructive for high-aspect-ratio structures [72].

In this chapter a review of cooling devices is presented. The scaling and aerodynamics of fans are also examined. Finally micro-fabrication techniques for making miniature fans are also briefly covered. In the next chapter, the design of miniature fan will be presented.



## 3 Design and Fabrication

### 3.1 Introduction

In this section, the design procedure is described. As previously stated, our design is based on the Cordier diagram and the conventional fan design method as described in [20]. Although this design method is used for relatively large axial fans, it has been adopted because there is a lack of a proper method for designing small fans; most existing small fans are designed based on scaled down version of conventional fans. Due to the size of the fan, the lift and drag coefficients may be different. Therefore, numerical analysis has been carried out to determine these essential quantities for fan blade design.

Although it may not be sufficiently accurate, using the Cordier diagram for choosing a reasonable specific diameter and speed in the design step can help to have a first estimate about the flow rate and pressure generated. The computed pressure generated and flow rate will be used in the design and also in the numerical analysis. During the design process, for a given diameter and rotating velocity, some other assumptions and approximations were also made and are presented below.

An important point that should be considered is that the size of the device influences the flow mechanism [2]. For small fans operating at very low Reynolds numbers, the effect of scaling cannot be ignored. Moreover, geometrical constraints are also very critical in very small fans [2]. Therefore, modifications will be carried out on the initial design to improve its performance.

A critical assumption in conventional design techniques is that fluid flow is in the turbulent regime, which means that the corresponding Reynolds numbers are much higher than the critical Reynolds number. A commonly reported value of the critical Reynolds is  $2 \times 10^5$  with marked performance penalties below  $1 \times 10^5$  [20]. This Reynolds number is calculated based on chord length. In this project, although the rotational speed is very high, i.e. 10000 rpm, the Reynolds number is much lower than the critical Reynolds number.

### 3.2 Design Procedure

In this project, it is assumed that the Cordier diagram is applicable for very low Reynolds numbers turbomachines ( $Re < 100$ ) though the original Cordier diagram was derived based on commercial sized machines.

In the design process, the desired generated pressure is obtained using the Cordier diagram. It is also assumed that the blade section is designed for the mean radius and there is no twist in the blade section.

$Q$  and  $\Delta P$  can be obtained using non-dimensional quantities defined by equations (2.30) and (2.31) and can be written as:

$$Q = \left( \frac{\omega}{n_s} \right) \left( \frac{D}{d_s} \right)^3 \quad (3.1)$$

and

$$\Delta P = \rho \left( \frac{\omega}{n_s} \right)^2 \left( \frac{D}{d_s} \right)^2 \quad (3.2)$$

During the design procedure, some other quantities have also been determined. These quantities are the local flow coefficient,  $\lambda$ , the mean pressure coefficient,  $K$ , the local swirl coefficient,  $\varepsilon$ , the angle between the relative mean velocity and the chord line,  $\beta$ , the blade angle,  $\xi$ , the blade solidity,  $\sigma$ , and the chord length,  $c$ .

The local flow coefficient,  $\lambda$ , is calculated for the mean radius using equation (2.20). The local swirl coefficient,  $\varepsilon$ , is calculated using equation (2.19). As mentioned previously, either  $\varepsilon_p$  or  $\varepsilon_s$  are assumed to be zero in the design procedure. In this design,  $\varepsilon_p$  is assumed to be zero. Hence,

$$\varepsilon_s = K \frac{\lambda}{2} \quad (3.3)$$

and  $K$  can be calculated using equation (2.21) where  $\Delta H$  is the mean total pressure change between two given points.

To calculate  $\Delta H$ , it is assumed that the difference between the  $V_{\theta_p}^2$  and  $V_{\theta_s}^2$  (in equations (2.8) and (2.9)) is negligible and, therefore,  $\Delta H$  can be estimated as the static pressure difference,  $\Delta P$ .

If equations (2.21) and (2.20) are substituted into equation (3.3), the local swirl coefficient,  $\varepsilon_s$ , can be simplified as follows,

$$\varepsilon_s = K \frac{\lambda}{2} = \frac{\Delta P}{\frac{1}{2} \rho \bar{V}_a^2} \frac{\bar{V}_a}{2r\omega} = \frac{\Delta P}{\rho r \omega \bar{V}_a} \quad (3.4)$$

Based on the assumption  $\varepsilon_p = 0$ , equation (2.24) can be reduced to:

$$\tan \beta_m = \frac{1 - \frac{1}{2} \varepsilon_s \lambda}{\lambda} \quad (3.5)$$

Using equations (3.4) and (2.20) the following expression can be obtained:

$$\varepsilon_s \lambda = \frac{\Delta P}{\rho r \omega \bar{V}_a} \frac{\bar{V}_a}{r \omega} = \frac{\Delta P}{\rho (r \omega)^2} \quad (3.6)$$

hence,

$$\tan \beta_m = (1 - \frac{1}{2} \varepsilon_s \lambda) / \lambda = (1 - \frac{1}{2} \frac{\Delta P}{\rho (r \omega)^2}) \frac{r \omega}{\bar{V}_a} \quad (3.7)$$

Equation (3.7) can be rearranged using equation (3.2) as,

$$\frac{\bar{V}_a}{r \omega} \tan \beta_m = 1 - \frac{\left(\frac{\omega}{n_s}\right)^2 \left(\frac{D}{d_s}\right)^2}{2(r \omega)^2} \quad (3.8)$$

And the axial velocity can be obtained if the dimensions are specified.

$$\bar{V}_a = \frac{Q}{A} = \frac{Q}{\frac{1}{4} \pi (D^2 - D_h^2)} \quad (3.9)$$

where  $D_h$  is the hub diameter.

As our goal is to design a fan of diameter 5 mm and a hub diameter of 1.5 mm, the axial velocity can be computed. Using equation (3.8),  $\beta_m$  can be calculated and the blade angle can be obtained from equation (2.26) and angle of attack,  $\alpha$ , is calculated using numerical simulation which will be explained in the next chapter. For high Reynolds numbers, empirical charts are available to determine the lift coefficients for different angles of attack

and hence the best angle can be chosen. But for very low Reynolds numbers, these charts are not available and for the preliminary design  $\alpha = 6^\circ$  is assumed.

After some simplifications,  $\sigma C_L$  can be obtained from equation (2.28) as

$$\sigma C_L = 2\varepsilon_s \cos \beta_m \quad (3.10)$$

For the first estimation  $C_L$  is assumed to be equal to flat plate lift coefficient ( $C_L = 0.6$  for  $\alpha = 6^\circ$ ) but this value will be checked by numerical simulations.

The chord length,  $c$ , is calculated using equation (2.29) while the number of blades in this project is assumed to be five.

Using the Cordier diagram, we determine the pressure generated and flow rate based on different specific speeds. The results are given in Table 3-1.

**Table 3-1 Flow rates and pressure differences for given specific speeds**

$n_s$	$d_s$	$Q \left( \frac{m^3}{s} \right)$	$\Delta P (Pa)$
4	1.5	9.69E-06	0.91
6	1.2	1.26E-05	0.63
9	1	1.45E-05	0.406
10	0.9	1.79E-05	0.406
14	0.8	1.82E-05	0.262

As the specific speed,  $n_s$ , increases, the flow rate increases while the pressure generated decreases. It is clear from the Cordier diagram that, for high rotational velocities, axial turbomachines have better performance than centrifugal ones with the same dimensions.

From Table 3-1, there is no difference between the  $\Delta P$ 's for  $n_s = 9$  and  $n_s = 10$ . But the flow rate is bigger for the bigger specific speed ( $n_s = 10$ ). In a comparison between  $n_s = 10$  and  $n_s = 14$ , although the flow rate for  $n_s = 14$  is bigger, the corresponding  $\Delta P$  is much smaller. Hence, a specific speed of 10 is selected for this project.

After determining  $\Delta P$  and  $Q$  obtained from the Cordier diagram and following the described procedure, we can obtain the results that are presented in Table 3-2 and Table 3-3.

Table 3-2 Required quantities for fan design

$\omega_{(m/s)}$	$n_s$	$d_s$	$D_{(mm)}$	$D_h_{(mm)}$	$r_m_{(mm)}$	$A_{(m^2)}$	$Q_{(m^3/s)}$	$\Delta P_{(Pa)}$	$\bar{V}_a_{(m/s)}$	$n$
1046.67	10	0.9	5	1.5	1.625	1.79e-5	1.79e-5	0.4057	1.00	5

Table 3-3 Calculated quantities

$\lambda$	$K$	$\varepsilon_s$	$\beta_m(^{\circ})$	$\alpha(^{\circ})$	$\sigma$	$C_L$	$C_{(mm)}$
0.5909	0.6696	0.1978	58	6	0.35	0.6	0.72

The relative air velocity is

$$V = \sqrt{\bar{V}_a^2 + (r\omega)^2} = 1.97 m/s \quad (3.11)$$

And the Reynolds number (based on the chord length) is

$$Re_c = \frac{\rho V c}{\mu} = 85.83 \quad (3.12)$$

where  $\rho = 1.2 kg/m^3$ ,  $\mu = 1.983 \times 10^{-5} kg/m.s$ .  $V$  and  $c$  is substituted from equation (3.11) and Table 3-3 respectively.

After calculating the required angle and chord length, a pattern is needed to design the geometry according to the aerodynamic calculated results and microfabrication processes and limitation.

As mentioned previously, the blade section will be a five-layer structure made from SU-8 using UV lithography. But each two layers should have an overlap to link the layers. This overlapped area should not be very small in order to have good stability and strength.

There is no guideline to determine the overlapped area. Therefore, a method is proposed for the design. This method was employed for all geometries. This method is illustrated below. Figure 3-1 shows the chord line (length) and blade angle that are calculated during the design.

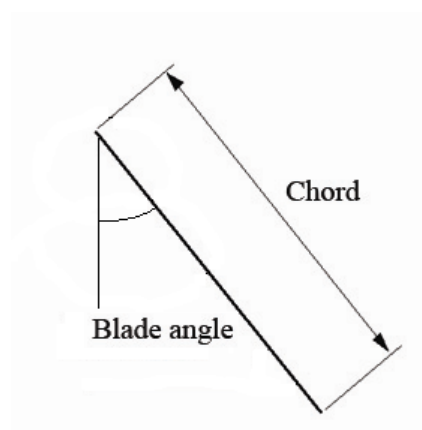


Figure 3-1 Schematic designed chord and angle

To draw the most similar layer-by-layer shape to this inclined line, a rectangle is drawn. As shown in Figure 3-2(a), the chord line is the diagonal of this rectangle. The width and length of the corresponding rectangle is divided into five sections, because, according to practical considerations, the blades, and therefore the whole fan, will be fabricated in five layers. Figure 3-2(b) shows the preliminary five layer blade section.

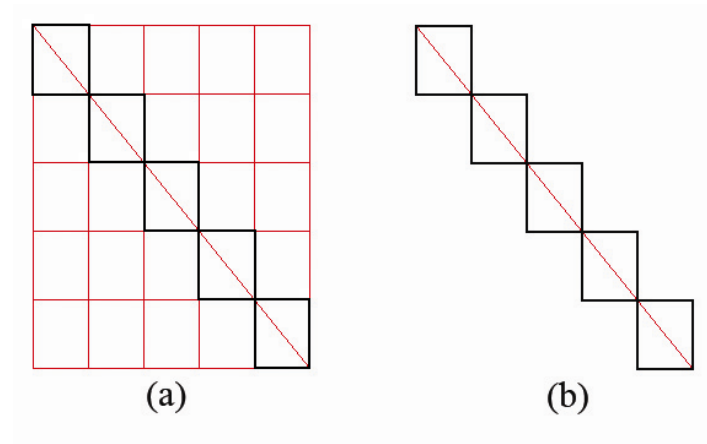


Figure 3-2 (a) Making a rectangle based on chord line, (b) Preliminary design of the cross section

The next step is to develop a procedure to make an overlapped area between layers. This area should be neither too small nor too big. If it is too small, the layers cannot be attached together very well. On the other hand if a big area is made, the section will **not be** efficient. One-fourth of the width of each layer was chosen to be added to each side. Figure 3-3 illustrates this procedure.

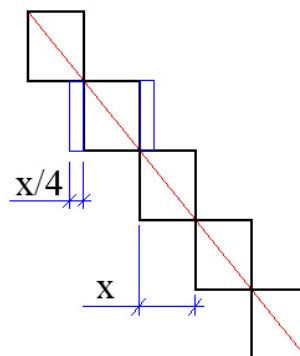


Figure 3-3 Added area to make an overlapped area

The final geometry can be seen in Figure 3-4.



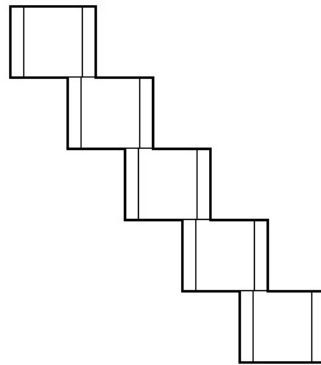


Figure 3-4 Final geometry (thick lines)

In Figure 3-4, the thick lines show the final shape of the designed cross section.

This procedure has been followed to complete the design of blade sections. The final shape of the first design (before numerical simulations) is shown in Figure 3-5.

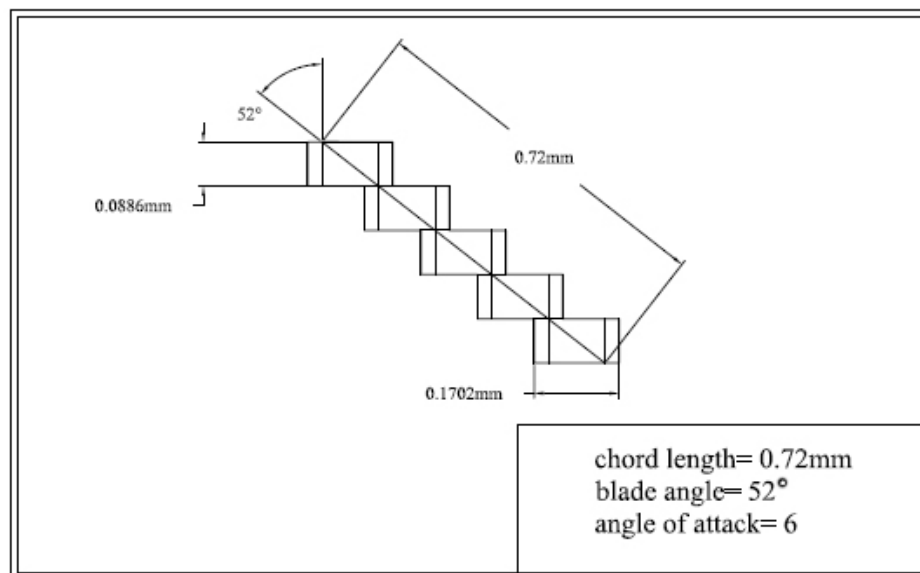


Figure 3-5 Final shape of the first design

To simulate the air flow around the cross section, the geometry is created using the Gambit software. The only difference between what is created using Gambit and the designed geometry is the omission of corners. Sharp corners, which can be seen in Figure 3-5, would cause numerical singularities in the simulations, which will result in inaccurate results. Therefore, curved corners were created instead of sharp corners as shown in Figure 3-6. The arcs are one quarter of a circle with a radius of 0.01 mm. This approach is common in overcoming the effect of singularities [73].



Figure 3-6 Curved corners

In this chapter, the design of a miniature fan is presented. Considerations are also taken in view of manufacturing constraints and, hence, modifications to the design are being proposed. In the next chapter, 2-D numerical simulation of the airfoil is being conducted to determine the appropriate angle of attack and aerodynamic performance.

### 3.3 Fabrication

In this chapter the fabrication process is explained. The designed fans were fabricated using the UV lithography on SU-8. The products have a more efficient blade profile. These profiles are obtained based on the best angle of attack for the blade with very low Reynolds number. The best angle of attack is obtained from two-dimensional numerical simulations presented in

the next chapter. Therefore, the products have modified blade profiles. A detailed explanation is available in the next chapter.

### **3.3.1 Introduction**

The fabrication process is explained in this chapter. UV lithography method was employed to make the desired five-layer products. The material of the product is SU-8. In general, SU-8 can be used as the main material or as the mold. In this project, SU-8 is the main material. SU-8 is a negative photoresist; hence it will be solidified when it is exposed by an appropriate dose of UV. Each layer of SU-8 is exposed through a specific pattern. These different patterns for different layers are drawn on different mask. Figure 3-7 illustrates the fabrication process schematically. It shows the fabrication process for the cross-section of a fan blade which is oblique. A single development step is conducted at the end. Finally, in order to detach the products from the silicone substrate, we submerged the wafer into the silicon etchant, i.e. Potassium hydroxide (KOH).

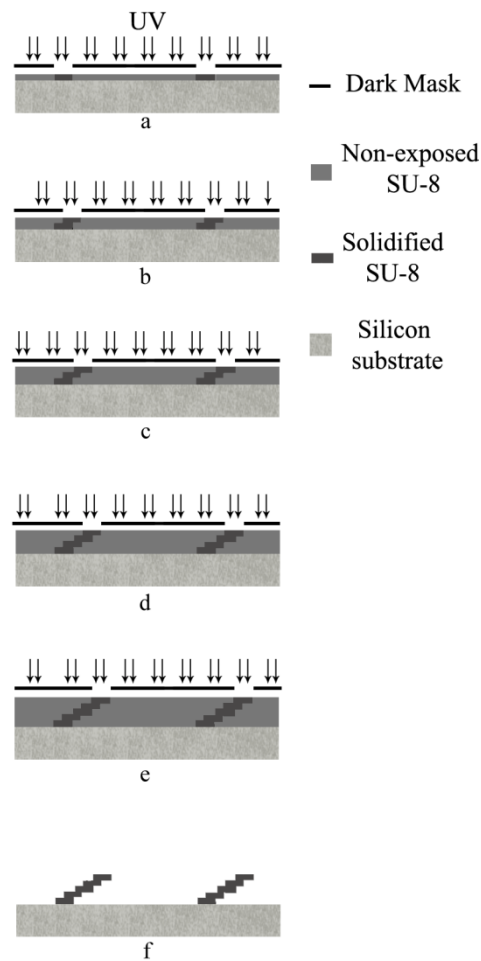


**Figure 3-7** Cross-sectional schematic diagrams of fabrication process. (a): The first layer of coated SU-8 is exposed by UV through specific patterns. (b-e): The patterns on the next masks are different, hence the ultimate products would be three-dimensional. (f): All five layers were developed simultaneously. All the areas on photoresist which are not exposed by UV are dissolved by SU-8 developer.

During the process, exposure time was altered to determine the sensitivity of the products quality to this parameter.

The procedure of this technique to fabricate a structure with five SU-8 layers is SU-8 spin coating, soft bake and exposure sequentially were introduced briefly in Chapter 2. Then a single post-exposure heating step after the last layer exposure is carried out. A single development step is conducted finally. Because the patterns on different masks have a small shift, the final product would contain oblique walls. The particular patterns on the masks are

determined by the design of the ultimate product. During the process, each SU-8 layer was exposed with its corresponding mask. This technique can be utilized to manufacture structures with complex features.

The patterns on the masks were drawn according to the modified layer-by-layer cross-sections which were designed after the 2-D numerical analyses were conducted. These analyses will be explained in Chapter 5.

The fabrication method employed, i.e. coating each layer on the non-developed previous layer and a single development step at the end of the process, has many advantageous like reduction in overall fabrication time. This technique was used in some research projects, for example in the fabrication process of an SU-8 layer-by-layer product for tissue engineering scaffolds [60, 75, 76]. However, the exploited technique in the current project has some differences like lack of post exposure baking after the exposure of each SU-8 layer.

At the end, the quality of the different products with different time of exposure and different wafer surface materials were compared together. To compare the shape of the products, several SEM (Scanning Electron Microscope) photos are presented in this chapter.

In this chapter, the fabrication procedure, dark mask preparation and the obtained results are presented.

### **3.3.2 Fabrication Procedure**

As mentioned before, in Chapter 2, the wafer and the coated SU-8 should be prepared, soft-baked, post-exposure-baked and developed in the UV lithography method to complete a single fabrication process. In the current project, the procedure is described below:

1. The alignment marks were etched at the bottom side.
2. Substrate was prepared for SU-8 coating.

3. SU-8 was spin coated.
4. The coated layer of SU-8 was heated.
5. Exposure through the appropriate mask.
6. Going to step No.3 until the last layer was coated.
7. The wafer and the photoresist layers were heated.
8. The products were developed.
9. The products were detached from the silicon substrate.

The aforementioned steps are explained below:

#### ***3.3.2.1 Bottom-Side Alignment Preparation***

The alignment marks were etched at the bottom side of the wafer to make the bottom side alignment (BSA) method feasible. To etch the required pattern at the bottom side, another lithography process was conducted.

A 5  $\mu$ m layer of positive photoresist of AZ9260 was coated on the bottom side of the wafer. AZ9260 is a positive photoresist, i.e. the solubility of exposure portions increases and they would be removed after that they were developed. Alignment marks were etched on the bottom side of the wafer using RIE (Tech Micro). Figure 3-8 shows this equipment. After the etching process is completed, the remaining photoresist was removed by acetone. These etched alignment marks were used for aligning all five layers. Bottom side alignment will be explained in more details in the section on lithography.



Figure 3-8 Etching Machine. Photo from: <http://mmc.mae.ntu.edu.sg/>

### 3.3.2.2 Substrate Preparation

To obtain maximum process reliability, the wafer should be clean and dry. Each new wafer was heated up to 100°C in a vacuum environment using Vapor Prime Process (SUSS Delta 150 VPO).



Figure 3-9 Delta 150 VPO (Vapor Prime Process). Photo from: <http://mmc.mae.ntu.edu.sg/>

### 3.3.2.3 SU-8 spin coating

In this stage, the wafer is covered by SU-8 using spin coating technique (Specialty Coating Systems Inc., P-6708). According to the catalogue prepared by the manufacturer (MicroChem Inc.), 1ml of resist should be dispensed for each inch (25mm) of substrate diameter. Hence, 4ml of the chemical is required for the used wafers which are 10cm in diameter. The spin coating parameters were set according to the data presented in the catalogue prepared by the

chemical manufacturer. The wafer was spun to 500 rpm at an acceleration of 100 rpm/s for 10 seconds. Then, in order to have a uniform surface, the speed was increased to 2500 rpm with an acceleration of 300 rpm/s for 30 seconds. This stage was repeated for all. The first stage of spin (500 rpm) is for dispensing the chemical over the wafer and the second stage (rotating with 2500 rpm) is in order to obtain a layer with uniform thickness.

#### 3.3.2.4 Soft Bake

Soft bake was done after spin coating. The wafer was heated to 65° C for 5 minutes using a hot plate. It was then heated up to 95° C for about 20-30 minutes. The wafer was left at room temperature (~ 25° C) for 10 minutes to cool down and to release stress. The required time is determined according to the Table 3-4 prepared by the chemical manufacturer.

Table 3-4 Soft Bake Time

THICKNESS microns	SOFT BAKE TIMES	
	(65°C)* minutes	(95°C) minutes
100 - 150	5	20 - 30
160 - 225	5 - 7	30 - 45
230 - 270	7	45 - 60
280 - 550	7 - 10	60 - 120

#### 3.3.2.5 Alignment and Exposure

The photoresist was exposed by UV using mask aligner equipment (Karl Suss, MA6). Figure 3-10 shows the mask aligner.





Figure 3-10 Karl Suss (MA6) mask aligner. Photo from: <http://mmc.mae.ntu.edu.sg/>

As mentioned before, bottom side alignment was used to obtain the desired result.

To use this alignment method, the wafer would be aligned with a grabbed image of the mask.

Figure 3-11 illustrates this method.

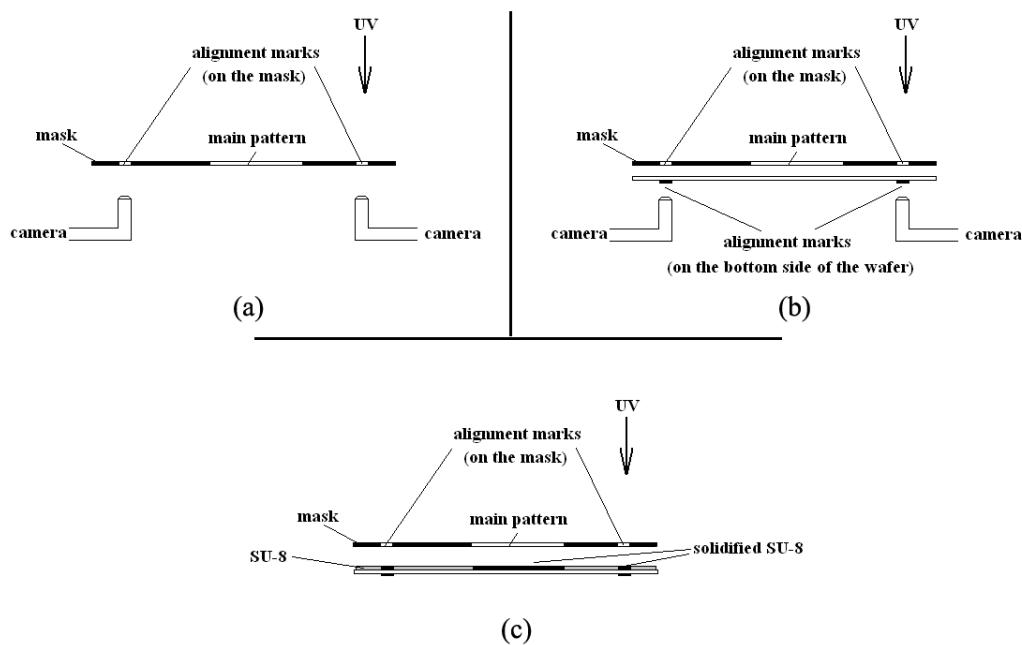


Figure 3-11 Bottom Side Alignment (BSA). (a): Mask is put at its place and the cameras take a picture from the alignment marks. The image is grabbed. (b): The wafer is situated at its place and is aligned with the mask according to the grabbed image. (c): The resist is exposed by UV light. The alignment marks have the same positions on the bottom side of the wafer and the exposed photoresist.

All five layers should be aligned with the etched marks on the bottom side of the wafer. Therefore, all layers are aligned relative to each other.

The machine was set for vacuum contact with  $10\mu$  vacuum distance. The recommended dosage of energy (by the manufacturer) was used. Required time was calculated according to the power of the machine ( $9.3 \text{ mJ}/(\text{m}^2 \cdot \text{s})$ ) and the exposure dose Table 3-5 prepared by the resist manufacturer.

Table 3-5 Exposure Dose

THICKNESS	EXPOSURE ENERGY
microns	$\text{mJ}/\text{cm}^2$
100 - 150	240 - 260
160 - 225	260 - 350
230 - 270	350 - 370
280 - 550	370 - 600

Because of the transparent nature of SU-8, UV light can penetrate it to relatively greater depths. Hence, the calculated time was applied just for the first layer and this time was reduced for the other layers. The exposure time was changed for different wafers to compare its effect. These values are presented Table 3-6.

**Table 3-6 Exposure time for different wafers**

Type	SU-8 layers	exposure time	substrate material
1	Layer No. 1 (at the bottom)	25.8 s	Silicon
	Layers No.2 to No. 5	22 s	
2	Layer No. 1 (at the bottom)	25.8 s	Silicon
	Layers No.2 to No. 5	20 s	
3	Layer No. 1 (at the bottom)	25.8 s	Silicon
	Layers No.2 to No. 5	18 s	

The exposure time for the first layer is more than the exposure time for the other layers. The reason will be explained in the section of Discussion in the current chapter.

As presented in Table 3-6, the exposure time for the substrate covered by gold is 1.5 times higher. This time is set according to Table 3-7 provided by the resist manufacturer.

**Table 3-7 Exposure Doses for Various Substrates**

RELATIVE DOSE	
Silicon	1X
Glass	1.5X
Pyrex	1.5X
Indium Tin Oxide	1.5X
Silicon Nitride	1.5 - 2X
Gold	1.5 - 2X
Aluminum	1.5 - 2X
Nickel Iron	1.5 - 2X
Copper	1.5 - 2X
Nickel	1.5 - 2X
Titanium	1.5 - 2X

### 3.3.2.6 Spin Coating of the Next Layer of SU-8 and Soft Baking

Another layer of SU-8 is spin coated immediately after the exposure. Then, the wafer is heated according to Table 3-4 assuming the thickness is equal to the thickness of the newly coated SU-8. Hence, the soft-bake time would be the same as the soft-bake time for the first layer of resist.

### 3.3.2.7 Exposure of the Next Layer

After the soft-bake process, the next exposure stage would be conducted. Bottom side alignment should be performed accurately. The exposure time is adjusted according to the explanation in part 6.2.5.

### 3.3.2.8 Post-Exposure Heating

The post-exposure bake was conducted only one time, after all five layers were exposed. The wafer was heated on a hot plate to 65°C for 5 minutes and then to 95°C for 30 minutes. The time for post-exposure heating was determined according to the manufacturer catalogue and the thickness of the whole layers as presented in Table 3-8. After heating, the wafer was left in room temperature ( $\sim 25^{\circ}\text{C}$ )

Table 3-8 Post Exposure Bake Times

THICKNESS	PEB TIME	PEB TIME
microns	(65°C)* minutes	(95°C) minutes
100 - 150	5	10 - 12
160 - 225	5	12 - 15
230 - 270	5	15 - 20
280 - 550	5	20 - 30

\* Optional step for stress reduction

### 3.3.2.9 Development

A single development step was carried out after the post-exposure bake. The wafer was submerged in the SU-8 developer (MicroChem Corp.). Because the product is quite thick, less agitation is more appropriate [72]. The development step was continued until the non-exposed SU-8 was completely moved away.

### 3.3.2.10 Detachment from the Substrate

The wafers were submerged into KOH in ambient temperature ( $\sim 25^{\circ}\text{C}$ ). The substrate is etched and the products would be detached. Because there are three different types of fans on each wafer and they are submerged in KOH after detachment, the angle of each fan has been verified using an optical microscope.

## 3.3.3 Masks

Dark field masks were used to conduct the exposure in various stages. L-Edit software was employed to create the pattern. Different layers were aligned using alignment marks. These marks are shown in Figure 3-12. Two sets of shown marks are printed on the mask to align the position and the angle of all the layers.

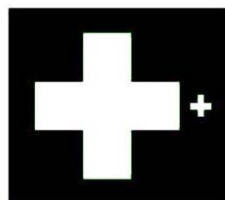


Figure 3-12 Alignment marks on the mask

As mentioned before, some parts of the pattern are slightly different. Hence, making oblique structure is possible. The patterns on different masks are illustrated in Figure 3-13.

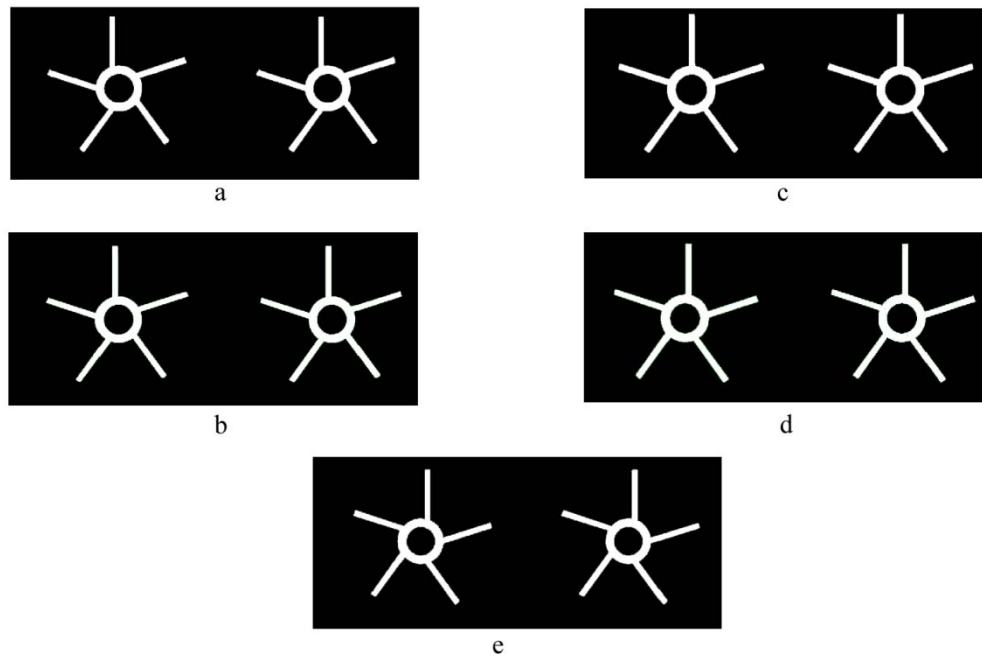


Figure 3-13 Patterns for two different fans on first to fifth mask respectively.

A photo taken from the real masks is presented Figure 3-14.

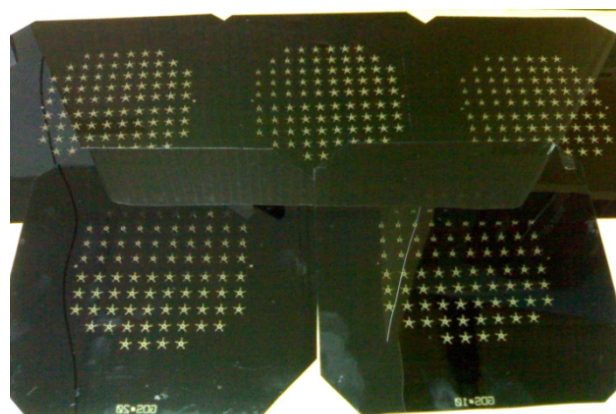


Figure 3-14 Five masks

Some SEM images and a discussion about the results are presented in the following chapter.

### 3.3.4 Results and Discussion

Several photos of the fans are presented in this chapter. The SEM images of different types (as categorized in Table 3-6).

#### 3.3.4.1 SEM Images

SEM (Scanning Electron Microscope) images of different fans with different exposure times (as listed in Table 3-6) are presented in the following sections. The SEM uses an electron beam to create a magnified image. As opposed to an optical microscope, which uses refraction of light, the SEM uses an electron beam to obtain visual magnification. The beam knocks electrons loose from the surface of the sample, where they are counted by a detector to create the image. Fans with three different angles were fabricated. SEM image of fans with an angle of attack of  $15^\circ$  is presented here and the other photos are presented in the Appendix. Some images are taken using SEM HITACHI S-3500 N with internal measurement software and some images are taken using SEM Jeol JSM-5600LV with internal measurement software.

- ***Type No.1***

An SEM image of the fan type No.1 as listed in Table 3-6, is presented in Figure 3-15. The blades are designed based on an angle of attack of  $15^\circ$ .

The exposure time for the first layer (at the bottom) is 25.8s and for the other layer is 22s.

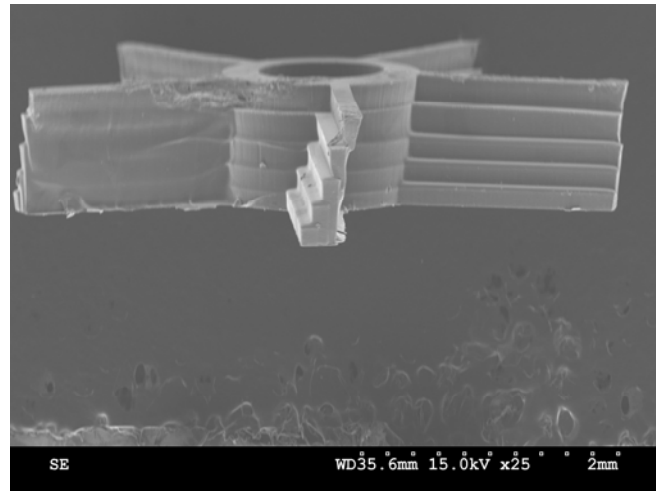


Figure 3-15 Type No.1

A closer view of the blade can be seen in Figure 3-16. The blades have the same cross-section at different radii; hence, the cross-section of the blade for this particular design is like what is illustrated in Figure 3-16 which shows the typical cross-section.

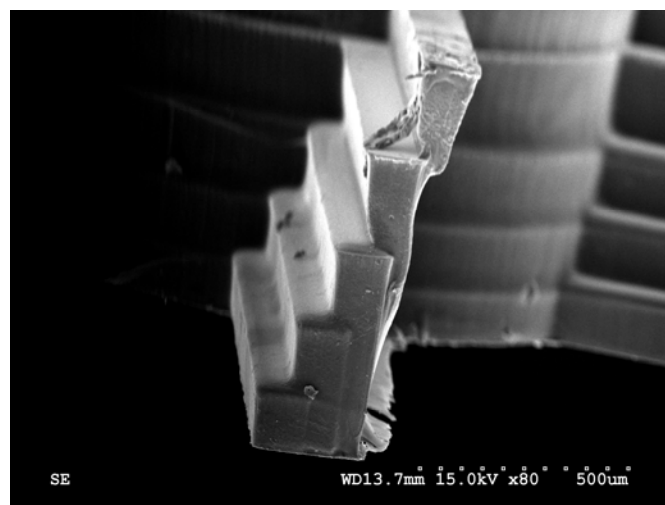


Figure 3-16 Type No.1, a closer view of the blade

- *Type No.2*



Figure 3-17 shows an SEM image of a fan design for an angle attack of  $15^\circ$ . The time of the exposure for the second layer is 20s, while the time of the exposure for the first layer is similar to the other types, i.e. 25.8s.

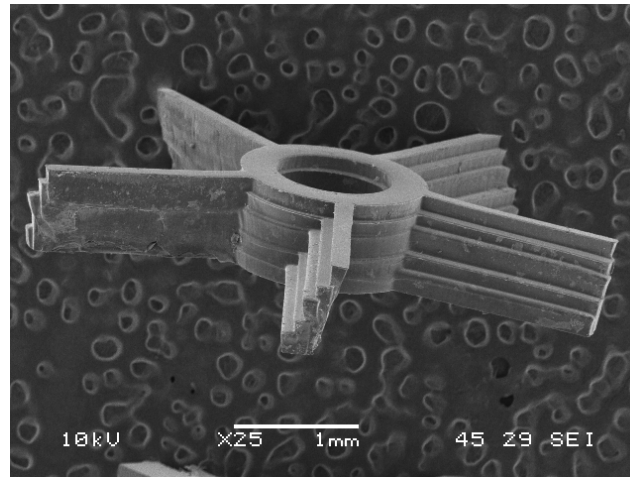


Figure 3-17 Type No.2

A closer view of the blade can be seen in Figure 3-18.

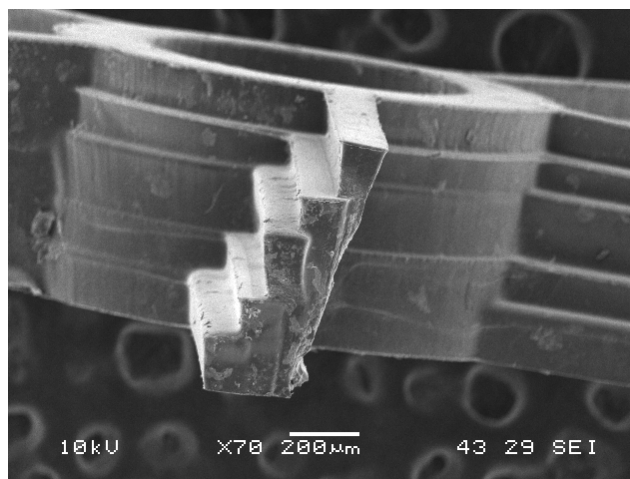
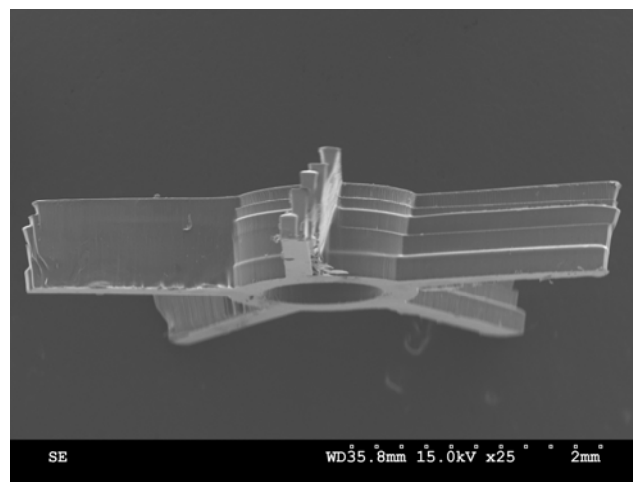


Figure 3-18 Type No.2, a closer view of the blade

The side that does not face the UV directly is smoother in the type No.2 products. This will be discussed in the in the section of Discussion in the current chapter.

- ***Type No.3***

The SEM image of the product Type No.3 is presented in Figure 3-19.



**Figure 3-19 Type No.3**

A closer view of the blade can be seen in Figure 3-20.

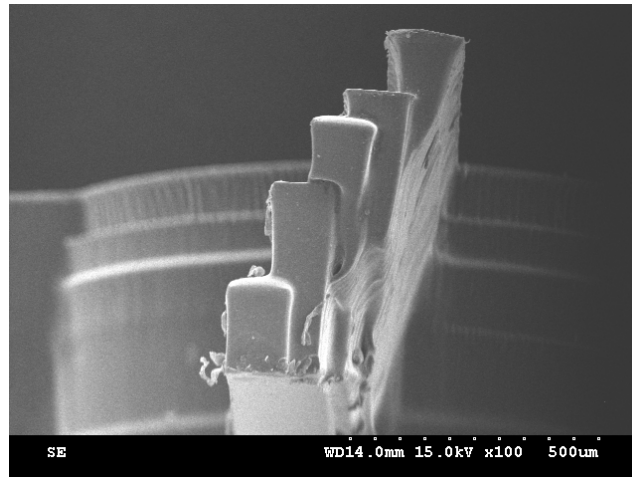


Figure 3-20 Type No.3, a closer view of the blade

The samples of this type have the best quality compared to the other types. This will be discussed in the chapter of Discussion.

### 3.3.5 Discussion

As mentioned earlier, each SU-8 layer is coated on the previous layer. Although all the parameters in spin coating such as rotational speeds, accelerations and exposure times, were the same for all layers, the thicknesses of the layers are different. It is concluded that in order to obtain more accurate products a relationship for the thickness against the speed should be determined for different layers. Moreover, the thickness of each layer of SU-8 can be measured before the exposure.

SU-8 attaches to the wafer very firmly. Hence, detachment was an important issue in this project. After the products were detached, some undesired parts were remained on the products. Figure 3-21 shows this undesired part on one of the blades.

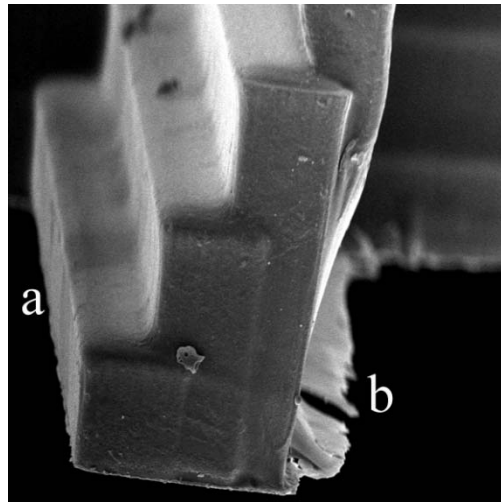


Figure 3-21 SEM image of one of the blades. (a): the side that faces the UV source. (b): the face that does not face UV source.

As illustrated in Figure 3-21, the shape of the profile is accurate in the part that is shown as (a). However, some undesired shapes are formed in the opposite side of the blade shown as (b). Non-perfect development process seems to be the main reason for this defect. Nevertheless, this defect occurs only in the side that does not face the UV source.

Another phenomenon that resulted in a deviation from ideal profile shape is the Fresnel diffraction. This phenomenon affects the size of patterns and sidewalls profile in the UV lithography printing [49]. Hence, the profile of vertical walls became V-shaped as it is shown Figure 3-22.

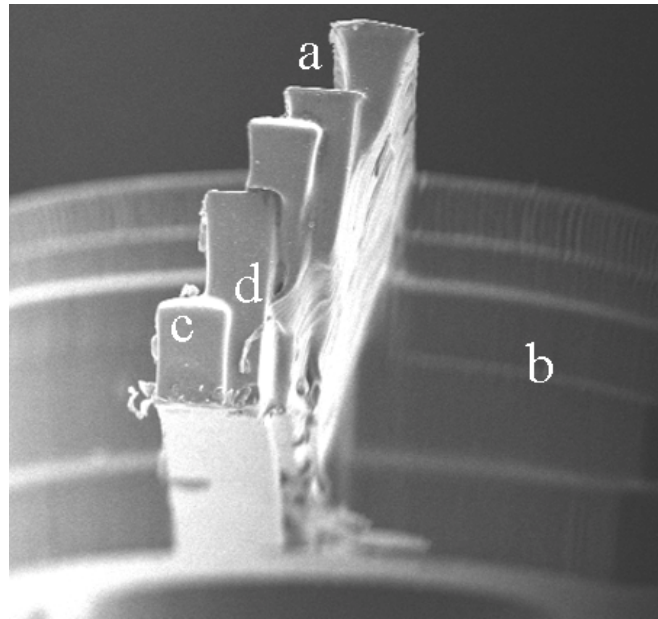


Figure 3-22 SEM image of one of the blades. (a): V-shaped profile. (b): ripples on the wall side of the hub. (c): the first layer profile is nearer to ideal profile shape in comparison to the other layers. (d): the second layer profile has a high thickness.

The diffraction error is related to thickness and the gap between the photomask and the resist[49]. Because the thicknesses of the layers are relatively large, the effect of this phenomenon is significant. One can see this error in Figure 3-22. V-shaped wall profile is marked as (a). Although the layers are aligned and the hub diameter is the same for all layers, the outer side of the hub is not smooth (Figure 3-22 (b)). The origin of this defect is the Fresnel diffraction. In other words, the profile of the each layer in hub is also V-shaped. Therefore, in spite of being aligned with the upper and lower layers, these ripples will be made.

The profile of the first layer at the bottom is quite near to ideal shape compared to the other layers profile (Figure 3-22 (c)). The second layer is thicker than the others (Figure 3-22 (d)). The reflected UV from the Silicon (or Gold) substrate seems to play the main role.

As mentioned earlier, four different fabrication processes were conducted to determine the effect of the exposure time on the quality of the products. According to Figures 3-15 to 3-20 and Table 3-6, exposure time for the second to fifth layer should be less than the exposure time for the first layer. If the exposure time for the layers which do not contact the substrate gets larger, the UV light penetrate the SU-8 in higher depth and, then, this layers will be thicker than what expected. The second and third layer (from the bottom) has this defect in Figure 3-16. Making a comparison between Figures 3-16, 3-18 and 3-20 shows that the reduction of the exposure time for the second to fifth layer, results in products with higher quality. One can see that the thickness of the third layer in Figure 3-20 (Type No.3) is not as high as the thickness of the third layer in Figure 3-16 (Type No.1).

According to SEM images, the face that does not face the UV source does possess steps. Hence, we succeeded to fabricate oblique wall using UV lithography on SU-8. Moreover, as explained above, the quality can be improved by controlling the exposure time for different layers. The exposure time for the second to fifth layer were reduced by factor of 0.7 of the exposure time for the first layer. This time can be further reduced to prevent the solidification of unwanted parts under the second layer. Nonetheless, reduction of the time exposure means that the UV dose is reduced. Hence, the lower part of the second to fifth layer would be thinner because of Fresnel diffraction and the layer may not attach to the previous layer firmly. Based on our findings, this reduction of exposure time, i.e. 0.7 of the exposure time for the first layer, is not too much and does not cause any problem in bonding between two layers. However, a series of experiment is needed to determine the appropriate exposure time for different layers with thickness.

## 4 Numerical Modelling

### 4.1 Introduction

In this chapter, the numerical modelling of the flow across two-dimensional cross-section of blades of a miniature axial fan is presented. As mentioned earlier, the simulation will show whether the designed machine would operate in an efficient condition. For this project, 2-D simulations are carried out to determine the best angle of attack and, consequently, the most efficient geometry. The FLUENT software is used as the solver of the simulation and the GAMBIT as geometry and mesh generator.

After performing several simulations, the results for different angles of attack were tabulated: the lift coefficient,  $C_L$ , the drag coefficient,  $C_D$ , and the lift drag ratio, i.e. the lift coefficient divided by the drag coefficient.

Because of the limitations in fabrication process, making the blades at any arbitrary angle is not possible. In other words, for a specific angle of attack, a specific shape can be made. However, to estimate the best angle of attack, the flow was simulated around a specific geometry at different angles of attack. The analyzed airfoil geometry is shown in Figure 3-5.

There are many uncertainties in numerical simulations. There are errors caused by the solution schemes, the lack of resolution of the computational grid, the boundary conditions specified and the initial conditions [73]. However, there are several approaches to minimize these uncertainties. Independency on mesh, a larger computation domain and choosing appropriate values for numerical parameters can minimize the effects of numerical uncertainties.

Since the resolution of the grid size is one of the most important factors that can affect the computed results, investigation of the grid refinement is necessary to determine the independency of the results on grid size. A grid-size independent solution is reached when there is very small difference in the computed variables between a coarse and a finer grid. Another important factor is the boundary conditions. Both the position and type of boundary conditions are important. The boundaries should be far enough to prevent any unphysical behaviour in the domain.

The results from simulation with  $V = 1.97 \text{ m/s}$  ( $V$  is the free stream air velocity) are used to design the fan blades. The simulations were carried out for two different grid sizes to show mesh-size independency. In this chapter, the geometries, boundary conditions and the results are presented.

## 4.2 Fan Geometry

The importance of the geometry is obvious. The geometry of the problem is a set of boundary conditions that are essential for solving a PDE. In a numerical approach, mesh properties (e.g. type, size, number, etc.), which are categorized as geometrical properties, are critical in solving the equation. Moreover, the geometry of the problem (solid borders) influences the shape and the type of the grid employed.



Mesh size can affect the accuracy of the solution and results. More accurate results would be obtained when finer meshes are used. However, using a finer mesh means spending greater computational time for a given problem. Therefore, there should be a balance between computational time and accuracy. Hence, the best choice is a mesh which is fine enough to result in a mesh-size independent solution for a given accuracy. When the difference in solutions, for finer and coarser meshes, is small, it can be claimed that the obtained results are mesh-size independent.

#### 4.2.1 Boundary conditions

In any numerical simulation, the effects of the boundary conditions are significant. Hence, boundary conditions should be selected carefully to obtain accurate results. As mentioned before, both the position and the type of the boundaries are critical in numerical modelling.

The whole domain for this project is a square that is shown in Figure 4-1.

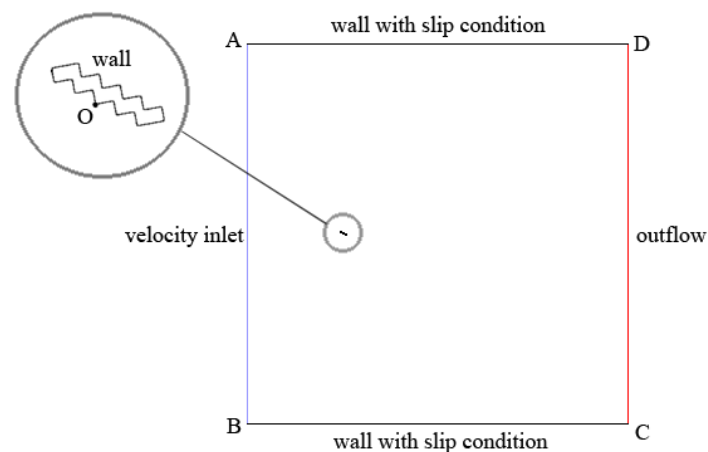


Figure 4-1 Whole domain and boundary conditions

The origin is the point O is located at (0, 0) and the coordinates of A, B, C and D are listed in Table 4-1.

**Table 4-1 Coordinates of the domain**

Points	x (mm)	y (mm)
O	0	0
A	-10	20
B	-10	-20
C	30	-20
D	30	20

The boundaries are located relatively far from the airfoil to avoid any undesirable effect on the results. The results (presented in the next chapter) confirm that the domain is big enough.

The boundary conditions are indicated in Figure 4-1. For the upper and lower boundaries and the airfoil, the condition “wall” is chosen in the FLUENT software. “Wall” is representative of a solid boundary with no normal velocity component on its surface. For the upper and lower boundaries, slip conditions were selected to avoid the effect of the shear stress applied by these walls on the flow field. But for the airfoil, no-slip condition is necessary.

#### **4.2.2 Mesh Generation**

Generally, meshes are categorized in two major types: structured and unstructured. Structured grids can be generated algebraically. In structured grid, each cell usually has four sides. Structured grid generation methods are based on mapping, i.e. the problem domain is mapped into another domain called computational domain. This mapping helps us to solve the problem (e.g. Navier-Stokes equations) numerically. In such grids, a nodal point can be related to other points by adding or subtracting integer values from its index number [74]. There are a few methods to generate structured grid. Although this type of grids results in

more accurate solution, they are not applicable in solving problems with complicated geometries.

In contrast to structured grids, an unstructured node can be related to its surrounding nodes by a connectivity matrix [74]. Unstructured grid technology allows a general computer code to be written that can handle complex geometries. Another benefit is the ability to adaptively refine the mesh in areas that contain complex flow structures [74].

In this project, unstructured, triangular meshes were generated using the GAMBIT software. The whole meshed domain (coarser mesh) is presented in Figure 4-2.

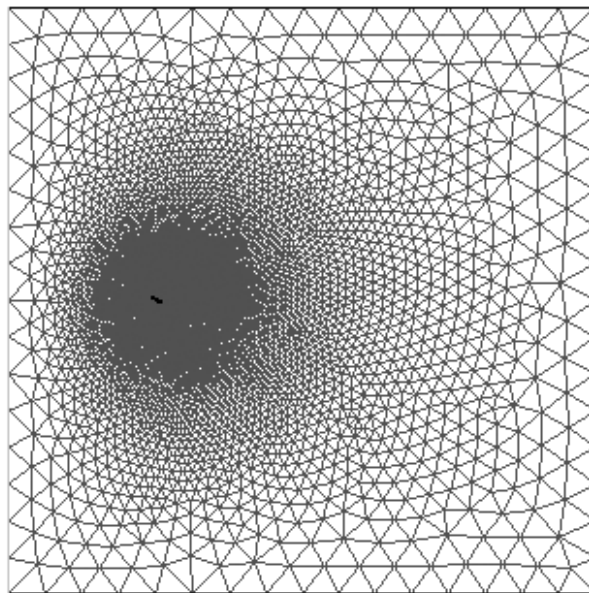
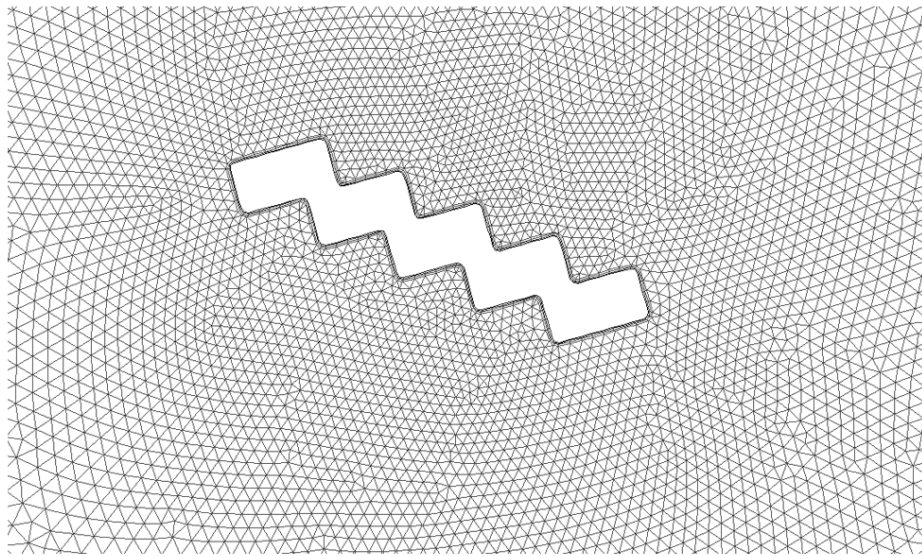
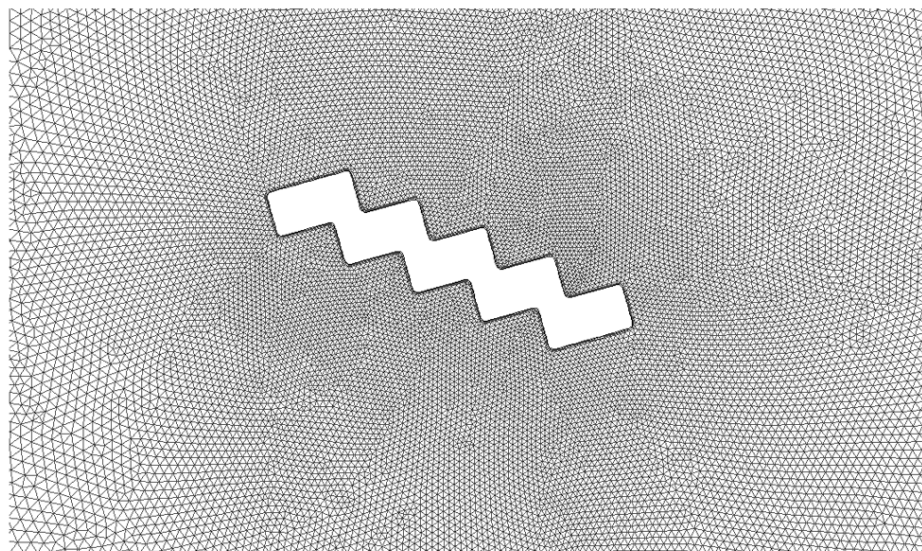


Figure 4-2 Whole domain, coarse mesh

Two different mesh-sizes were generated to show the independency of the results on the mesh size. The coarser and finer meshes (around the airfoil) are shown in Figures 4-3 (a) and (b) respectively. A boundary layer mesh was also generated around the airfoil to have smaller cells near to the solid surface in order to obtain more accurate results.



(a)



(b)

Figure 4-3 (a) Coarse and (b) fine mesh. Angle of attack=  $20^\circ$

The number of cells for geometry with an angle of attack of  $20^\circ$  is 21830 for the coarser mesh and 78526 for the finer mesh. For other angles of attack, although the numbers of the cells are not exactly the same, they are very closer to these numbers.

### 4.2.3 Numerical Simulation

A series of 2-D simulations were carried out. The flow was assumed to be steady. A laminar flow model was chosen as the Reynolds number (based on equation (3.12)) shows that the flow is laminar. The Second Order method was selected for pressure discretization. For the momentum calculation, the Third-Order MUSCL was selected in FLUENT.

As described previously, the upper and the lower boundaries were defined as “wall” with the slip condition. All simulations are conducted for  $V = 1.97 \text{ m/s}$  (where  $V$  is the free stream air velocity). The results for an angle of attack of  $15^\circ$  are presented in details. The results for the other angles of attack are presented in tables and diagrams at the end of this section and the Appendix B. The lift and drag coefficients are calculated according to equations (2.4) and (2.5).

Residuals, as the solution history and the convergence criterion, are presented. The default value for the convergence criterion parameter in the FLUENT software is  $10^{-3}$ . However, in this project, we selected  $10^{-5}$  to obtain better results.

Figure 4-4 shows a comparison between the obtained lift coefficients for coarse and fine meshes.



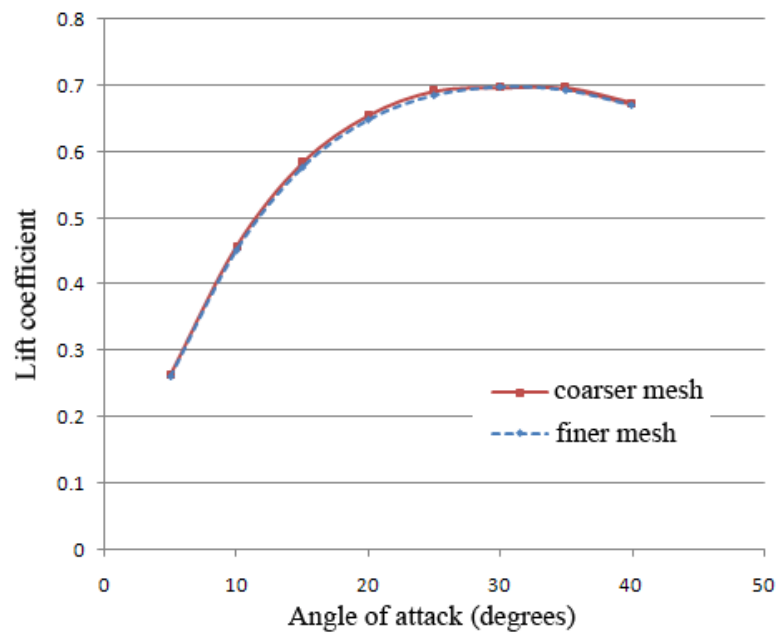


Figure 4-4 The lift coefficient for coarser and finer meshes

The results for these two meshes of different sizes agree very well. Therefore, the results can be claimed to be mesh-size independent.

In the next chapter, the results obtained from numerical simulations will be presented. Suggestions on modifications of the blade geometry are also made and their effects on aerodynamic performances are also addressed.

## 5 Design Modification

In this chapter, the results obtained from CFD simulations are presented. The results for an angle of attack of  $15^\circ$  degrees are presented in details while the results for other angles of attack are presented in Appendix B.

### 5.1 Results for Angle of attack= $15^\circ$

The results for an angle of attack of  $15^\circ$  will be presented. The residuals, the velocity and pressure contours are shown in Figures 5-1 to 5-6.

It can be seen that convergence is achieved after approximately 3000 iterations. Default value for the convergence criterion parameter in the FLUENT software is  $10^{-3}$  for residuals. However, in this project  $10^{-5}$  was selected to obtain more accurate results.

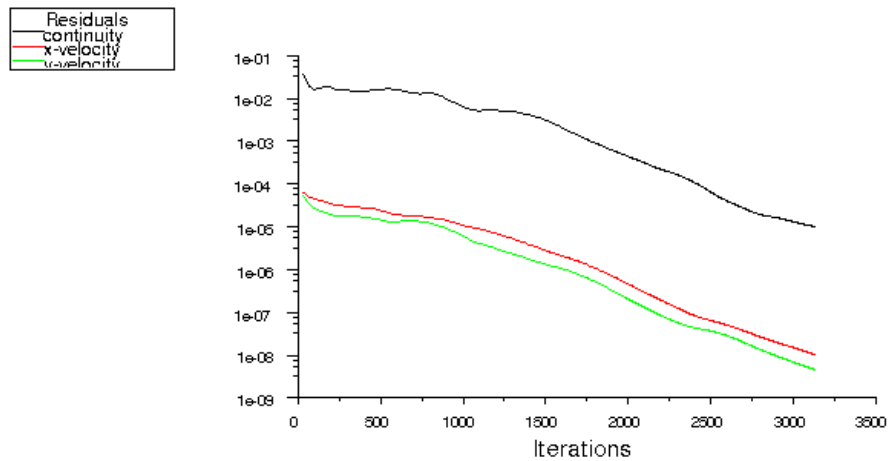


Figure 5-1 Residuals, angle of attack=15°

The velocity contour is illustrated in Figure 5-2.

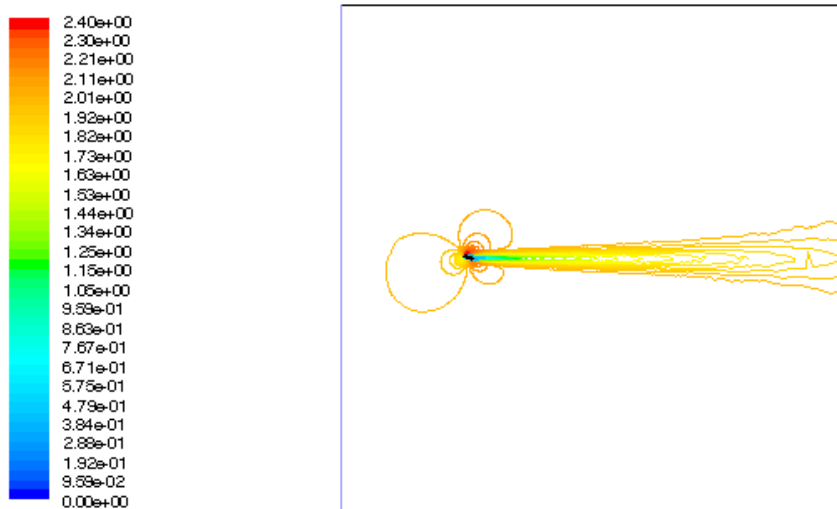


Figure 5-2 Whole domain, angle of attack=15°

According to Figure 5-3, the velocity at the inlet is equal to the velocity at the upper and lower walls. This shows that the domain size is large enough and the upper and lower walls do not affect the flow around the airfoil. A closer view is illustrated in Figures 5-3 and 5-4.



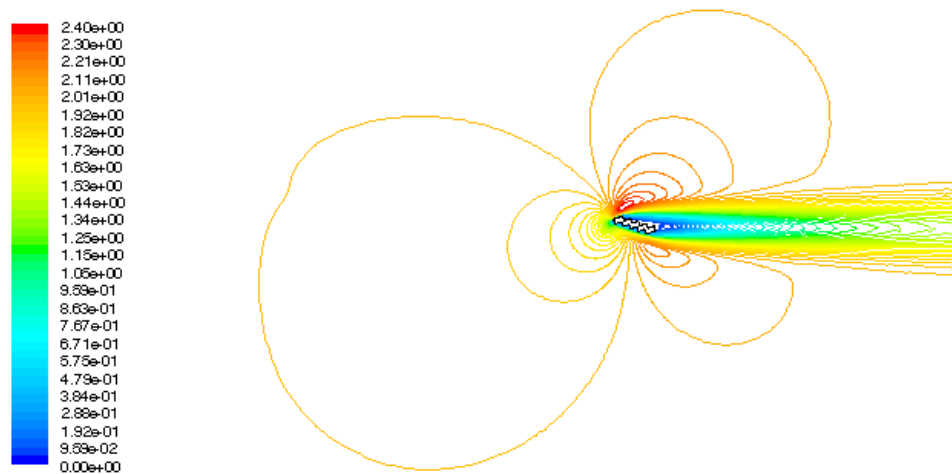


Figure 5-3 Velocity contour, angle of attack=15°

The maximum velocity is about 2.4 m/s at the top of the airfoil.

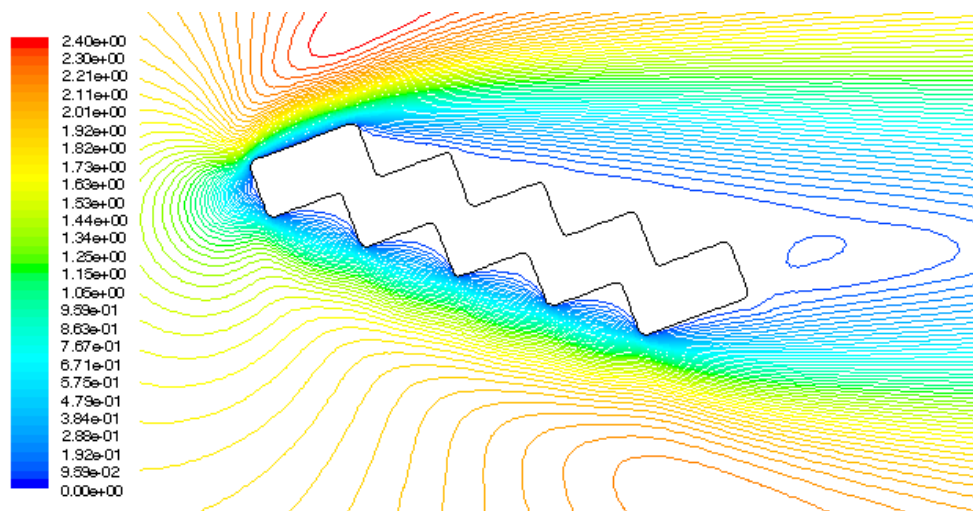


Figure 5-4 Velocity contour, a closer view, angle of attack=15°

As it is shown in Figure 5-4, according to the contours, in a relatively large region behind the airfoil, the air has very low velocity.

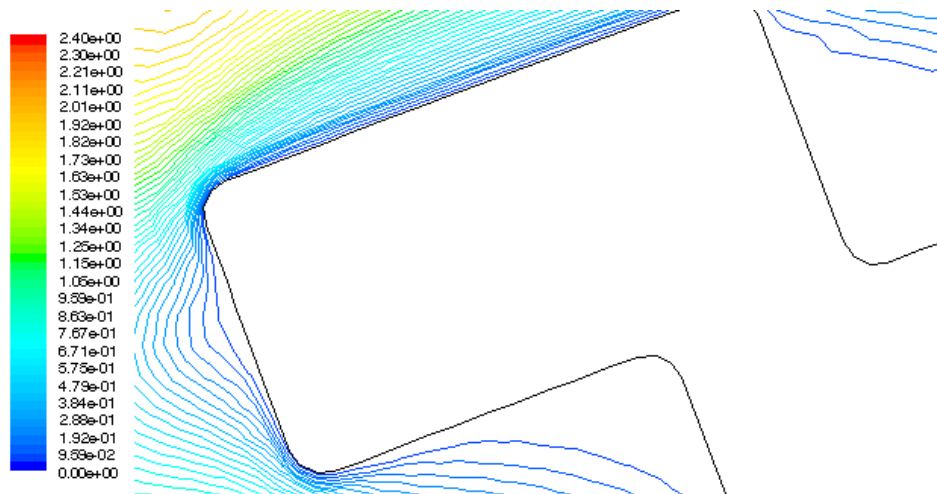


Figure 5-5 Velocity contour around leading edge, angle of attack=15°

The velocity gradient at the top of the airfoil is larger than the velocity gradient in the lower region.

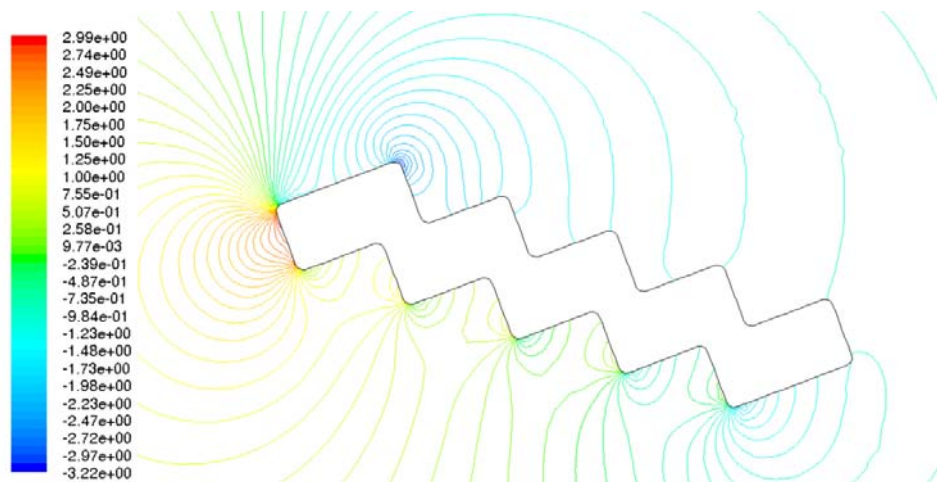


Figure 5-6 Pressure contour around the airfoil, angle of attack=15°

The forces and the coefficients are presented in Tables 5-1 and 5-2 for x-direction and y-direction components, respectively. In these tables, the pressure and viscous components represent the force due to pressure distribution and the resistance due to the force effects of

viscosity, respectively. The pressure gradient around the airfoil results in a force called “pressure force”. This force can be dissolved to two components. The component which is parallel to the flow is called “pressure drag”. The other component, which is perpendicular to the flow, is “pressure lift”.

**Table 5-1 Forces and coefficients parallel to the free stream velocity direction (Drag)**

force (N)			coefficient		
Pressure	Viscous	Total	Pressure	Viscous	Total
0.00070100724	0.00033751863	0.0010385259	0.40959197	0.19720898	0.60680095

The viscosity of the fluid results in a skin friction over the surface of the airfoil. This force is called “viscous force”. While the pressure force that acts normal to the surface of the airfoil, the viscous force is parallel to the surface. The net viscous force can be dissolved into two components: parallel and perpendicular to the flow. They are called viscous drag and lift respectively.

**Table 5-2 Forces and coefficients perpendicular the free stream velocity direction (Lift)**

force (N)			coefficient		
Pressure	Viscous	Total	Pressure	Viscous	Total
0.00095643504	3.1097802e-05	0.00098753284	0.55883604	0.018170154	0.5770062

The computed drag and lift coefficients are of the same order; hence, the lift/drag ratio is about one. The lift coefficient does not violate the assumption amount of this coefficient. However the drag coefficient is relatively large.

Making a comparison between the forces formed via pressure difference and the force due to friction or viscosity shows that the pressure plays a dominant role in drag and lift.

## 5.2 Aerodynamic Coefficients

In this section, all the aerodynamic coefficients for different angles of attack are presented.

Table 5-3 contains the lift coefficient,  $C_L$ , the drag coefficient,  $C_D$ , and the lift/drag ratio,

$\frac{C_L}{C_D}$ , for all angles of attack.

**Table 5-3 Lift and Drag Coefficients, Lift/Drag Ratio in different angles**

Angle of attack °	$C_L$	$C_D$	$\frac{C_L}{C_D}$
<b>5</b>	0.260577	0.535421	0.486677
<b>10</b>	0.451592	0.564379	0.800157
<b>15</b>	0.577006	0.606801	0.950899
<b>20</b>	0.648931	0.658122	0.986035
<b>25</b>	0.685994	0.715122	0.959268
<b>30</b>	0.698669	0.77621	0.900104
<b>35</b>	0.693669	0.838987	0.826794
<b>40</b>	0.670976	0.902192	0.743717

Figure 5-7 shows the obtained results for the lift coefficients for different angles of attack.

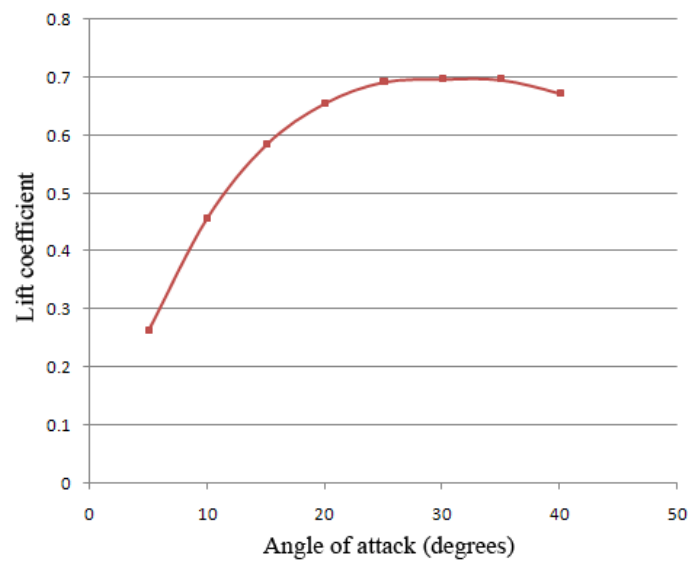


Figure 5-7 Lift coefficient vs. angle of attack

As it is illustrated in Figure 5-7 the total lift coefficient increases as the angle of attack increases up to  $30^\circ$ . For larger angles of attack, the lift coefficient is decreasing but not as sharp as in the cases with high Reynolds numbers.

The obtained results for the total drag coefficient are shown in Figure 5-8.

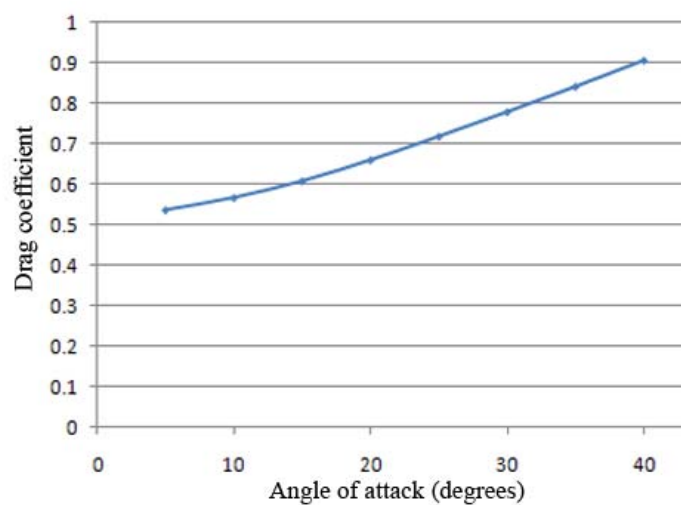


Figure 5-8 Drag coefficient vs. angle of attack

As the angle of attack increases, the drag coefficient also increases. This behaviour is similar to the behaviour of the drag coefficient for large airfoils with high Reynolds numbers.

The diagram of the lift/drag ratio versus the angle of attack is shown in Figure 5-9.

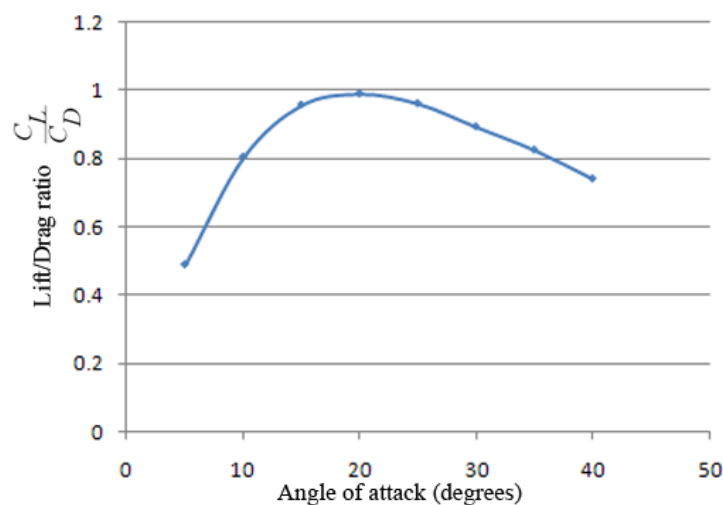


Figure 5-9 Lift/Drag Ratio vs. angle of attack

According to Figure 5-9, the Lift/Drag ratio is a maximum at an angle of attack of 20°. The maximum value for this ratio is about one. Generally, the value of the Lift/Drag ratio exceeds 10 for a shape that is considered an airfoil. However, as the drag coefficient is relatively large in the current project because of the shape of the cross-section and the Reynolds number for this fan is very low, the value of the Lift/Drag ratio obtain is much lower than 10.

The viscous and the pressure components of the drag and lift forces are drawn to determine the significance of each component. The pressure- and viscous-drag forces for different angles of attack are shown in Figures 5-10 and 5-11, respectively.

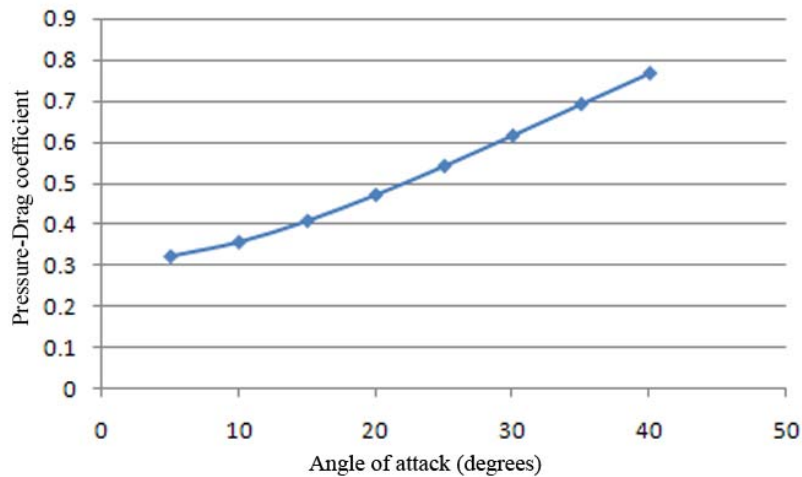


Figure 5-10 Pressure-Drag coefficient

As explained before, the pressure-drag is a drag force caused by pressure gradient. The angle of attack affects the pressure distribution around the airfoil. Therefore, pressure-drag is related to the angle of attack. According to Figure 5-10, the pressure-drag is larger for larger angles of attack.

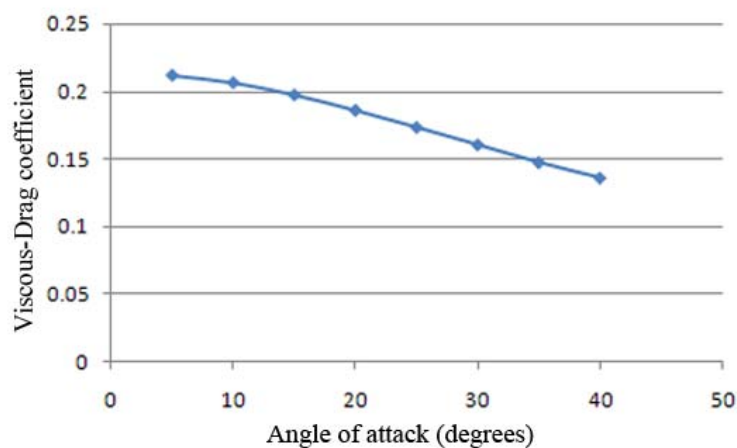


Figure 5-11 Viscous-Drag coefficient

Because the viscous force is tangential to the surface of the airfoil, the components are related to the angle of the chord line. When the angle of attack changes the viscous force and its drag and lift components changes. The viscous force is, basically, a friction force exerted by the fluid on the surface of the airfoil. Hence, the magnitude and the direction of this force are highly related to the shape of the airfoil. Moreover, the shape of the airfoil affects the thickness of the boundary layer. This factor can also affect the viscous force.

The coefficients (pressure- and viscous-lift) are shown in Figures 5-12 and 5-13.

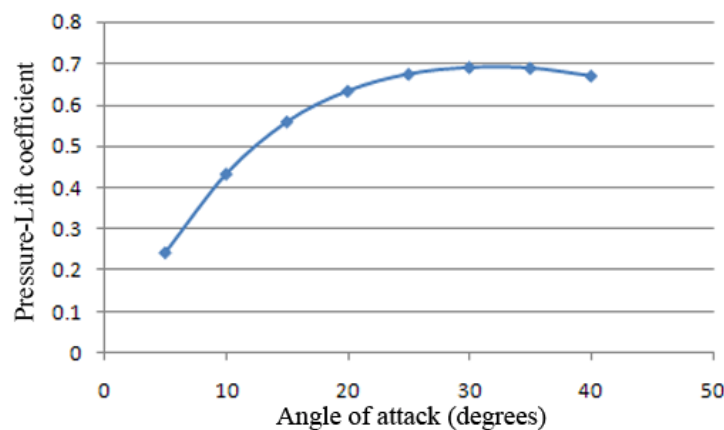


Figure 5-12 Pressure-Lift coefficient

The behaviour and amount of the pressure-lift is very similar to the behaviour and amount of the total lift.

The diagram for viscous-lift coefficient versus angle of attack is shown in Figure 5-13.



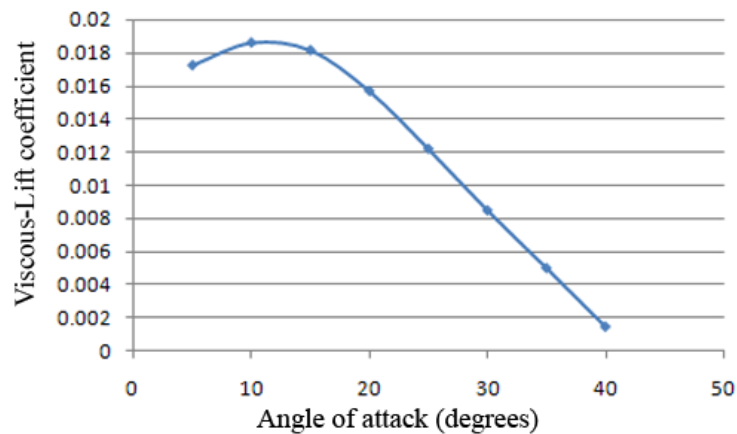


Figure 5-13 Viscous-Lift coefficient

As mentioned before the viscous force is related to the angle of attack and the shape of the airfoil. According to the Figure 5-13, the viscous lift increases for angles smaller than  $15^\circ$  and for larger angles, this value decreases. This behavior is because of the unusual layer-by-layer cross-section of the airfoil.

### 5.3 Discussions

The main result extracted from the contours and the diagrams, is that the best angle of attack for a given design, can be determined. The lift coefficient and the lift/drag ratio were used to determine the best angle; which is the value at which the highest lift/drag ratio occurs.

As mentioned in Chapter 2, the decrease of the total lift force and lift coefficient show that stall has occurred. There is a similar phenomenon at low velocities. However, comparing Figure 2-9 with Figure 5-7, for low Reynolds number the drop in the lift coefficient is not as sharp as that for high Reynolds numbers.

Although the lift coefficient is slightly bigger than the assumed value ( $C_L = 0.6$ ), it does not violate our design criteria. A smaller lift coefficient results in a longer chord. Due to its

critical role in transferring the energy to accelerate the air, the chord line should be longer for smaller fans.

It should be noted that according to the definition of airfoils, the lift/drag ratio should be greater than 10. This ratio cannot be obtained for layer-by-layer airfoil for very low Reynolds numbers. However, the word “airfoil” is used for ease of convenience.

The angle of attack of  $20^\circ$  is determined as the best angle for fan blade, because at this angle, the lift/drag ratio is a maximum ( $\frac{C_L}{C_D} \approx 0.99$ ). The lift coefficient for this angle is 0.65

$$(C_L|_{\alpha=20^\circ} \approx 0.65).$$

The drag coefficient behaves similarly for high and low Reynolds numbers. However, it is much larger for very low Reynolds numbers which is disadvantageous for small fans. According to Figures 5-10 to 5-13, the pressure distribution is critical in determining the total lift and drag forces. The pressure lift and drag coefficients, which are representative for the lift and drag forces due to the pressure gradient around the airfoil are significant compared to viscous lift and pressure coefficients. Hence, it is concluded that the pressure gradient around the airfoil plays more significant role in comparison to the effect of viscosity.

## 5.4 Modification of the Geometry

As mentioned in the beginning of this section, fabrication process limitations do not allow the making of any arbitrary airfoil shape. Therefore, the shape of the cross-section of the airfoil is different for different blade angles.

After the preceding simulation and discussion, the modified blade sections are modelled and the results are presented in this section. The modified geometries are those that will be fabricated using micro fabrication techniques. These cross sections are designed according to

the described algorithm in the Design section. The difference is that when the angle of attack changes, the airfoil is not rotated, but is designed for the new angle. Simulations are carried out for several angles:  $15^\circ$ ,  $20^\circ$ ,  $25^\circ$  and  $30^\circ$ . The results for angle of attack equal to  $15^\circ$  are illustrated below. The contours and tables for other angles of attack are presented in Appendix B.

#### 5.4.1 Results for Angle of attack= $15^\circ$

The geometry of the modified airfoil is shown in Figure 5-14. The blade angle is shown in the picture (the length unit is millimetre).

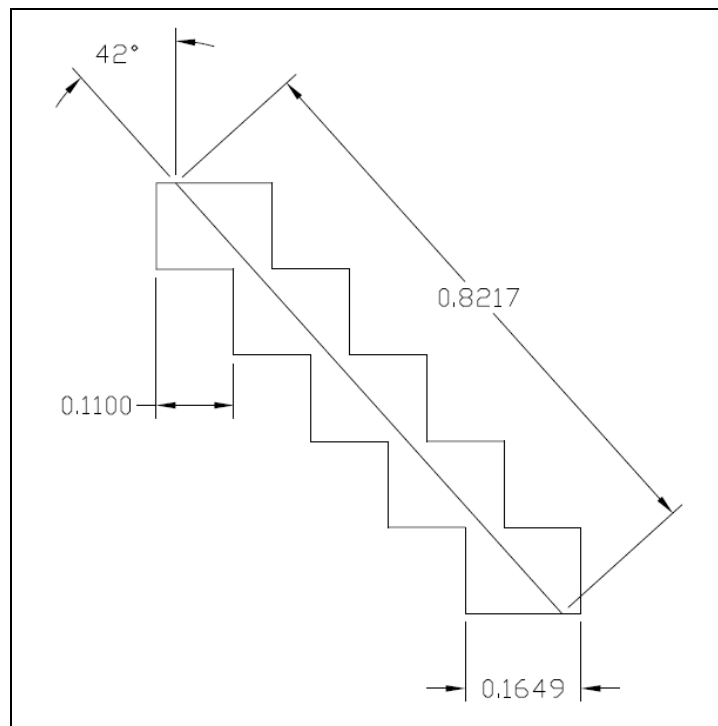


Figure 5-14 Modified geometry, angle of attack= $15^\circ$

The residuals, the velocity contours and the pressure contour around the airfoil are presented in Figures 5-15 to 5-19.

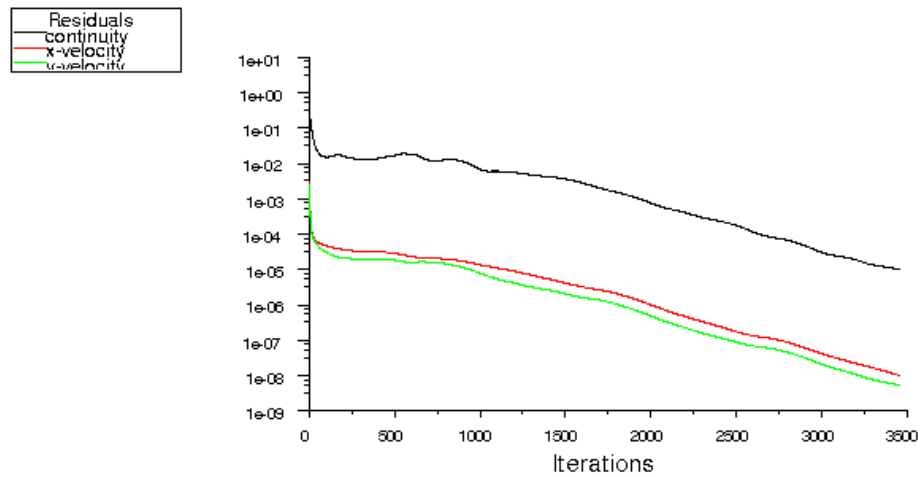


Figure 5-15 Residuals, angle of attack= $15^\circ$

The solution has converged after about 3500 iterations.

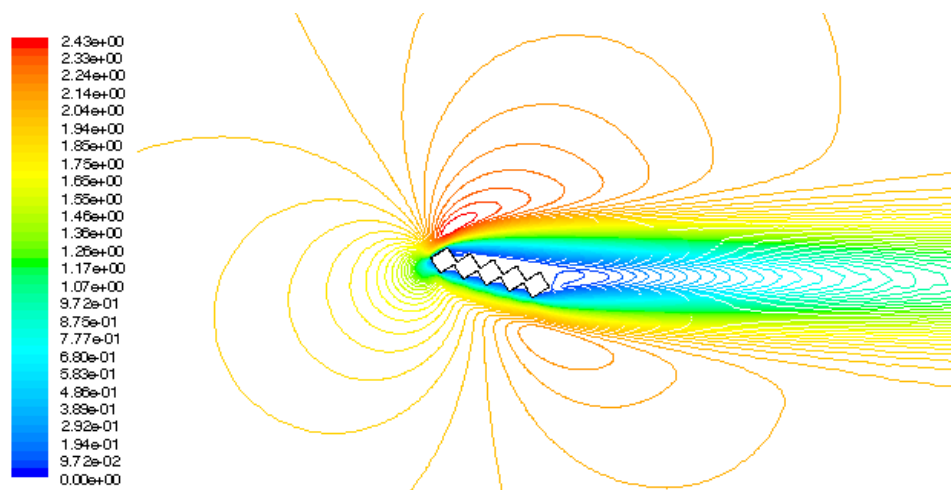


Figure 5-16 Velocity contour, angle of attack= $15^\circ$

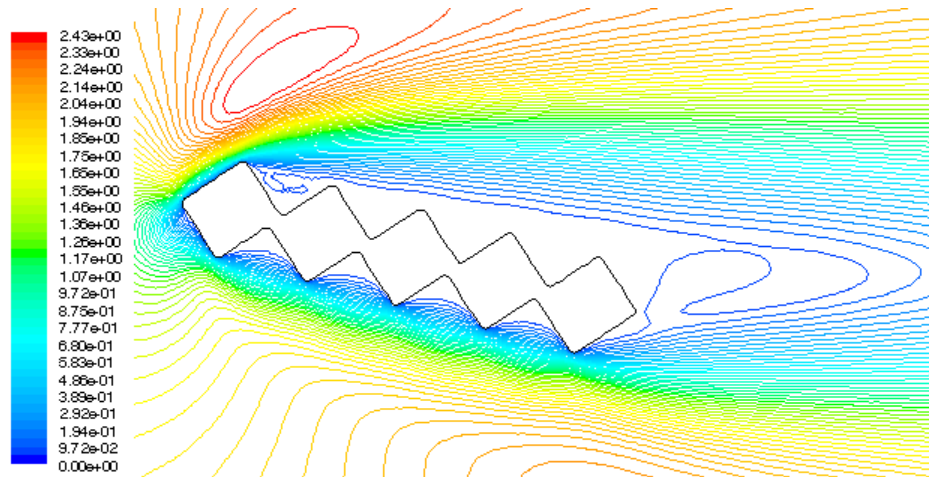


Figure 5-17 Velocity Contour, angle of attack=15°

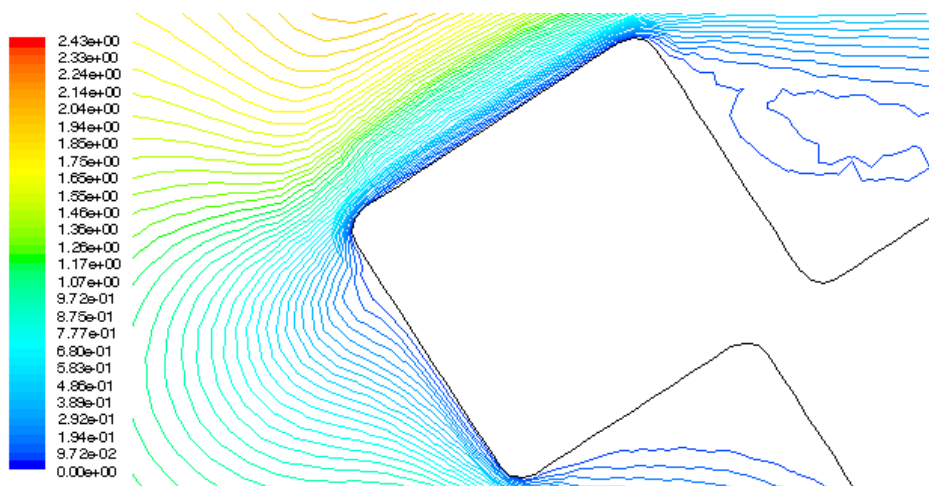


Figure 5-18 Velocity contour around the leading edge, angle of attack=15°

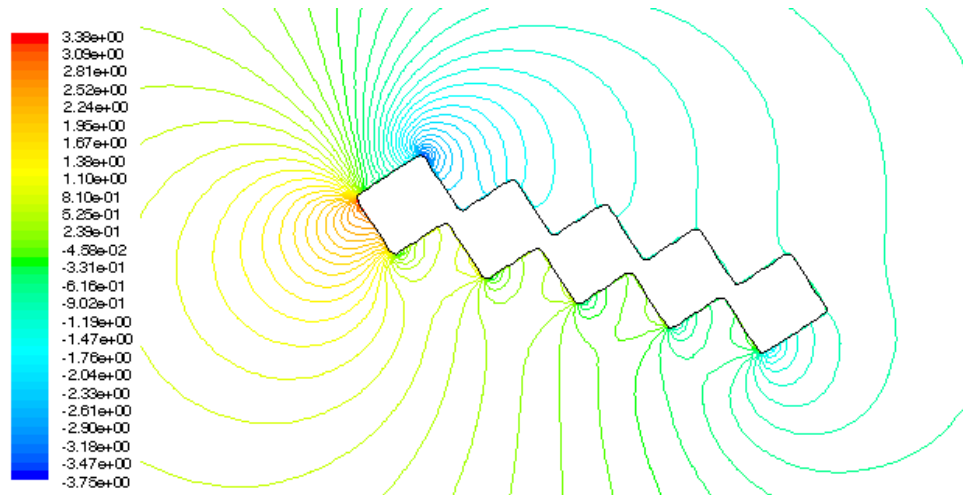


Figure 5-19 Pressure contour around the airfoil, angle of attack=15°

The obtained results for the forces and the coefficients are presented in Table 5-4 and Table 5-5. The first table is for x-direction component and the second table is for the perpendicular forces and the corresponding coefficients.

Table 5-4 Forces and coefficients parallel to the free stream velocity direction (Drag)

force (N)			coefficient		
Pressure	Viscous	Total	Pressure	Viscous	Total
0.00078934009	0.00031225691	0.001101597	0.40412181	0.1598675	0.56398931

Table 5-5 Forces and coefficients perpendicular to the free stream velocity direction (Lift)

force (N)			coefficient		
Pressure	Viscous	Total	Pressure	Viscous	Total
0.0011045441	2.3234403e-05	0.0011277786	0.56549818	0.011895416	0.5773936

$$\frac{C_L}{C_D} = 1.024$$

## 5.5 Flat-Plate Cross-Section

The results for simulation of flow around the corresponding flat plate cross-sections are presented here. This corresponding cross-section is generated separately for each layer-by-layer designed blade.

### 5.5.1 Geometry

The method of creating the geometry of the “flat plate” cross-section is illustrated in Figure 5-20 for the blade with the angle of attack of  $25^\circ$ .

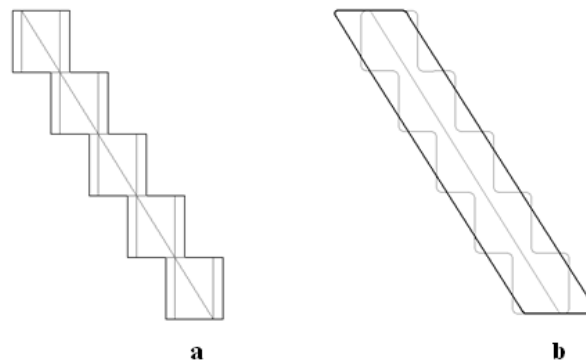


Figure 5-20 Layer-by-layer and flat-plate cross-sections

As illustrated in Figure 5-20-b, the thickness of the flat plate is considered to be the same as that of the corresponding designed airfoil. Because of fabrication limitations, the dimensions of each layer of modified cross-section for different angle of attack are different. Hence, flat plate cross-sections have different thicknesses. This investigation shows the effect of the steps on the air around the blades.

### 5.5.2 Numerical Simulation

The air flow around these geometries was simulated. The coordinates of the domain and the boundary conditions remained unchanged. A close view of this cross-section in the domain is shown in Figure 5-21.

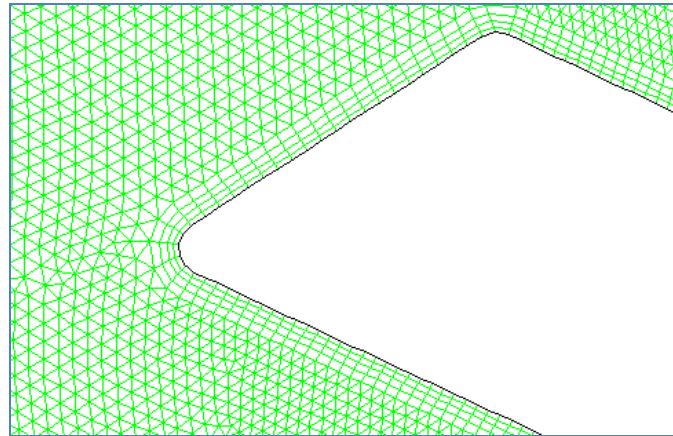












Figure 5-21 A close view of the flat-plate cross-section in the domain

There are 78812 cells in the coarser mesh and 175390 in the finer mesh for  $\alpha = 20^\circ$ . The simulations were conducted for these two sizes of meshes to show that the solution is mesh size independent. A boundary layer was generated around the flat plate airfoil as in the previous simulations. This boundary layer can be seen in Figure 5-21.

Table 5-6 provides a comparison between the shape of the different cross-sections.



**Table 5-6 Layer-by-layer and flat-plate cross-sections for different angles**

Angle of Attack	35°	30°	25°	20°	15°
layer-by-layer cross-section					
flat-plate cross-section					

The obtained results from these simulations are presented briefly in following chapters.

#### 5.5.2.1 Angle of attack = 15°

The velocity contour about the flat-plate airfoil is illustrated in Figure 5-22.

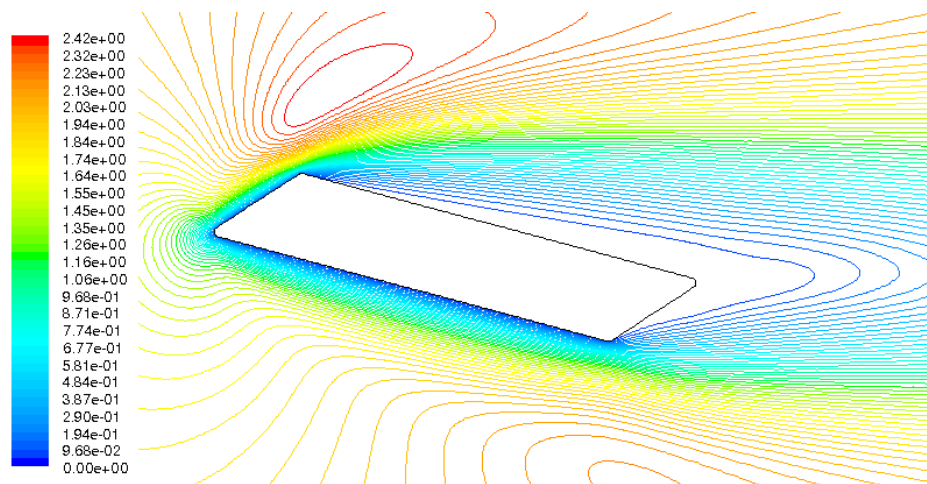


**Figure 5-22 Velocity contour, angle of attack=15°**

The obtained results for the forces and the coefficients are presented in Table 5-7 and Table 5-8. The first table is for x-direction component and the second table is for the perpendicular forces and the corresponding coefficients.

Table 5-7 Forces and coefficients parallel to the free stream velocity direction (Drag)

force (N)			coefficient		
Pressure	Viscous	Total	Pressure	Viscous	Total
0.00048652102	0.00062387823	0.0011103992	0.24908624	0.3194096	0.56849584

Table 5-8 Forces and coefficients perpendicular to the free stream velocity direction (Lift)

force (N)			coefficient		
Pressure	Viscous	Total	Pressure	Viscous	Total
0.0010387946	2.2144813e-05	0.0010609395	0.53183612	0.011337574	0.5431737

$$\frac{C_L}{C_D} = 0.955$$

## 5.6 Discussions

To compare the results for non-modified geometry, modified geometries and the obtained results for flat-plate cross-sections, these results are listed in Table 5-9.

Table 5-9 Results for modified and non-modified geometries

Angle of attack	$\alpha = 10^\circ$		$\alpha = 15^\circ$		$\alpha = 20^\circ$		$\alpha = 25^\circ$		$\alpha = 30^\circ$	
Coefficients	$C_L$	$\frac{C_L}{C_D}$	$C_L$	$\frac{C_L}{C_D}$	$C_L$	$\frac{C_L}{C_D}$	$C_L$	$\frac{C_L}{C_D}$	$C_L$	$\frac{C_L}{C_D}$
Non-modified	0.452	0.800	0.577	0.951	0.649	<b>0.986</b>	0.686	0.959	0.699	0.900
Modified	0.391	0.774	0.577	<b>1.024</b>	0.635	0.972	0.696	0.950	0.734	0.904
Flat-Plate	0.344	0.672	0.543	0.955	0.652	1.017	0.744	<b>1.029</b>	0.803	0.998

Table 5-9 shows that the results for the modified geometries are generally better. It also shows that the results for the flat-plate cross sections are almost the same, i.e. the steps do not

affect significantly the flow in this range of Reynolds number and the results are comparable to those corresponding to the layer-by-layer cross-section. The assumed lift coefficient in the design process was 0.6 in  $\alpha = 6^\circ$  for the flat plate. This value is slightly different from the computed lift coefficient. Nevertheless, this difference does not violate the design procedure as explained previously. It should be noted that the best angle of attack is very different for high and low Reynolds. For very low Reynolds numbers ( $Re < 100$ ), this angle is larger. If this angle is determined based on the lift coefficient and the lift/drag ratio, as in this project, it will be approximately  $20^\circ$  for the non-modified geometry and  $15^\circ$  for the modified geometries.

A region having very low velocity takes place downstream of the blade. It results in a comparatively high drag coefficient. Decreasing of the drag coefficient and, consequently, a rise in the lift/drag ratio is expected if this region becomes smaller. In other words, if the boundary layer thickness behind the airfoil decreases, the performance of the fan will improve. In this region, the fluid flows backward. The amount of the back flow is very small compared to the free stream velocity. Corona discharge can be exploited to make this area smaller. For this purpose, required electrical potential should be applied to the appropriate areas on the blade surface. According to Figure 2-7, the separation area can be controlled using this technique.

Another approach to prevent flow separation is modifying the shape of the airfoil. This modification can be achieved by making different-thickness layers.

The analyzed airfoils have different chord lengths. Fabrication limitations cause different chord lengths for different airfoils at different angles of attack. Lithography is a planar fabrication method, i.e. a 3-D product produced using this method has a layer-by-layer

structure. Because several fans will be fabricated simultaneously on a single wafer, they will possess the same layer thicknesses. Different blade angles and the same layers thicknesses will result in different chord lengths.

In this chapter, the CFD results of the 2-D airfoil at different angles of attack are presented and discussed. Modifications to the geometry are made according to selected fabrication technique (lithography) and the aerodynamics coefficients are recomputed for some angles. It is observed that most of the lift coefficients and the lift/drag ratios for the modified geometries are slightly higher which results in a better performance and the difference between the coefficients of the modified layer-by-layer cross-section and the corresponding coefficients of the flat-plate cross-section is not significant.

## 6 Fan Testing and Experiment

### 6.1 Introduction

In this chapter, the results from fan testing are presented. A test rig was designed and fabricated to test the fans. A DC electro motor was employed as the actuator. The air flow was calculated based on the static pressure and total pressure measured using a Pitot - Static tube and a pressure transducer. The pressure transducer was calibrated using an inclined manometer and a wind tunnel. Figure 6-1 shows the whole calibration set-up.

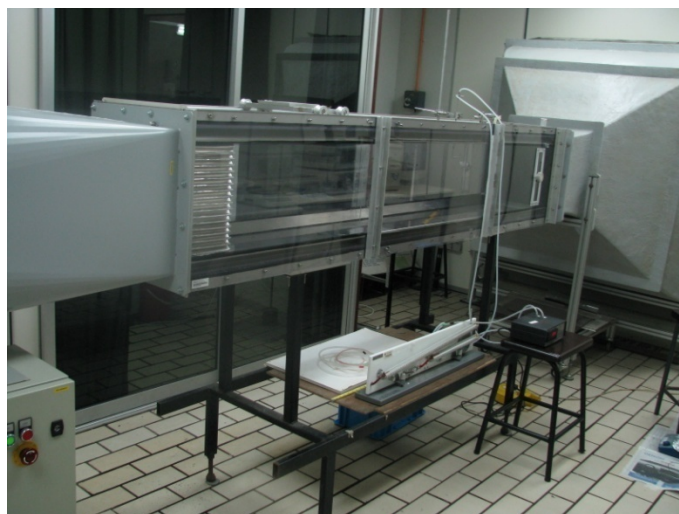


Figure 6-1 Calibration set-up

## 6.2 Calibration

An inclined manometer was utilized as the reference to calibrate the pressure transducer which shows the pressure difference in Pascal. The manometer can be seen in Figure 6-2.



Figure 6-2 Inclined manometer

A Pitot – Static tube which was installed in a wind tunnel was linked to the inclined manometer and the pressure transducer. The fan speed, and consequently, the air flow rate were controlled. The difference between the static and total pressure was measured to calibrate the transducer. Figures 6-3 to 6-5 show the Pitot – Static tube, the pressure transducer and the control panel of the wind tunnel respectively.



Figure 6-3 Pitot-Static Tube Installed Inside the Wind Tunnel

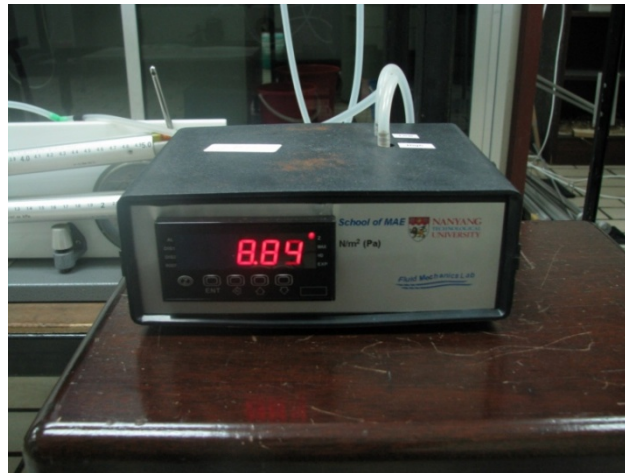


Figure 6-4 Pressure Transducer



Figure 6-5 Control Panel of the Wind Tunnel

### 6.3 Test Rig

A test rig was designed and built to test the fan pressure generated. Figure 6-6 shows the test rig.



Figure 6-6 Test Rig

The actuator of the fan is a DC electro motor. The motor was coupled to the fan using a coupling that was fabricated using CNC (Computer Numerical Control) machine. A small Pitot –Static tube was utilized to measure the static and total pressure difference to calculate



the air flow rate. The calibrated pressure transducer was used to measure the pressure difference.

## 6.4 Torque Calculation

An estimation of the exerted torque to the motor from the fan is needed for motor selection. The torque was calculated according to [20]. The procedure of the calculation is presented below.

$$T = T_c \times \frac{1}{2} \rho \bar{V}_a^2 \pi R^3 \quad (6.1)$$

where  $T$  is total torque applied on the motor shaft,  $\rho$  is the air density,  $\bar{V}_a$  is the mean axial velocity,  $R$  is the radius of the fan and  $T_c$  is calculated from equation (6.2).

$$T_c = \int_{x_b}^1 \frac{2(V_{a1} + V_{a2})(V_{\theta_s} + V_{\theta_p})x^2}{\bar{V}_a^2} dx \quad (6.2)$$

where  $V_a$  and  $V_\theta$  is axial and swirl velocity component. According to the assumptions explained in the chapter of Chapter (3.2) and equation (2.13):

$$\varepsilon_p = 0 \Rightarrow V_{\theta_p} = 0 \quad (6.3)$$

$$V_{a1} = V_{a2} = \bar{V}_a \quad (6.4)$$

And according to the definition we have:

$$V_{\theta_s} = \varepsilon_s \bar{V}_a = 0.19782 \approx 0.2 m/s \quad (6.5)$$

And  $x$  is:

$$x = \frac{r}{R} \quad (6.6)$$

Hence,

$$x_b = \frac{r_h}{R} = 0.3 \quad (6.7)$$

Then the integral in the equation (6.2) turns to

$$T_c = \frac{4\bar{V}_a V_{\theta_s}}{\bar{V}_a^2} \int_{x_b}^1 x^2 dx = (0.324) \frac{4\bar{V}_a V_{\theta_s}}{\bar{V}_a^2} \quad (6.8)$$

After substitution we have,

$$T_c = 1.296 \quad (6.9)$$

Now we can calculate  $T$  from equation (6.1). After substituting all the parameters, we have,

$$T = 3.81 \times 10^{-8} N.m \quad (6.10)$$

The value for the total torque is small enough to be considered negligible. It is concluded that the torque does not possess a significant importance for choosing the motor. In other words, because the torque is related to the size of the fan, the fan is small enough to make it feasible to assume that the motor works with no load.

## 6.5 Results and Discussion

Because of the extra small size of the fans, there are many limitations in measurements. As mentioned earlier, a Pitot-Static tube was employed to measure the difference between the total pressure and static pressure. This difference is used for air flow rate calculation. The pressure generated by the fan is measured to compare the products with the assumption made according to the Cordier diagram. Three different fans with different blade angles were tested. Each fan was rotated at three rotational speeds: 19150 rpm, 13660 rpm and 10250 rpm. These speeds were adjusted by changing the voltage of the motor and were measured using a tachometer.

The values of static pressure generated by different fans are listed in Table 6-1. The air flow rate is calculated using equation (6.11).

$$Q = AV \quad (6.11)$$

where  $A$  is the area and  $V$  is the mean axial velocity.  $A$  is the same as what is written in Table 3-2.  $V$  is calculated according the pressure difference measured by Pitot-Static tube using (6.12).

$$V = \sqrt{\frac{2\Delta P}{\rho}} \quad (6.12)$$

where  $\Delta P$  is the pressure difference measured by the Pitot-Static tube and  $\rho$  is the air density.

**Table 6-1 Measured Pressures and Flow Rates**

Angle of Attack	Speed (rpm)	Pressure Generated (Pa)	Pitot-Static Tube (Pa)	Flow Rate (Q/m <sup>3</sup> )
15°	19150	0.51	0.17	9.51E-06
	13660	0.25	0.08	5.16E-06
	10250	0.13	0.05	4.61E-06
20°	19150	0.47	0.15	8.93E-06
	13660	0.27	0.06	5.65E-06
	10250	0.16	0.05	5.16E-06
25°	19150	0.29	0.20	1.03E-05
	13660	0.14	0.08	6.52E-06
	10250	0.08	0.04	4.61E-06

The assumption for the rotational speed in the design procedure is 10000 rpm. The speeds in Table 6-1 have been adjusted by changing the voltage. Therefore, the smallest values for the speeds are slightly different. The test was repeated for two other speeds.

The pressure generated by the fans at about 10000 rpm are less than what is assumed in design procedure. This is reasonable because the pressure difference for the design was assumed according to the Cordier diagram. As mentioned earlier, the Cordier diagram is valid for conventional size turbomachines. One of the critical requirements for an efficient turbomachines is an efficient blade cross-section shape or airfoil. The blades of tested fans are not efficient because of numerous fabrication limitations. However, the values for pressure generated seem acceptable.

According to the results, for the lowest rotational speed, the fan with angle of attack of  $20^\circ$  generated the highest static pressure. This fan generates the highest static pressure at the rotational speed of 13660 rpm. Nevertheless, at rotational speed of 19150 rpm, the highest static pressure is generated by the fan with angle of attack of  $15^\circ$ .

The measured flow rate is smaller than what is mentioned in Table 3-1. It is reasonable for the actual flow rate to be smaller than the ideal one, because the design flow rate was derived from the Cordier diagram. The fans with angle of attack of  $25^\circ$ , can generate a larger flow rate. On the other hand, they cannot generate pressures as large as the other tested fans with other angles of attack. The extra small size of the test rig and tested products caused many limitations in selection of measurement devices and their accuracy. Hence, it is recommended to employ more accurate devices if more accurate result is required.

The results show that the numerical simulation and the Lift/Drag criteria are helpful to obtain an acceptable estimation for the best angle of attack. Although 2-D numerical analyses do not

predict the best angle of attack exactly, they help the manufacturer to select an acceptable angle of attack.

## 7 Conclusions and Recommendations

### 7.1 Conclusions

A thorough literature review was conducted. There are many different technologies that can be employed in cooling devices. To have an efficient heat removal device, various technologies should be combined. A small air accelerator is a component that can make cooling devices more efficient. A micro axial fan can be a complementary part in efficient micro cooling system. Nevertheless, they can also be used in other applications.

In the next stage, an axial fan was designed using a conventional axial fan design method. The Cordier diagram was used to estimate the flow rate and pressure generated. The dimensions and rotary velocity are assumed as given quantities. The designed fan is 5 mm in diameter with the rotary velocity of 10000 rpm. Because of the fan size, the profile at the mid-radius will be designed. After completing the design, a procedure was suggested to develop a five-layer airfoil according to fabrication limitations. The preliminary design was then modified using the results obtained from CFD analysis of designed airfoils. The five-layer airfoils were simulated during the numerical modelling.

2-D simulations were carried out to determine the optimal angle of attack. Maximum value for lift/drag ratio was selected as the criterion for determining this angle. The trend of the lift and drag coefficients are similar for very low and high Reynolds numbers. However, when stall occurs, the lift coefficient drop is not as sharp as the drop at high Reynolds number. The obtained lift coefficients are very similar to the lift coefficient of the flat plate in high Reynolds number (Figure 2-9). The maximum lift coefficients for flat plate at high Reynolds number is about 0.8 and for the five-layer airfoil in this project is about 0.7. The lift coefficient at the angle where the maximum lift/drag ratio occurs is about 0.6. At very low Reynolds numbers, the maximum lift coefficient occurred at a comparatively larger angle of attack (Figure 5-7) as compared to high Reynolds number flows.

On the other hand, the drag coefficients are much larger for very low Reynolds numbers when compared to high Reynolds number flows. Larger drag coefficients results in a comparatively smaller lift/drag ratio. This fact should be considered that, although the lift/drag ratio for an airfoil should be more than 10, the obtained results show that this ratio is about 1 for designed airfoils. Both the unusual shape of the airfoils and the very low Reynolds number cause this ratio to be small.

The pressure forces (formed by pressure distribution) and viscous forces (formed because of the effect of viscosity) are compared together. The pressure forces are much larger than viscous forces. Hence, the effect of pressure is more important than the effect of viscosity.

After the first series of simulations, the design was modified considering the fabrication process. This modification results in different airfoils for different angles of attack. These airfoils, because of the fabrication limitations, have different chords lengths. However, the layers thicknesses are the same. Hence, many fans, with different angles of attack, can be fabricated simultaneously.

Fabrication of the fans and testing their performances are the critical conquests of the future work. Evaluation of the design method and its assumptions for very low Reynolds numbers is another objective for future work.

Fabrication of five-layer SU-8 structure was a challenging part of the project. Detaching the solidified SU-8 from the substrate was also an important task during the fabrication process.

The (static) pressure is a maximum near to the leading edge (stagnation point). The maximum value is about three times the free stream static pressure. Therefore this layer should not be too thin.

Although the main goal of simulations was to determine the optimal angle of attack for very low Reynolds number, a few different blades (with different angles) have been fabricated and tested. The fans with angles of attack of  $15^\circ$ ,  $20^\circ$  and  $25^\circ$  are fabricated and tested.

The shapes of the fans are compared. SEM images show that the quality is enhanced when the exposure time for the layers not at the bottom was reduced. Exposure times were changed for different wafers. It is concluded that the exposure time should be less than what is given in the manufacturer's catalogues for the layers which are not supposed to touch the silicon substrate. This is because the exposure time that is provided by the manufacturer is for a single layer product.

As mentioned before, one of the most important properties of photolithography is the ability of high speed manufacturing of relatively small products. Using photolithography allows us to fabricate many parts (of the same thicknesses) simultaneously. In this project, the substrate is a 10cm diameter wafer and the outer diameter of each fan is 5mm. The products should be 2-3 mm apart from each other. The latter is due to the fact that each fan should be prevented from being attached together.



The fabricated fans were tested and the results were compared to 2-D numerical analyses at the same angle of attack. It is concluded that the 2-D simulations and the lift/drag ratio criteria can give us an acceptable estimation of the best angle of attack, although the best angle of attack cannot be predicted exactly, based on 2-D simulation. 3-D simulations can be conducted if more accurate prediction is required. The best angle of attack based on static pressure generation is  $20^\circ$  at a speed of 13660 rpm. However, the fan with an angle of attack of  $15^\circ$  provides better performance at higher rotational speeds. The flow rates generated by the fans with the angles of attack of  $15^\circ$  and  $20^\circ$  are almost the same. Fans with an angle of attack of  $15^\circ$  generate larger flow rates, except for the lowest rotational speed. The largest flow rate is generated by the fan with an angle of attack of  $25^\circ$ . However, the pressure generated is lower than the other tested samples.

## 7.2 Recommendations

This project can be divided to four different stages: design, numerical analysis, fabrication and testing. A few recommendations, about each above-mentioned stage are presented in the current chapter for future researches in this field.

The adopted design method is a conventional technique. An improvement in the design method for the very small-sized axial fans is required. Experimental diagrams for the lift coefficient against angle of attack for very low Reynolds numbers ( $<100$ ) are required. Because of the fabrication limitations, making any arbitrary airfoil is not possible. Hence, an investigation to determine appropriate airfoil shapes for extra small rotary fans which are possible to be fabricated can be conducted.

In spite of the recent significant improvement in micro fabrication technique, there are still many limitations to fabricate 3-D structures. Other fabrication methods can be employed for making small axial fans. Some methods which were introduced in the chapter of Literature Review possess capabilities to be suitable for fan blade fabrication. MEMSNAS method is a recommended method for the future researches in this area.

Small size and, consequently, very low Reynolds number results in relatively large region behind the blade that the air velocity is almost zero. Corona discharge that is illustrated in Figure 2-7 can be used to solve the problem. In order to use corona discharge, an electrically conductor layer should be sputtered on the appropriate position of the blade.

Fabrication improvements can be made to enhance the quality of the fan produced.. An investigation to determine the optimum exposure time for multi layer product with various thicknesses can be very helpful.

Three-dimensional simulations can be carried out to compare the computed pressure and airflow the actual pressure generated and air flow rate. 3-D simulations results more accurate results. On the other hand, they cause higher computational costs.

And finally, improvement of measurement devices is necessary. Because of the extra small size of the fans, the test rig would be very small compared to conventional test rigs. Hence, there are lots of limitations in measurements. The most important limitation is flow rate measurement. A small Pitot-Static tube was fabricated for this project. More accurate devices for very low Reynolds numbers can be developed to obtain more reliable results from experiments in the future. Moreover, the efficiency of these fans in heat removal can also be investigated to determine the effectiveness of the products for the main purpose that they are designed for.

This field is very promising and any development that can be used to achieve an optimum extra-small axial-fan design and fabrication method will be higher desirable.

## 8 References

1. Linderman, R.J., P.E. Kladitis, and V.M. Bright, *Development of the micro rotary fan*. Sensors & Actuators: A. Physical, 2002. **95**(2-3): p. 135-142.
2. Epstein, A.H., *MILLIMETER-SCALE, MEMS GAS TURBINE ENGINES*. Proceedings of ASME Turbo Expo 2003 Power for Land, Sea, and Air, 2003.
3. Grimes, R., et al., *Effect of Geometric Scaling on Aerodynamic Performance*. AIAA Journal, 2005. **43**(11): p. 2293-2298.
4. Tsai, B.J. and C.L. Wu, *Investigation of a miniature centrifugal fan*. Applied Thermal Engineering, 2007. **27**: p. 229-239.
5. Frechette, L.G., et al. *Demonstration of a Microfabricated High-Speed Turbine Supported on Gas Bearings*. in *Hilton Head Solid-State Sensor & Actuator Workshop*. 2000. Hilton Head Island.
6. Yoo, J.H., J.I. Hong, and W. Cao, *Piezoelectric ceramic bimorph coupled to thin metal plate as cooling fan for electronic devices*. Sensors & Actuators: A. Physical, 2000. **79**(1): p. 8-12.
7. Tan, F.L. and C.P. Tso, *Cooling of mobile electronic devices using phase change materials*. Applied Thermal Engineering, 2004. **24**(2-3): p. 159-169.
8. Jewell-Larsen, N.E., et al. *Coupled-Physics Modeling of Electrostatic Fluid Accelerators for Forced Convection Cooling*. 2006.
9. Yang, F., et al. *Corona Driven Air Propulsion for Cooling of Electronics*. 2003.
10. Hsu, C.P., et al., *Miniaturization of Electrostatic Fluid Accelerators*. Microelectromechanical Systems, Journal of, 2007. **16**(4): p. 809-815.
11. Jewell-Larsen, N.E., et al. *Numerical simulation and optimization of electrostatic air pumps*. 2004.

12. Hsu, C.P., et al. *Heat Transfer Enhancement Measurement for Microfabricated Electrostatic Fluid Accelerators*. 2008.
13. Truckenbrodt, E., *An Approximate Method for the Calculation of the Laminar and Turbulent Boundary Layer by Simple Quadrature for Two- Dimensional and Axially Symmetric Flow*. Journal of Aeronautical Science, 1952. **19**: p. 428-429.
14. Denton, J.D., *Loss Mechanisms in Turbomachines*. Journal of Turbomachinery, 1993. **115**(4): p. 621–656.
15. Jacobson, S.A. *Aerothermal challenges in the design of a microfabricated gas turbine engine*. 1998.
16. Mehra, A., *Computational Investigation and Design of Low Reynolds Number Micro-Turbomachinery*, in *Department of Aeronautics and Astronautics*. 1997, Massachusetts Institute of Technology.
17. Mehra, A., et al. *Aerodynamic Design Considerations for the Turbomachinery of a Micro Gas Turbine Engine*. 1998.
18. Léger, L., et al., *Influence of a DC corona discharge on the airflow along an inclined flat plate*. Journal of Electrostatics, 2001. **51**: p. 300-306.
19. Epstein, A.H. and S.D. Senturia, *Microengineering: Macro Power from Micro Machinery*. Science, 1997. **276**(5316): p. 1211.
20. Wallis, R., *Axial Flow Fans and Ducts*. 1983: Wiley-Interscience.
21. Eppler, R., *Airfoil Design and Data*. 1990: Springer Verlag.
22. Eppler, R. and D.M. Somers, *Supplement To: A Computer Program for the Design and Analysis of Low-Speed Airfoils*. NASA TM-81862, 1980.
23. Eppler, R. and D.M. Somers, *A Computer Program for the Design and Analysis of Low-Speed Airfoils*. NASA TM-80210, 1980.
24. Wallis, R.A., *Wind Tunnel Tests on a Series of Circular ARC Plate Aerofoils*. ARL Aero Note 74, 1946.
25. Cordier, O., *Similarity Considerations in Turbomachines*. VDI Reports, 1955. **3**.
26. Wright, T., *Fluid Machinery: Performance, Analysis, and Design*. 1999: CRC Press.
27. Ikuta, K. and K. Hirowatari. *Real three dimensional micro fabrication using stereo lithography and metal molding*. 1993.
28. Ikuta, K., S. Maruo, and S. Kojima. *New micro stereo lithography for freely movable 3D microstructure-super IH process with submicron resolution*. 1998.
29. Maruo, S. and K. Ikuta, *Three-dimensional microfabrication by use of single-photon-absorbed polymerization*. Applied Physics Letters, 2000. **76**: p. 2656.

30. Bertsch, A., H. Lorenz, and P. Renaud. *Combining microstereolithography and thick resist UV lithography for 3D microfabrication*. 1998.
31. Bertsch, A., H. Lorenz, and P. Renaud, *3D microfabrication by combining microstereolithography and thick resist UV lithography*. Sensors & Actuators: A. Physical, 1999. **73**(1-2): p. 14-23.
32. Bourouina, T., T. Masuzawa, and H. Fujita, *The MEMSNAS process: microloading effect for micromachining 3-D structures of nearly all shapes*. Microelectromechanical Systems, Journal of, 2004. **13**(2): p. 190-199.
33. Tabata, O., et al. *3D fabrication by moving mask deep X-ray lithography (M<sup>2</sup> DXL) with multiple stages*. 2002.
34. Beuret, C., et al. *Microfabrication of 3D multidirectional inclined structures by UV lithography and electroplating*. 1994.
35. Han, M., et al., *3D microfabrication with inclined/rotated UV lithography*. Sensors & Actuators: A. Physical, 2004. **111**(1): p. 14-20.
36. Da Yang, S.J.J. and C.K. Ober, *Three-Dimensional Microfabrication by Two-Photon Lithography*. MRS BULLETIN, 2005. **30**: p. 977.
37. Witzgall, G., et al., *Single-shot two-photon exposure of commercial photoresist for the production of three-dimensional structures*. Optics Letters, 1998. **23**(22): p. 1745-1747.
38. Yin, X., et al., *Near-field two-photon nanolithography using an apertureless optical probe*. Applied Physics Letters, 2002. **81**: p. 3663.
39. Simcic, J., et al., *3D micromachining of SU-8 polymer with proton microbeam*. Nuclear Inst. and Methods in Physics Research, B, 2005. **241**(1-4): p. 479-485.
40. Koller, D.M., et al., *Three-dimensional SU-8 sub-micrometer structuring by electron beam lithography*. Microelectronic Engineering, 2008. **85**(7): p. 1639-1641.
41. Kim, J., D.C. Joy, and S.Y. Lee, *Controlling resist thickness and etch depth for fabrication of 3D structures in electron-beam grayscale lithography*. Microelectronic Engineering, 2007. **84**(12): p. 2859-2864.
42. Irwin, R., et al. *Quick prototyping of flip chip assembly with MEMS*. 1998.
43. Harsh, K.F., V.M. Bright, and Y.C. Lee, *Solder self-assembly for three-dimensional microelectromechanical systems*. Sensors & Actuators: A. Physical, 1999. **77**(3): p. 237-244.
44. Harsh, K.F., R.S. Irwin, and Y.C. Lee, *Solder self-assembly for MEMS*, in *Proc. 1998 Int. Instrumentation Symposium (ISA)*. 1998. p. 256-261.
45. Kladitis, P.E., R.J. Linderman, and V.M. Bright, *Solder self-assembled micro axial flow fan driven by a scratchdrive actuator rotary motor*, in *Micro Electro Mechanical*

- Systems, 2001. *MEMS 2001. The 14th IEEE International Conference on*. 2001. p. 598-601.
46. Lee, K.Y., N. La Bianca, and S. Rishten, A. *Micromaching application of a high resolution with thick photoresist [J]*. J Vac Sci Technol, 1995. **13**(6): p. 3012-3016.
  47. Ho, C.H., et al., *Ultrathick SU-8 mold formation and removal, and its application to the fabrication of LIGA-like micromotors with embedded roots*. Sensors & Actuators: A. Physical, 2002. **102**(1-2): p. 130-138.
  48. Jeong, K.H., J. Kim, and L.P. Lee, *Biologically Inspired Artificial Compound Eyes*. 2006, American Association for the Advancement of Science. p. 557-561.
  49. Chuang, Y.J., F.G. Tseng, and W.K. Lin, *Reduction of diffraction effect of UV exposure on SU-8 negative thick photoresist by air gap elimination*. Microsystem Technologies, 2002. **8**(4): p. 308-313.
  50. Becker, E.W., et al., *Fabrication of microstructures with extreme structural heights by synchrotron radiation lithography, galvanofarming and plastic forming (LIGA process)*. Microelectron. Eng, 1986. **4**: p. 35-56.
  51. Bogdanov, A.L. and S.S. Peredkov, *Use of SU-8 photoresist for very high aspect ratio x-ray lithography*. Microelectronic Engineering, 2000. **53**(1-4): p. 493-496.
  52. Cremers, C., et al., *SU-8 as resist material for deep X-ray lithography*. Microsystem Technologies, 2001. **7**(1): p. 11-16.
  53. del Campo, A. and C. Greiner, *SU-8: a photoresist for high-aspect-ratio and 3D submicron lithography*. JOURNAL OF MICROMECHANICS AND MICROENGINEERING, 2007. **17**(6): p. 81.
  54. Liu, J., et al., *Process research of high aspect ratio microstructure using SU-8 resist*. Microsystem Technologies, 2004. **10**(4): p. 265-268.
  55. Lorenz, H., et al., *High-aspect-ratio, ultrathick, negative-tone near-UV photoresist and its applications for MEMS*. Sensors & Actuators: A. Physical, 1998. **64**(1): p. 33-39.
  56. Lorenz, H., et al., *SU-8: a low-cost negative resist for MEMS*. JOURNAL OF MICROMECHANICS AND MICROENGINEERING, 1997. **7**: p. 121-124.
  57. Lorenz, H., et al., *Fabrication of photoplastic high-aspect ratio microparts and micromolds using SU-8 UV resist*. Microsystem Technologies, 1998. **4**(3): p. 143-146.
  58. Lorenz, H., M. Laudon, and P. Renaud, *Mechanical characterization of a new high-aspect-ratio near UV-photoresist*. Microelectronic Engineering, 1998. **41**(42): p. 371-374.
  59. Yang, R. and W. Wang, *A numerical and experimental study on gap compensation and wavelength selection in UV-lithography of ultra-high aspect ratio SU-8 microstructures*. Sensors & Actuators: B. Chemical, 2005. **110**(2): p. 279-288.



60. Mata, A., A.J. Fleischman, and S. Roy, *Fabrication of multi-layer SU-8 microstructures*. JOURNAL OF MICROMECHANICS AND MICROENGINEERING, 2006. **16**(2): p. 276.
61. Peterman, M.C., et al., *Building thick photoresist structures from the bottom up*. JOURNAL OF MICROMECHANICS AND MICROENGINEERING, 2003. **13**(3): p. 380-382.
62. Tien, J., C.M. Nelson, and C.S. Chen, *Fabrication of aligned microstructures with a single elastomeric stamp*. Proceedings of the National Academy of Sciences, 2002. **99**(4): p. 1758.
63. Sum, T.C., et al., *Proton beam writing of low-loss polymer optical waveguides*. Applied Physics Letters, 2003. **83**: p. 1707.
64. Nordström, M., et al., *Investigation of the bond strength between the photo-sensitive polymer SU-8 and gold*. Microelectronic Engineering, 2005. **78**: p. 152-157.
65. Blanco, F.J., et al., *Novel three-dimensional embedded SU-8 microchannels fabricated using a low temperature full wafer adhesive bonding*. JOURNAL OF MICROMECHANICS AND MICROENGINEERING, 2004. **14**(7): p. 1047-1056.
66. Chuang, Y.J., et al., *A novel fabrication method of embedded micro-channels by using SU-8 thick-film photoresists*. Sensors & Actuators: A. Physical, 2003. **103**(1-2): p. 64-69.
67. Zhang, J., et al., *Reduction of diffraction effect for fabrication of very high aspect ratio microchannels in SU-8 over large area by soft cushion technology*. Microsystem Technologies, 2005. **11**(7): p. 519-525.
68. Bohl, B., et al., *Multi-layer SU-8 lift-off technology for microfluidic devices*. JOURNAL OF MICROMECHANICS AND MICROENGINEERING, 2005. **15**(6): p. 1125-1130.
69. Carlier, J., et al., *Integrated microfluidics based on multi-layered SU-8 for mass spectrometry analysis*. JOURNAL OF MICROMECHANICS AND MICROENGINEERING, 2004. **14**(4): p. 619-624.
70. Kim, K., et al., *A tapered hollow metallic microneedle array using backside exposure of SU-8*. JOURNAL OF MICROMECHANICS AND MICROENGINEERING, 2004. **14**(4): p. 597-603.
71. Chang, H.K. and Y.K. Kim, *UV-LIGA process for high aspect ratio structure using stress barrier and C-shaped etch hole*. Sensors & Actuators: A. Physical, 2000. **84**(3): p. 342-350.
72. Williams, J.D. and W. Wang, *Using megasonic development of SU-8 to yield ultra-high aspect ratio microstructures with UV lithography*. Microsystem Technologies, 2004. **10**(10): p. 694-698.



73. Gao, H., *A computational study of quasi-2D flows at low Reynolds numbers*, in *Aerospace Engineering*. 2008, Iowa State University.
74. Garg, V.K., *Applied Computational Fluid Dynamics*. 1998: CRC Press.
75. Mata, A., A.J. Fleischman, and S. Roy, *FABRICATION OF 3D MICRO-TEXTURED SCAFFOLDS FOR TISSUE ENGINEERING*. Newport. **6**: p. 7.
76. Mata, A., A.J. Fleischman, and S. Roy. *Microfabricated 3D scaffolds for tissue engineering applications*. 2005: Warrendale, Pa.; Materials Research Society; 1999.

## Appendix A

The final shape of the fan and obtained results from CFD simulations (for angles of 5, 25 and 35 degrees) in details are presented in this appendix. A top view and a 3-D view of the fan are shown in Figure A-1.

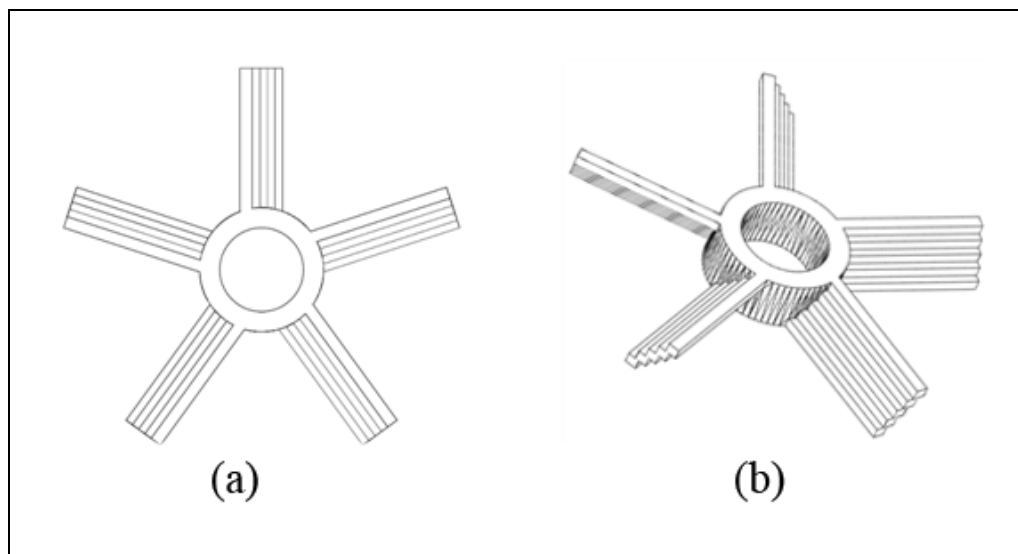


Figure A-1 Top view (a) and 3-D view (b) of the final product

These two pictures are for an angle of attack of 20 degrees. The blade angle is equal to  $37^\circ$ .

## Appendix B

The details for the conducted numerical analysis are presented here. The 2-D numerical analysis for preliminary design, modified design and flat plate are available in the Appendix B. The velocity and pressure contours are presented. The forces and the coefficients are also tabulated.

## Preliminary Design

Angle of attack =  $5^\circ$

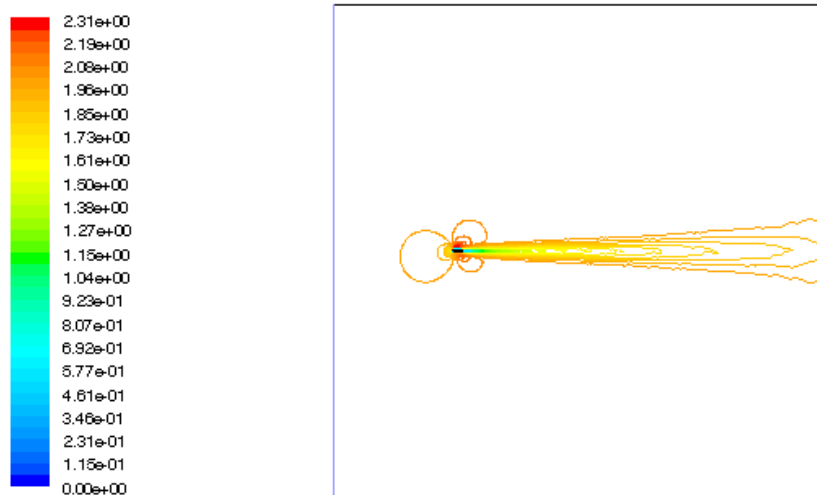


Figure B-2 Whole domain, angle of attack =  $5^\circ$

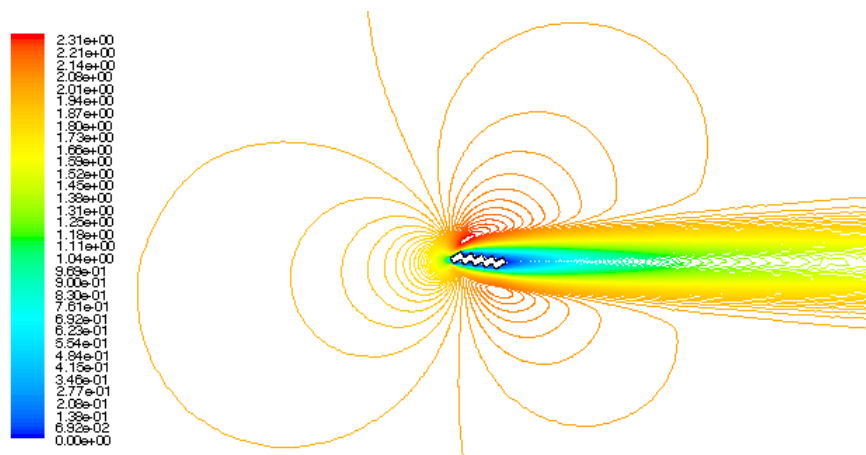


Figure B-3 Velocity contour around the airfoil, angle of attack =  $5^\circ$

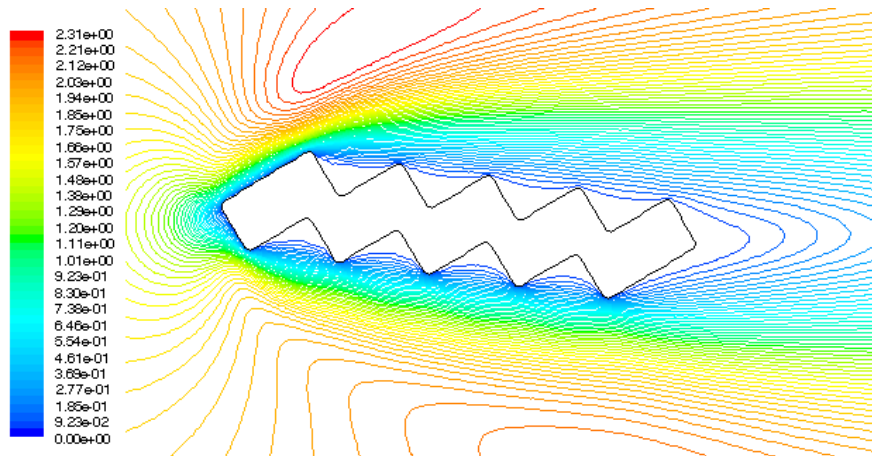


Figure B-4 Velocity contour around the airfoil, a closer view, angle of attack=5°

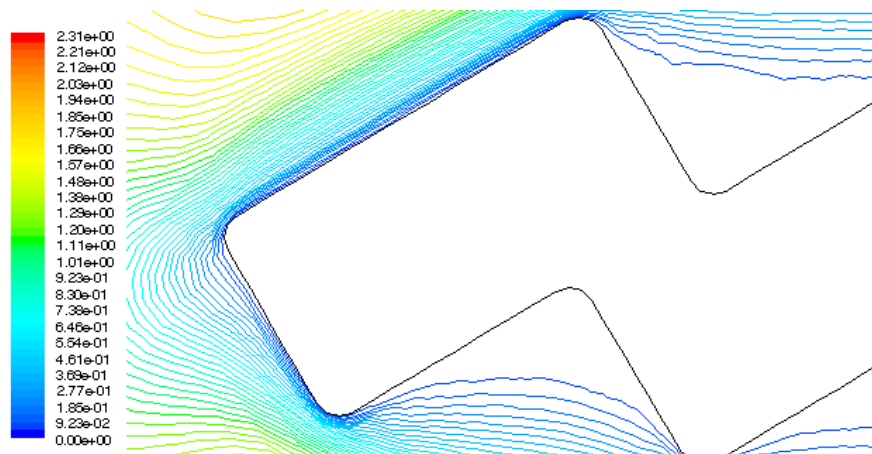


Figure B-5 Velocity contour around incidence area, angle of attack=5°

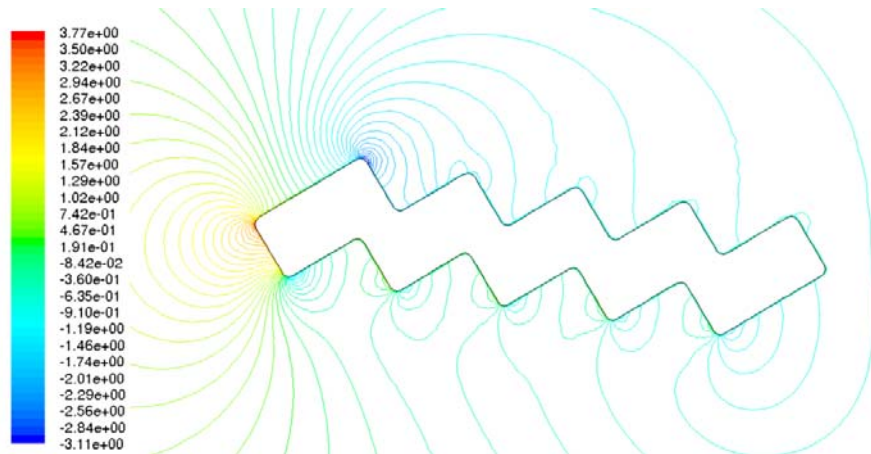


Figure B-6 Pressure contour around the airfoil, angle of attack=5°

Table B-0-1 Forces and coefficients parallel to the free stream velocity direction (Drag)

force (N)			coefficient		
Pressure	Viscous	Total	Pressure	Viscous	Total
0.00055394006	0.0003624211	0.00091636116	0.32366201	0.21175927	0.53542127

Table B-0-2 Forces and coefficients perpendicular to the free stream velocity direction (Lift)

force (N)			coefficient		
Pressure	Viscous	Total	Pressure	Viscous	Total
0.0004164332	2.9538391e-05	0.00044597159	0.24331803	0.017259006	0.26057704

$$\frac{C_L}{C_D} = 0.4867$$

Angle of attack =  $10^\circ$



Figure B-7 Whole domain, angle of attack =  $10^\circ$

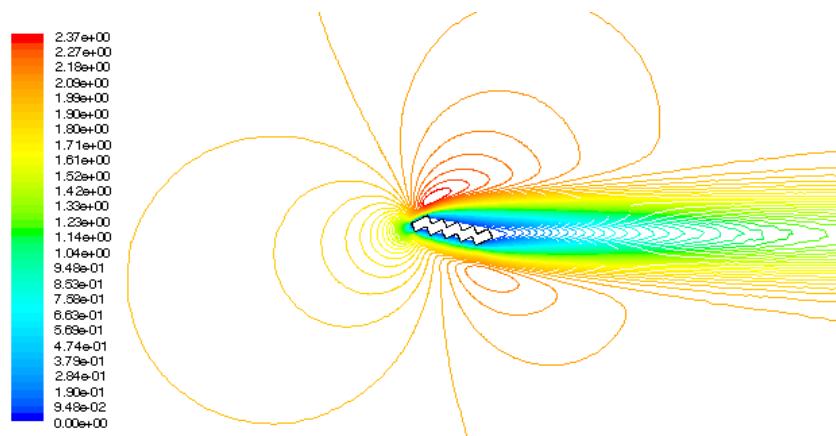


Figure B-8 Velocity contour around the airfoil, angle of attack =  $10^\circ$

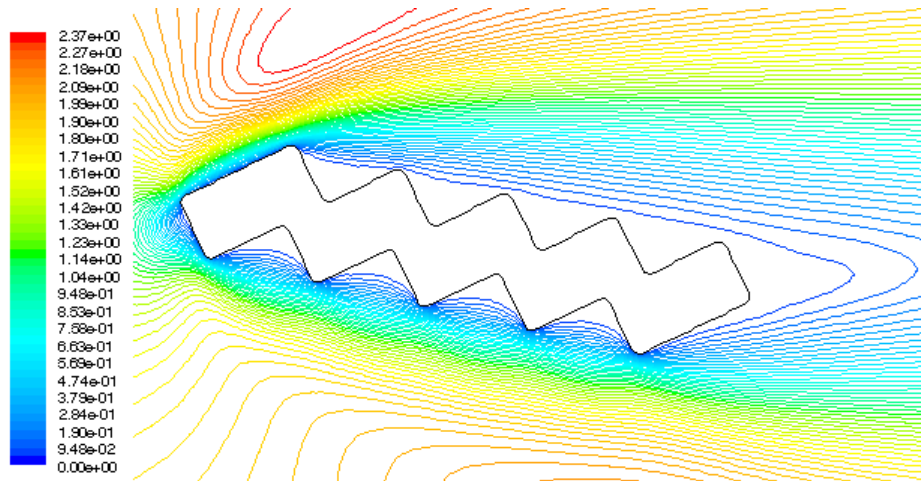
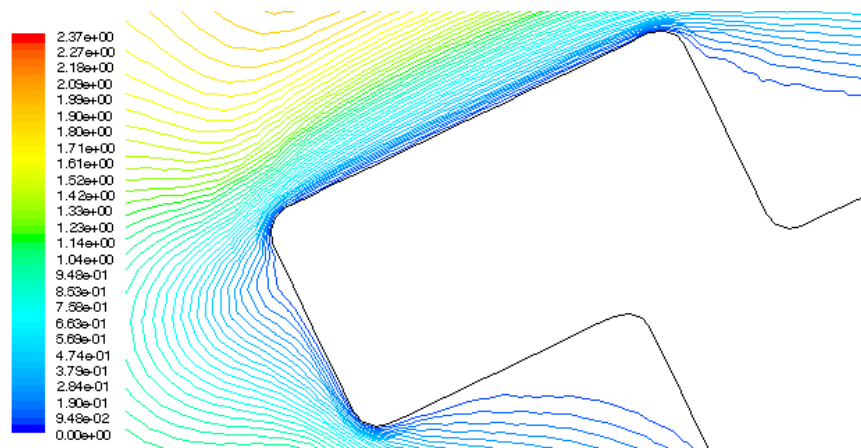
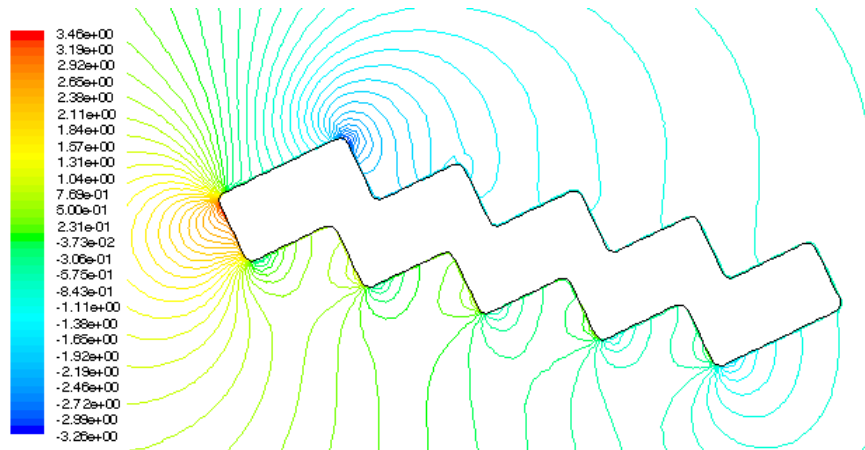


Figure B-9 Velocity contour around the airfoil, a closer view, angle of attack=10°



0Figure B-10 Velocity contour around the airfoil, a closer view, angle of attack=10°





0 Figure B-11 Pressure contour around the airfoil, angle of attack=10°

Table B-3 Forces and coefficients parallel to the free stream velocity direction (Drag)

force (N)			coefficient		
Pressure	Viscous	Total	Pressure	Viscous	Total
0.00061281251	0.00035310959	0.0009659221	0.35806061	0.20631863	0.56437924

Table B-4 Forces and coefficients perpendicular the free stream velocity direction (Lift)

force (N)			coefficient		
Pressure	Viscous	Total	Pressure	Viscous	Total
0.00074101171	3.1877148e-05	0.00077288886	0.43296621	0.018625519	0.45159173

$$\frac{C_L}{C_D} = 0.8001$$

Angle of attack=20°

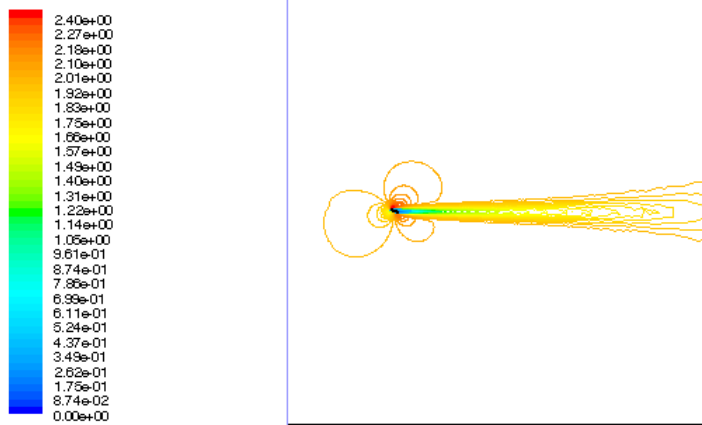


Figure B-12 Whole domain, angle of attack = 20°

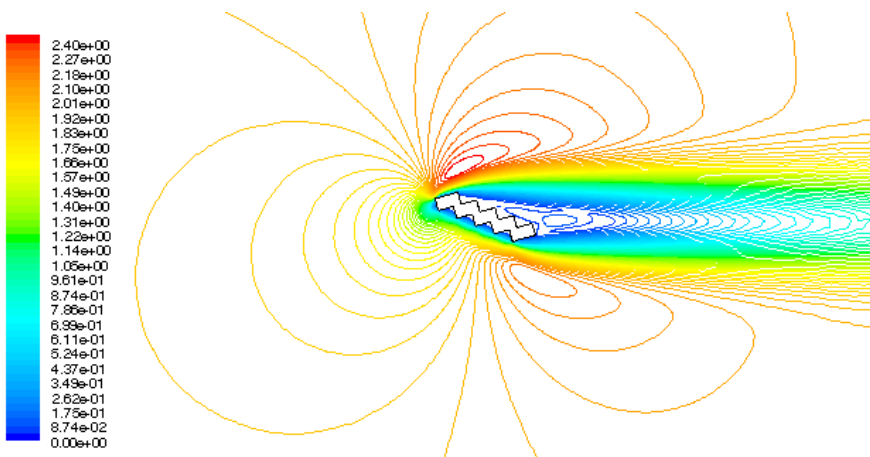


Figure B-13 contour around the airfoil, a closer view, angle of attack=20°

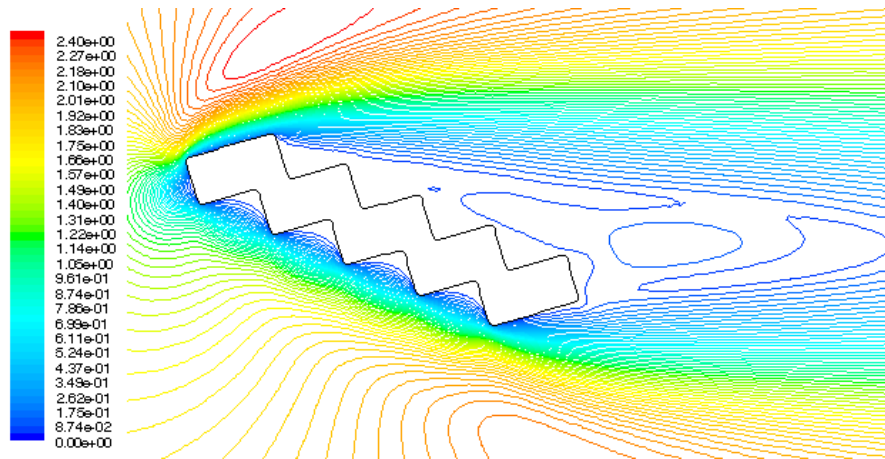


Figure B-14 contour around the airfoil, a closer view, angle of attack= $20^\circ$

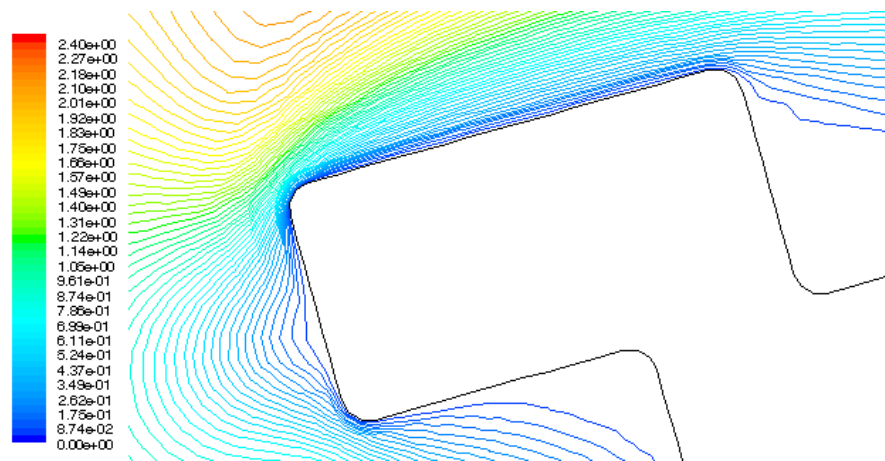


Figure B-15 contour around the airfoil, a closer view, angle of attack= $20^\circ$

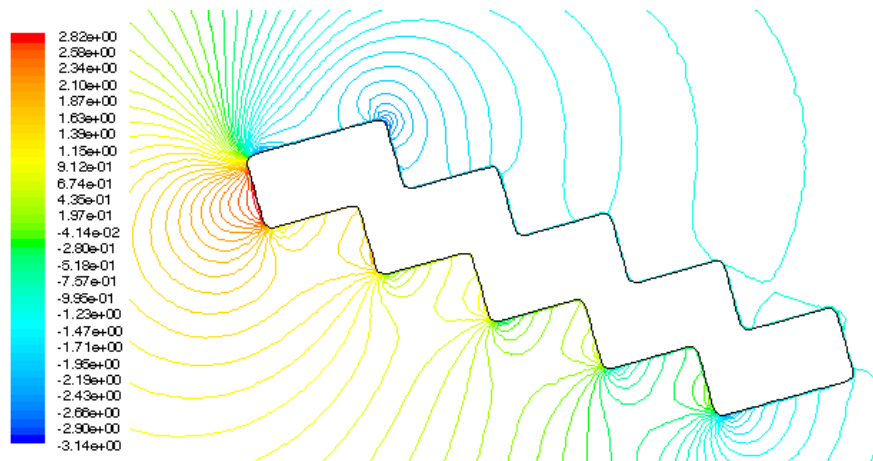


Figure B-16 Pressure contour around the airfoil, angle of attack=20°

Table B-5 Forces and coefficients parallel to the free stream velocity direction (Drag)

force (N)			coefficient		
Pressure	Viscous	Total	Pressure	Viscous	Total
0.00080832702	0.00031803359	0.0011263606	0.47229791	0.18582405	0.65812196

Table B-6 Forces and coefficients perpendicular the free stream velocity direction (Lift)

force (N)			coefficient		
Pressure	Viscous	Total	Pressure	Viscous	Total
0.0010837587	2.687233e-05	0.001110631	0.63323005	0.015701251	0.6489313

$$\frac{C_L}{C_D} = 0.9860$$

Angle of attack=25°

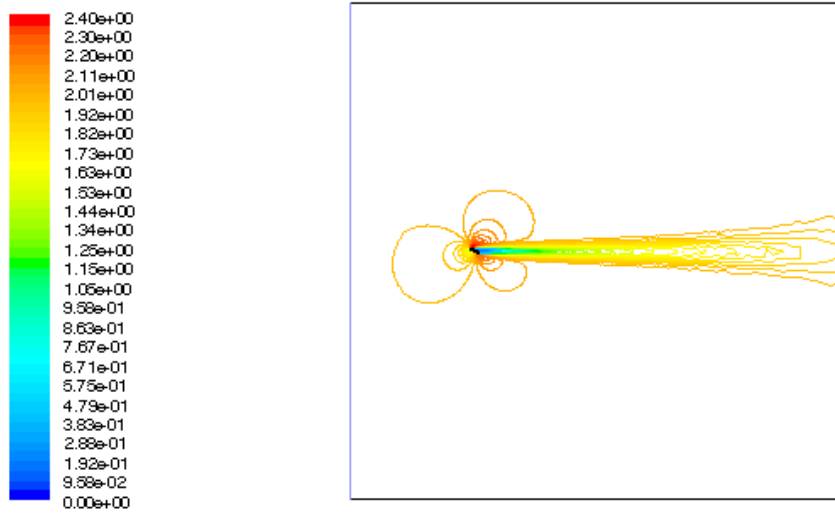


Figure B-17 Velocity contour in whole domain, angle of attack=25°

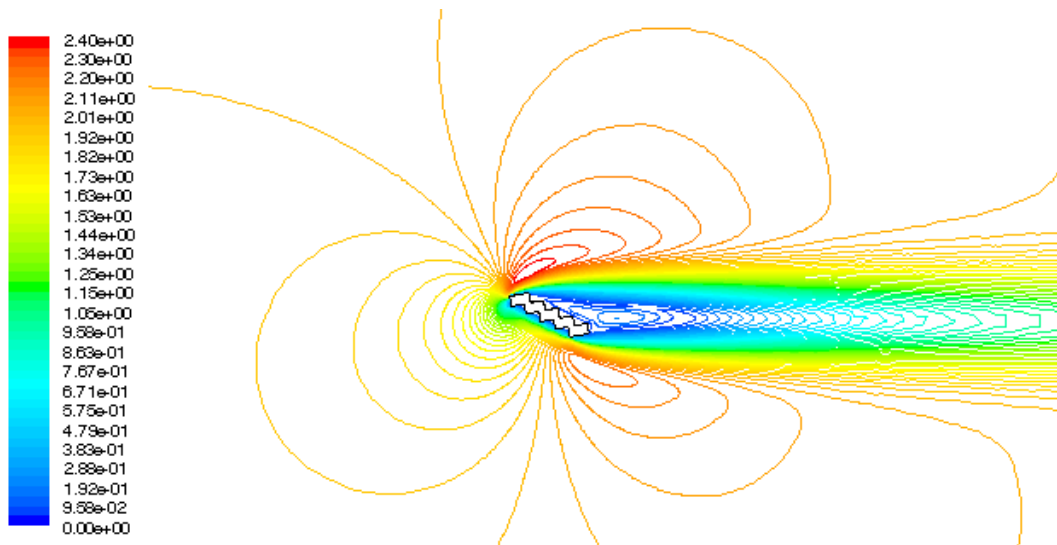


Figure B-18 Velocity contour around the airfoil, angle of attack=25°

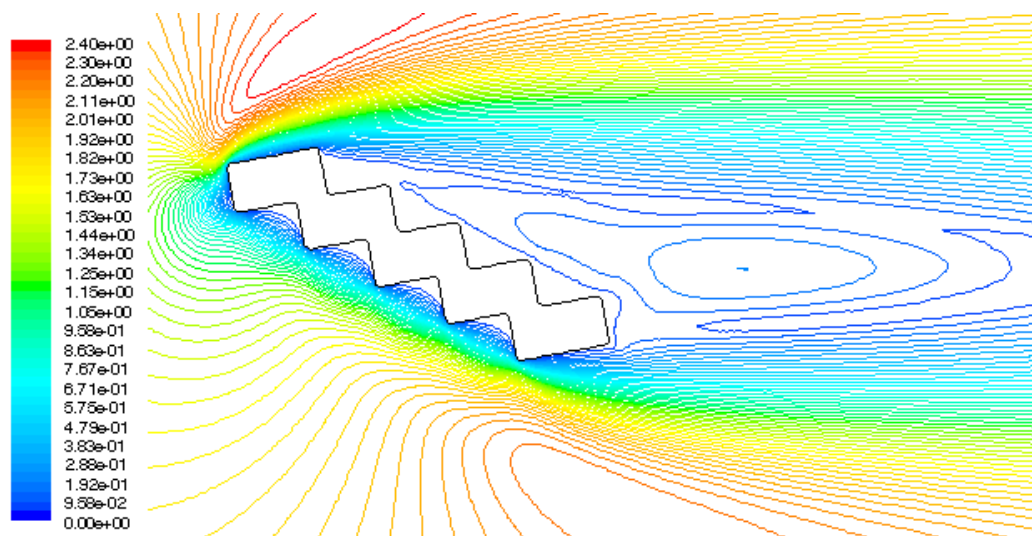


Figure B-19 Velocity contour around the airfoil, angle of attack=25°

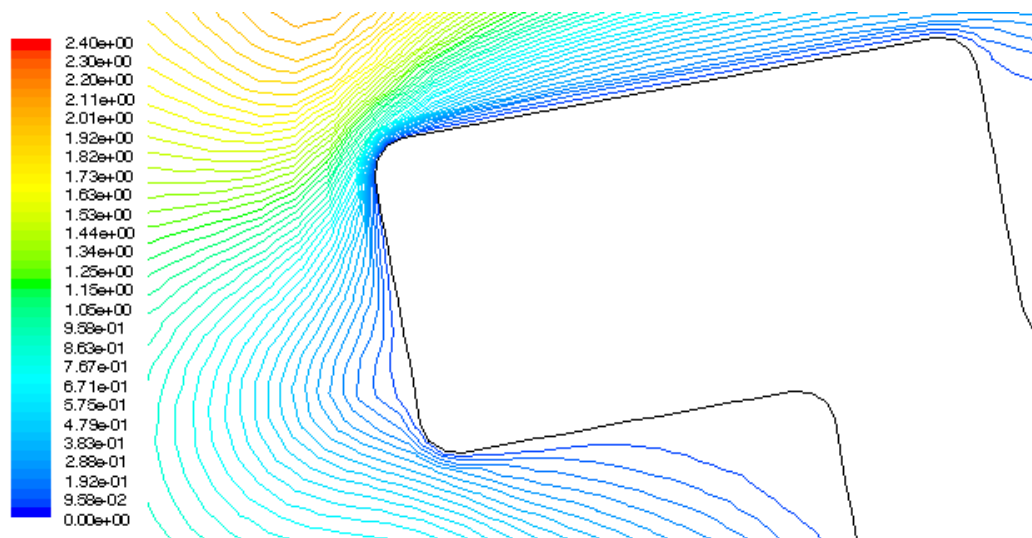


Figure B-20, Velocity contour around the leading edge, angle of attack=25°

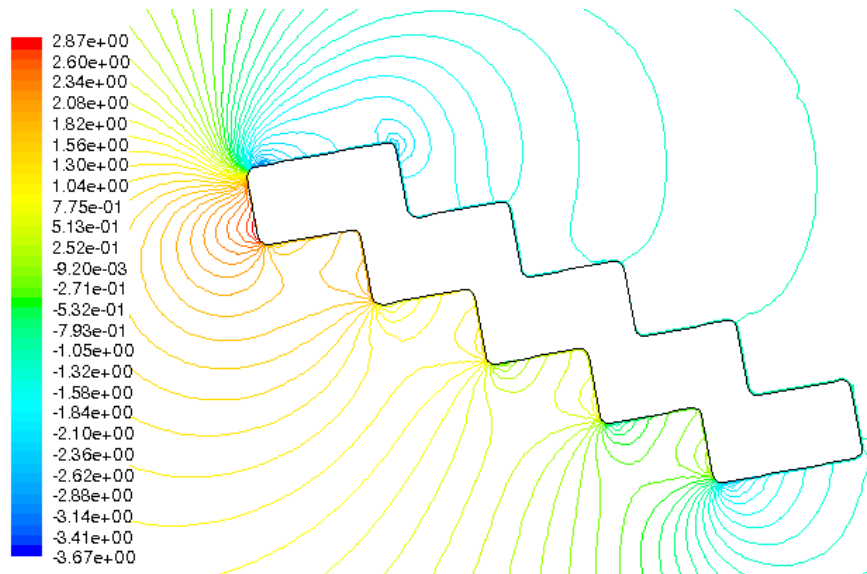


Figure B-21, Pressure contour around the airfoil

Table B-7 Forces and coefficients parallel to the free stream velocity direction (Drag)

force (N)			coefficient		
Pressure	Viscous	Total	Pressure	Viscous	Total
0.00092753733	0.00029637808	0.0012239154	0.54195138	0.17317094	0.71512232

Table B-8 Forces and coefficients perpendicular the free stream velocity direction (Lift)

force (N)			coefficient		
Pressure	Viscous	Total	Pressure	Viscous	Total
0.0011531724	2.0890972e-05	0.0011740634	0.67378783	0.012206399	0.68599423

$$\frac{C_L}{C_D} = 0.9593$$

Angle of attack=30°



Figure B-22 Velocity contour in whole domain, angle of attack=30°

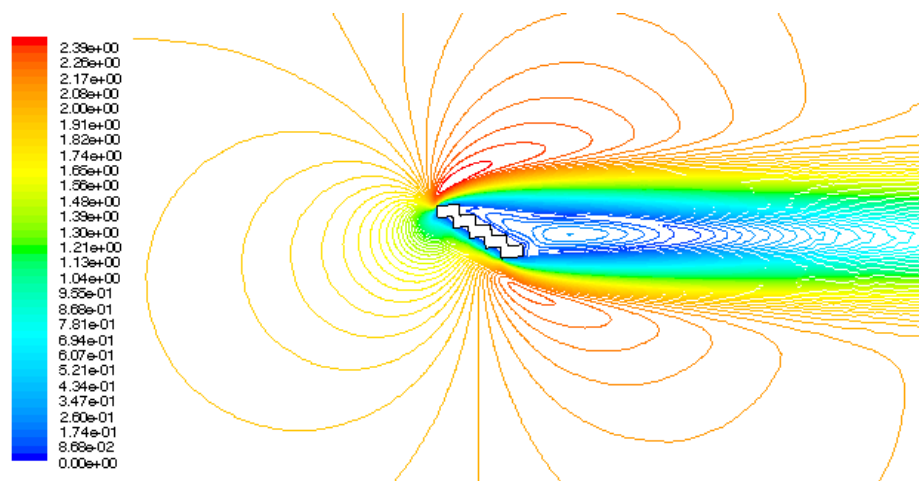


Figure B-23 Velocity contour around the airfoil, angle of attack=30°



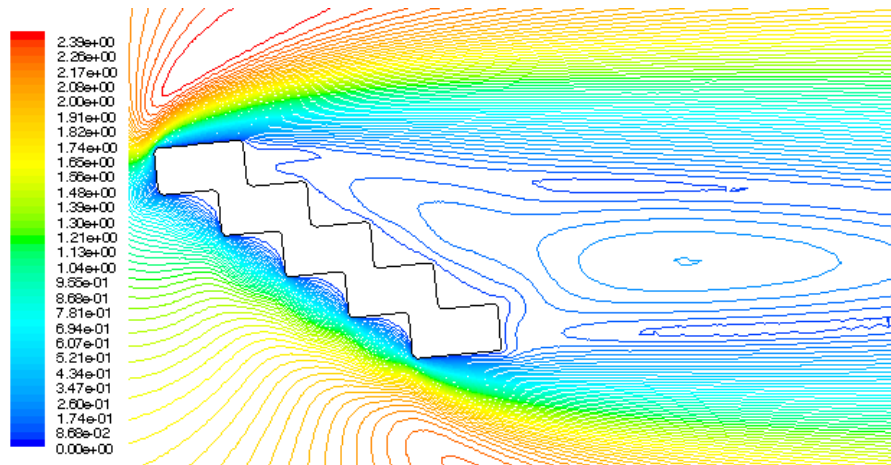


Figure B-24 Velocity contour around the airfoil, angle of attack=30°

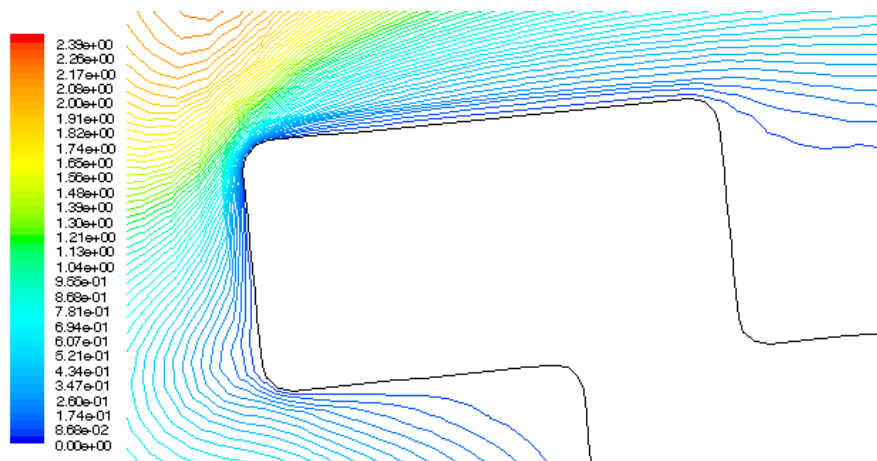


Figure B-25 Velocity contour around the airfoil, angle of attack=30°

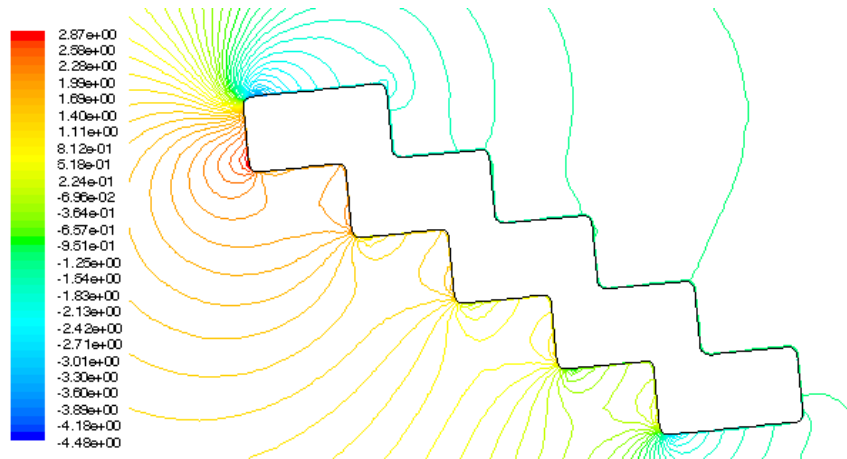


Figure B-26 Pressure contour around the airfoil, angle of attack=30°

Table B-9 Forces and coefficients parallel to the free stream velocity direction (Drag)

force (N)			coefficient		
Pressure	Viscous	Total	Pressure	Viscous	Total
0.0010541451	0.00027431997	0.0013284651	0.61592711	0.16028259	0.7762097

Table B-10 Forces and coefficients perpendicular the free stream velocity direction (Lift)

force (N)			coefficient		
Pressure	Viscous	Total	Pressure	Viscous	Total
0.0011812119	1.4544862e-05	0.0011957567	0.69017103	0.0084984267	0.69866946

$$\frac{C_L}{C_D} = 0.9002$$

Angle of attack=35°



Figure B-27 Velocity contour in whole domain, angle of attack=35°

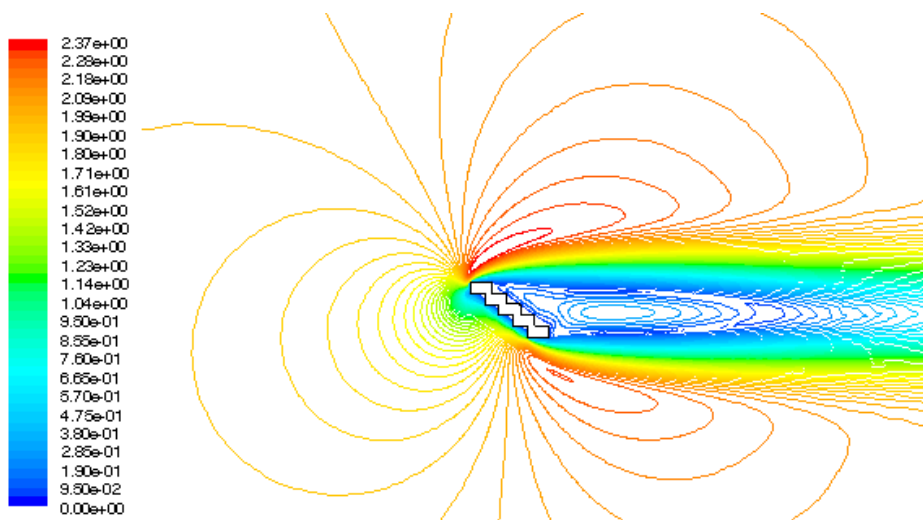


Figure B-28 Velocity contour around the airfoil, angle of attack=35°

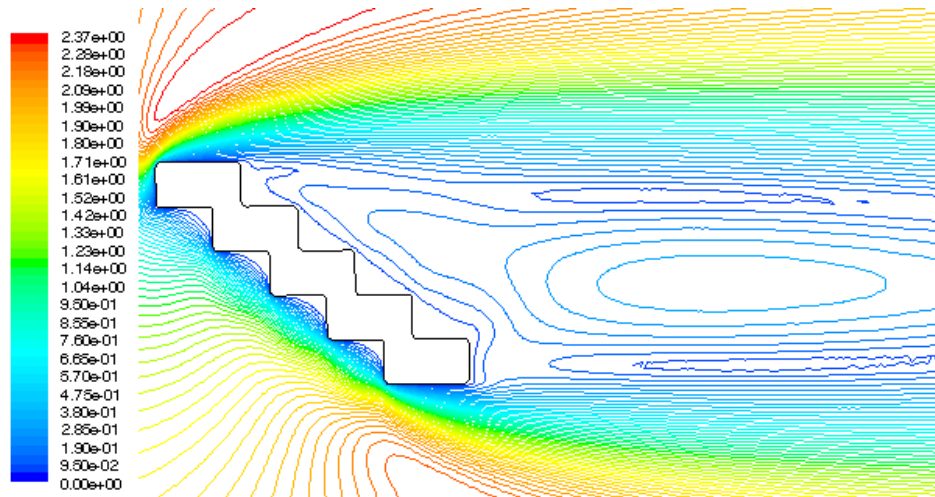


Figure B-29 Velocity contour round the airfoil, angle of attack= $35^\circ$

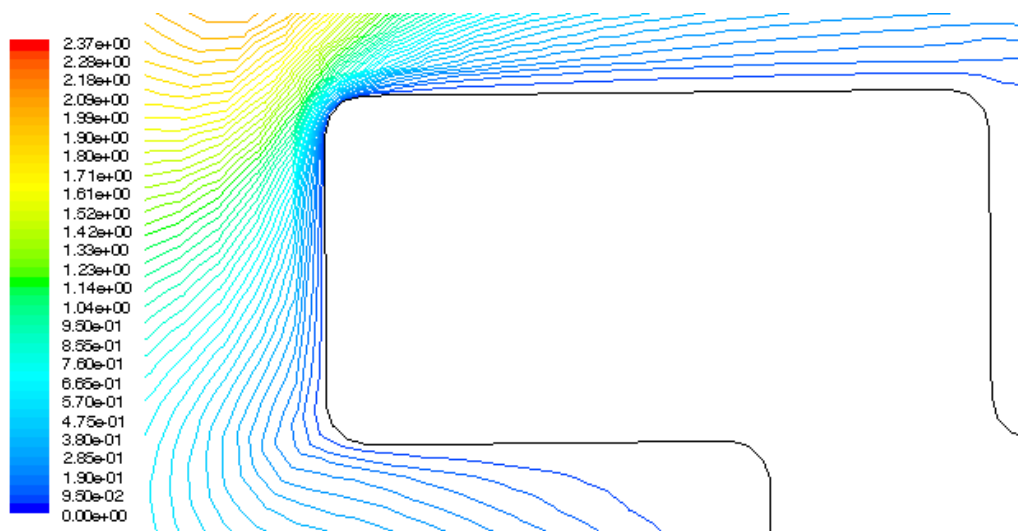


Figure B-30 Velocity contour near to the leading edge, angle of attack= $35^\circ$

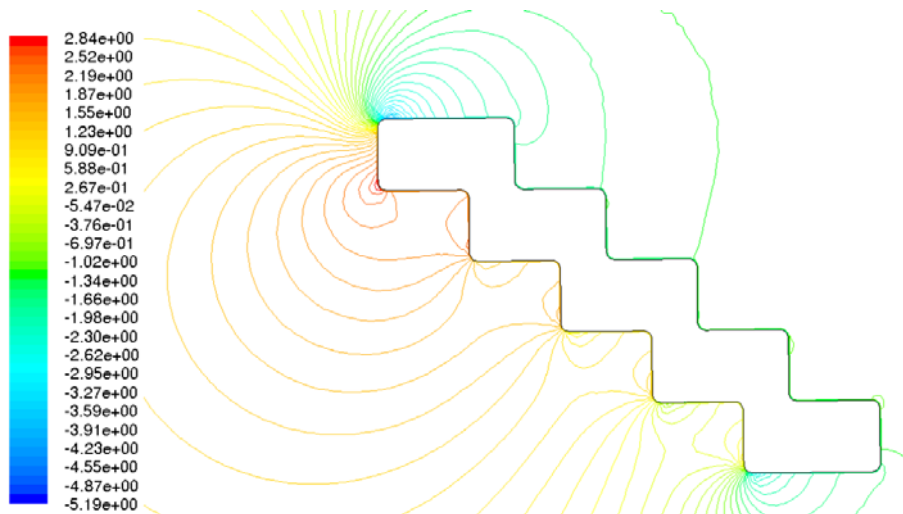


Figure B-31 Pressure contour around the airfoil, angle of attack=35°

Table B-11 Forces and coefficients parallel to the free stream velocity direction (Drag)

force (N)			coefficient		
Pressure	Viscous	Total	Pressure	Viscous	Total
0.0011840093	0.00025189746	0.0014359068	0.69180557	0.14718133	0.8389869

Table B-12 Forces and coefficients perpendicular to the free stream velocity direction (Lift)

force (N)			coefficient		
Pressure	Viscous	Total	Pressure	Viscous	Total
0.0011786198	8.5794908e-06	0.0011871993	0.68865654	0.0050129162	0.69366946

$$\frac{C_L}{C_D} = 0.8268$$

## Modified Geometry

*Angle of attack= 20°*

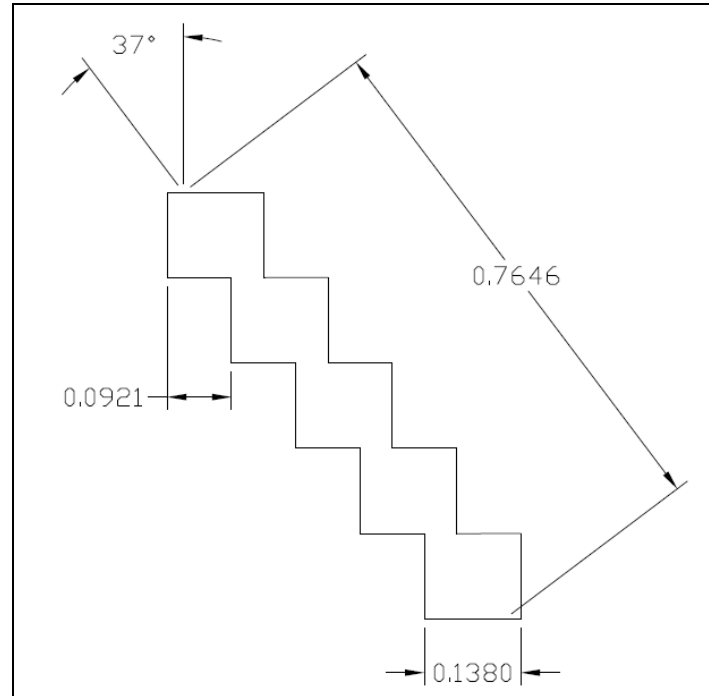


Figure B-31 Modified geometry, angle of attack=20°

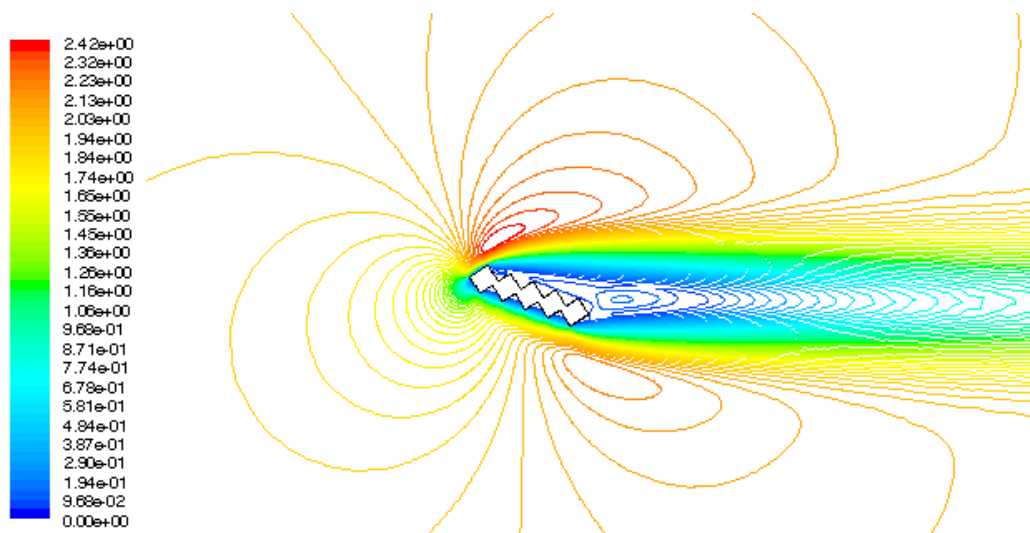


Figure B-32 Velocity contour, angle of attack=20°

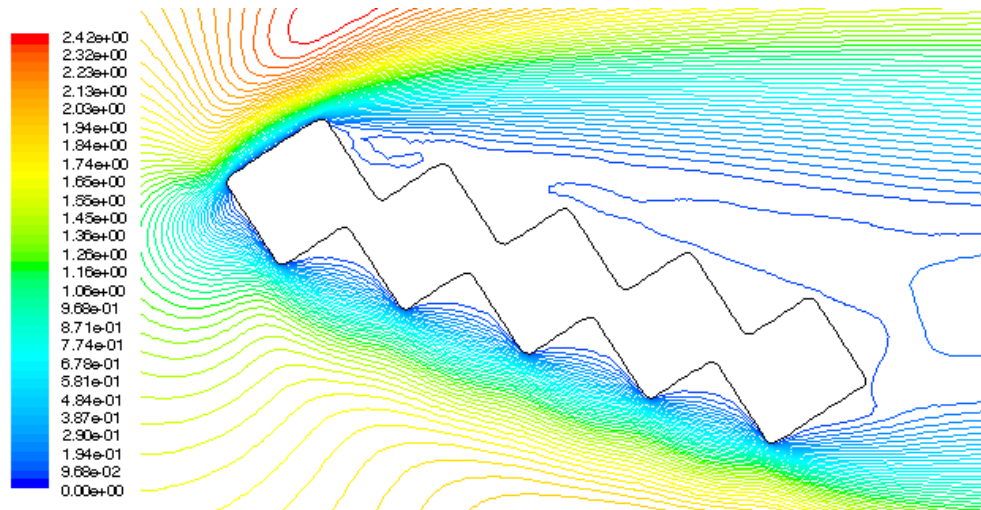


Figure B-33 Velocity contour, angle of attack=20°

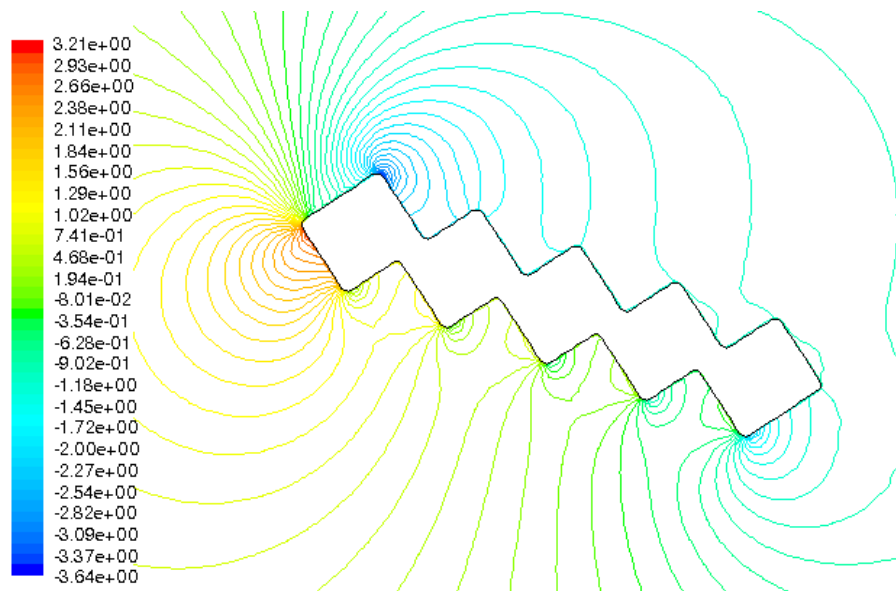


Figure B-34 Pressure contour, angle of attack=20°

**Table B-13 Forces and coefficients parallel to the free stream velocity direction (Drag)**

force (N)			coefficient		
Pressure	Viscous	Total	Pressure	Viscous	Total
0.00088649112	0.00030044385	0.001186935	0.48781858	0.16532832	0.6531469

**Table B-14 Forces and coefficients perpendicular to the free stream velocity direction (Lift)**

force (N)			coefficient		
Pressure	Viscous	Total	Pressure	Viscous	Total
0.0011374432	1.6283489e-05	0.0011537267	0.62591255	0.0089604829	0.63487304

$$\frac{C_L}{C_D} = 0.972$$

**Angle of attack = 25°**

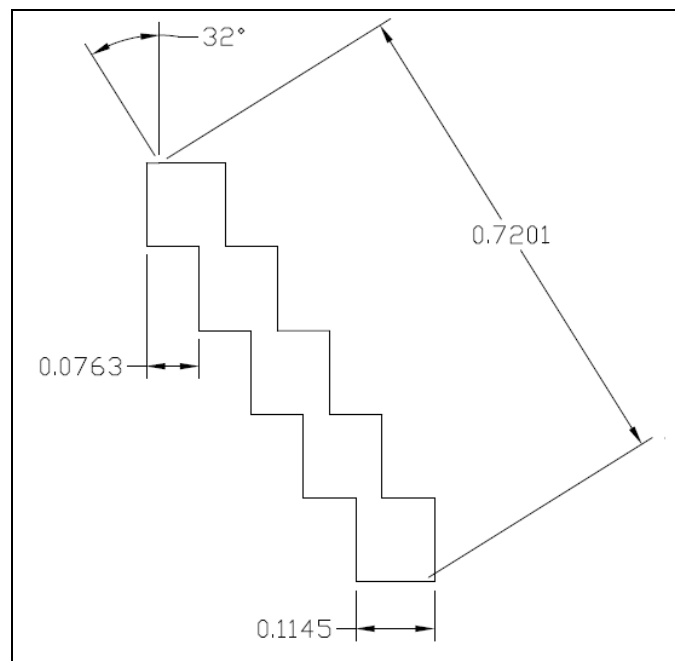


**Figure B-35 Modified geometry for angle of attack = 25°**



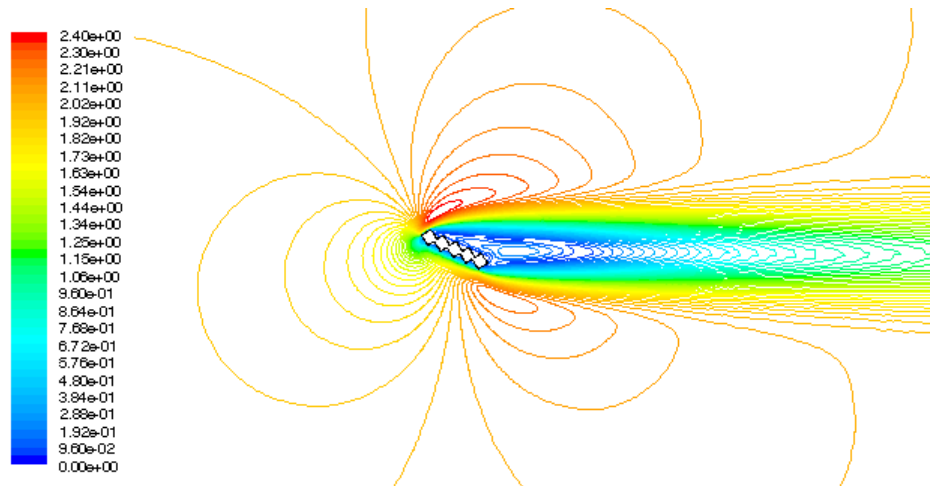


Figure B-36 Velocity contours around the airfoil, angle of attack =  $25^\circ$

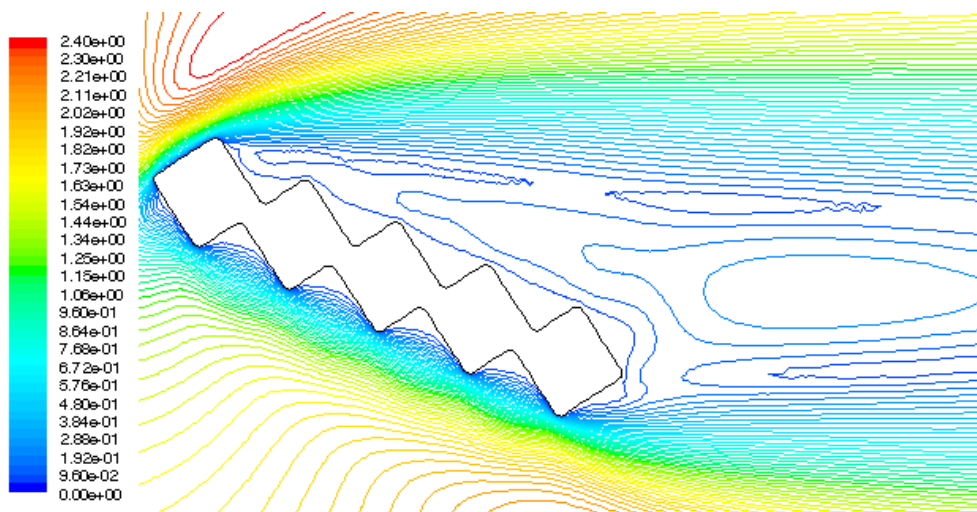


Figure B-37 Velocity contours around the airfoil, a close view, angle of attack =  $25^\circ$

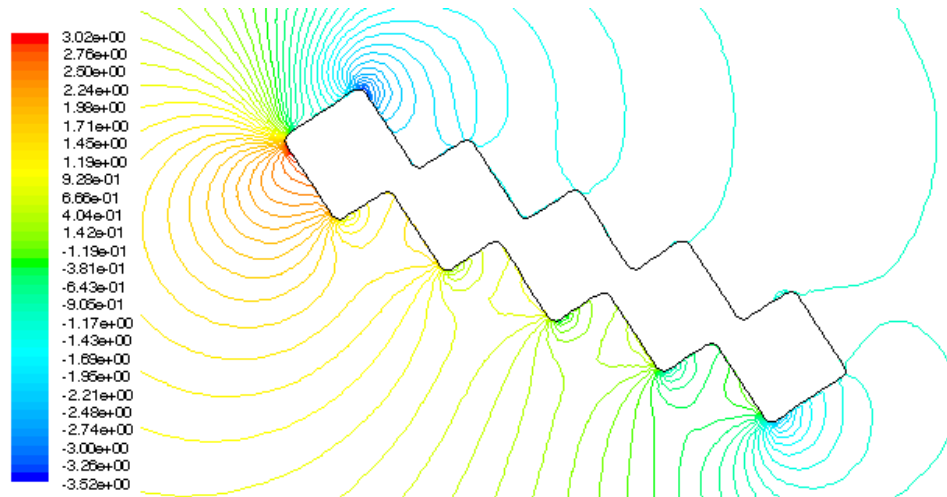


Figure B-38 Pressure contours around the airfoil, angle of attack = 25°

Table B-15 Forces and coefficients parallel to the free stream velocity direction (Drag)

force (N)			coefficient		
Pressure	Viscous	Total	Pressure	Viscous	Total
0.00097939708	0.00027475135	0.0012541484	0.57225255	0.16053464	0.73278719

Table B-16 Forces and coefficients perpendicular to the free stream velocity direction (Lift)

force (N)			coefficient		
Pressure	Viscous	Total	Pressure	Viscous	Total
0.0011896458	1.6980163e-06	0.0011913438	0.69509892	0.00099213503	0.69609105

$$\frac{C_L}{C_D} = 0.950$$

Angle of attack=  $30^\circ$

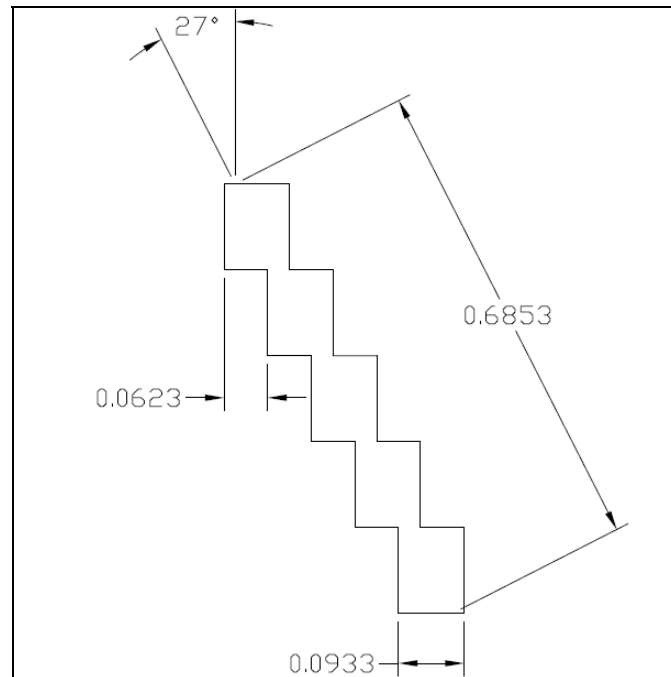


Figure B-39 Modified geometry, angle of attack= $30^\circ$

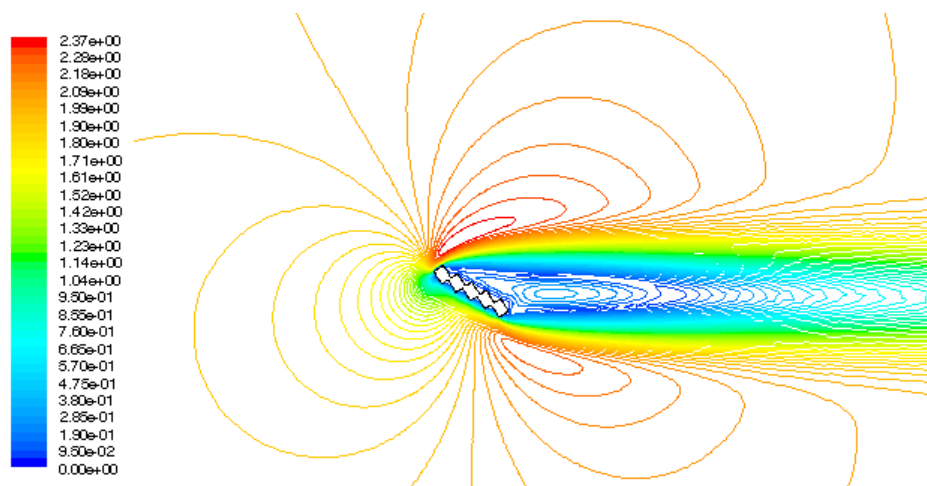


Figure B-40 Velocity contour, angle of attack= $30^\circ$

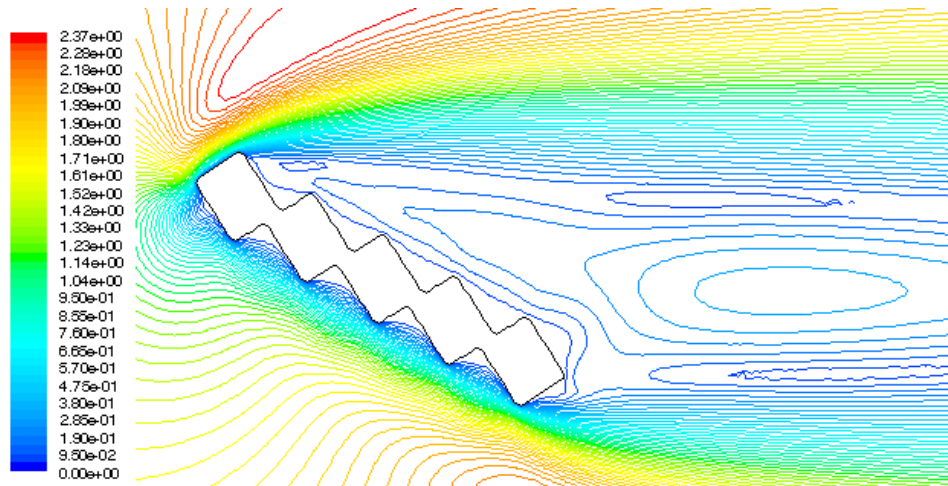


Figure B-41 Velocity contour, angle of attack=30°

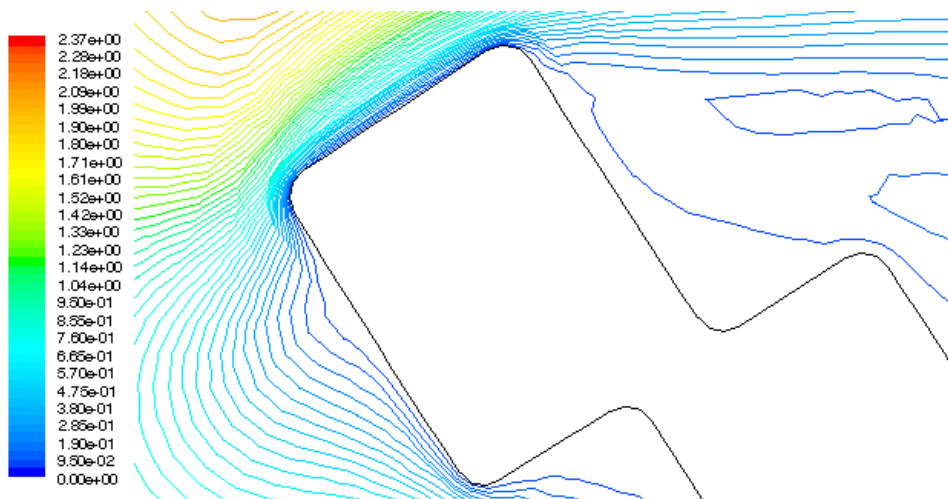


Figure B-42 Velocity contour around the leading edge, angle of attack=30°

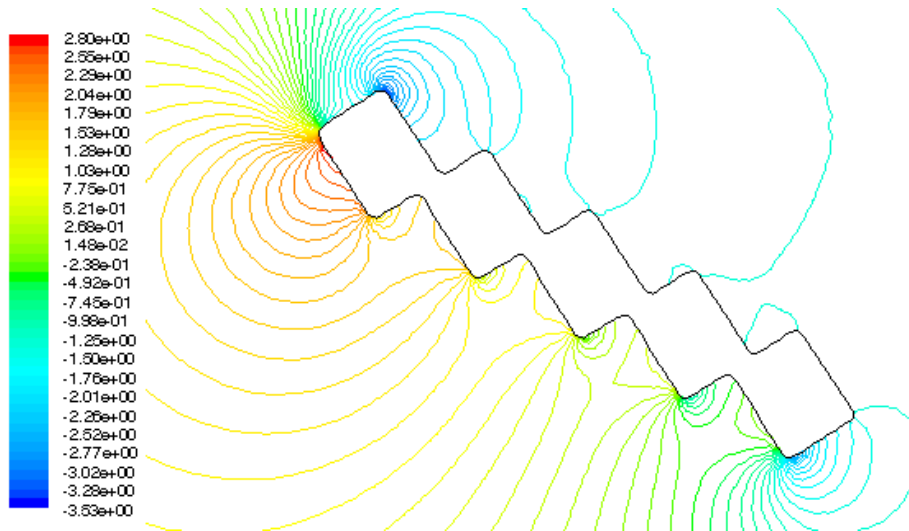


Figure B-43 Pressure contour around the airfoil, angle of attack=30°

Table B-17 Forces and coefficients parallel to the free stream velocity direction (Drag)

force (N)			coefficient		
Pressure	Viscous	Total	Pressure	Viscous	Total
0.0010721047	0.00025024723	0.0013223519	0.65804341	0.15359837	0.81164178

Table B-18 Forces and coefficients perpendicular to the free stream velocity direction (Lift)

force (N)			coefficient		
Pressure	Viscous	Total	Pressure	Viscous	Total
0.0012074229	-1.1681052e-05	0.0011957419	0.74109991	-0.007169672	0.73393024

$$\frac{C_L}{C_D} = 0.904$$



## Flat Plate

Angle of attack =  $20^\circ$

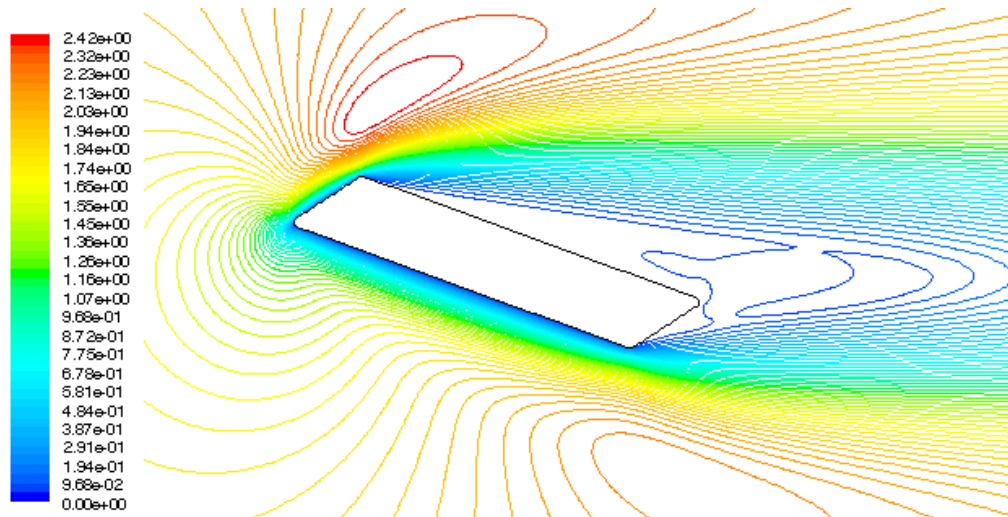


Figure B-44 Velocity contour, angle of attack= $20^\circ$

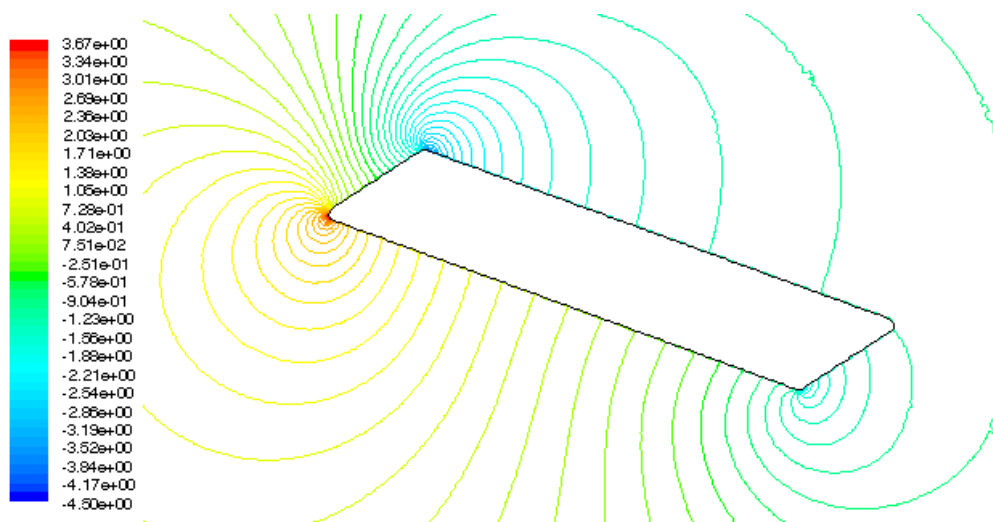


Figure B-45 Pressure contour around the flat plate, angle of attack= $20^\circ$

Table B-19 Forces and coefficients parallel to the free stream velocity direction (Drag)

force (N)			coefficient		
Pressure	Viscous	Total	Pressure	Viscous	Total
0.00060758149	0.00055827676	0.0011658583	0.33434011	0.30720869	0.6415488

Table B-20 Forces and coefficients perpendicular to the free stream velocity direction (Lift)

force (N)			coefficient		
Pressure	Viscous	Total	Pressure	Viscous	Total
0.0011881756	-2.972993e-06	0.0011852026	0.6538296	-0.00163598	0.65219362

$$\frac{C_L}{C_D} = 1.017$$

Angle of attack = 25°

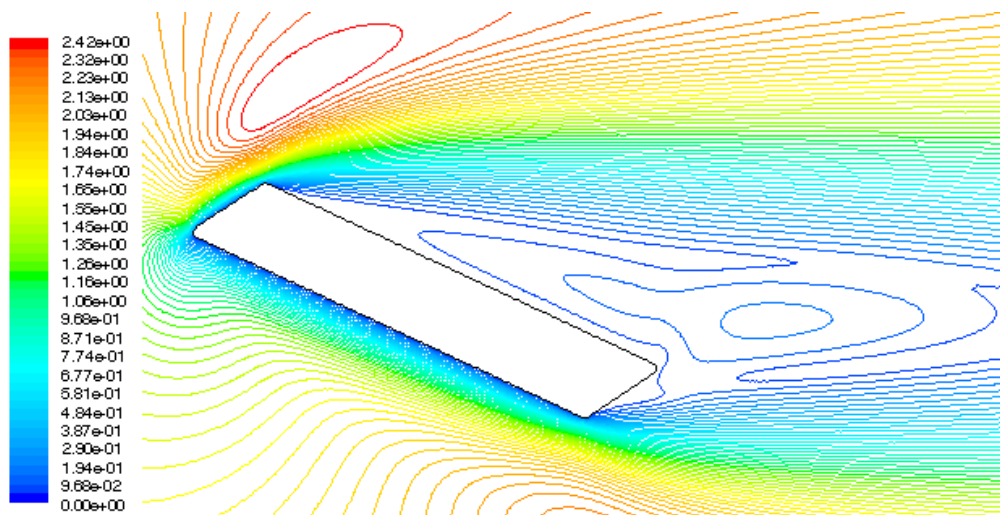


Figure B-46 Velocity contour, angle of attack=25°

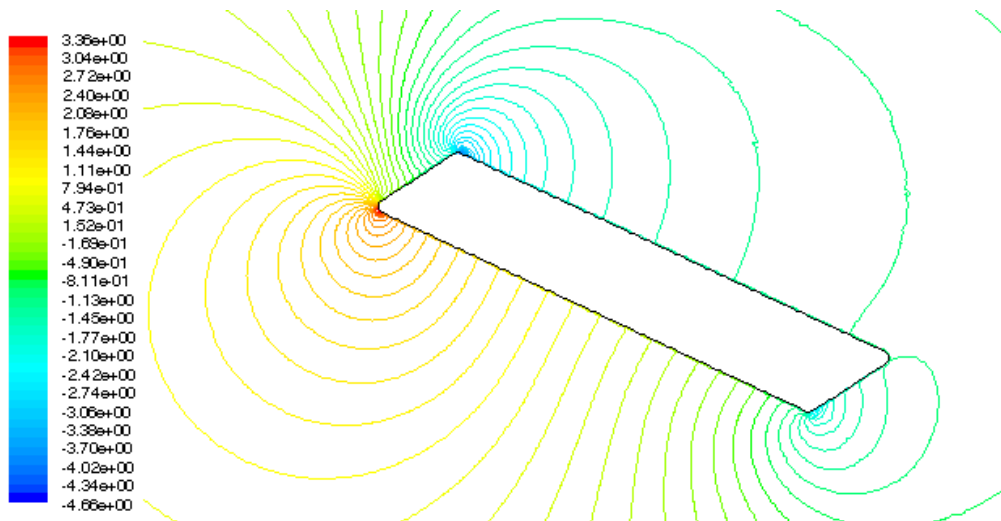


Figure B-47 Pressure contour around the flat plate, angle of attack=25°

Table B-21 Forces and coefficients parallel to the free stream velocity direction (Drag)

force (N)			coefficient		
Pressure	Viscous	Total	Pressure	Viscous	Total
0.00074294475	0.00049459323	0.001237538	0.43409567	0.2889862	0.72308186

Table B-22 Forces and coefficients perpendicular to the free stream velocity direction (Lift)

force (N)			coefficient		
Pressure	Viscous	Total	Pressure	Viscous	Total
0.0012962526	-2.335825e-05	0.0012728943	0.75738825	-0.01364801	0.74374025

$$\frac{C_L}{C_D} = 1.029$$



Angle of attack =  $30^\circ$

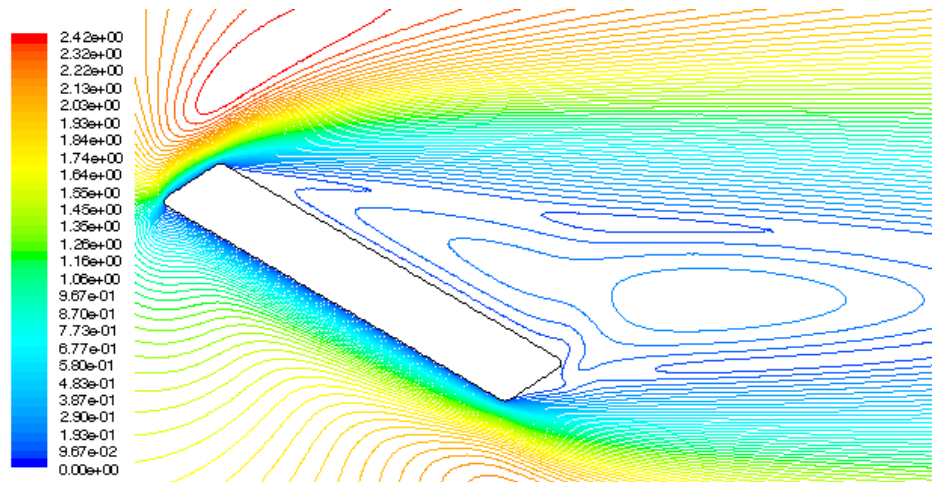


Figure B-48 Velocity contour, angle of attack= $30^\circ$

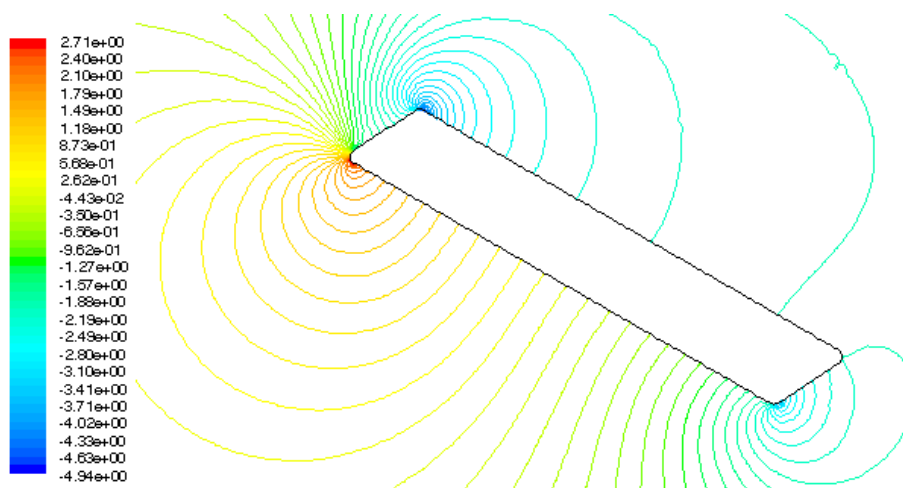


Figure B-49 Pressure contour around the flat plate, angle of attack= $30^\circ$

Table B-23 Forces and coefficients parallel to the free stream velocity direction (Drag)

force (N)			coefficient		
Pressure	Viscous	Total	Pressure	Viscous	Total
0.00088513851	0.00042525948	0.001310398	0.54328609	0.26101853	0.80430462



Table B-24 Forces and coefficients perpendicular to the free stream velocity direction (Lift)

force (N)			coefficient		
Pressure	Viscous	Total	Pressure	Viscous	Total
0.0013518079	-4.353293e-05	0.001308275	0.82972146	-0.02671993	0.80300154

$$\frac{C_L}{C_D} = 0.998$$